Future Probes of Cosmology and the High-Redshift Universe

Future Probes of Cosmology and the High-Redshift Universe

A dissertation presented

by

Elijah Francis Visbal

to

The Department of Physics

in partial fulfillment of the requirements

for the degree of

Doctor of Philosophy

in the subject of

Physics

Harvard University

Cambridge, Massachusetts

April 2013

Dissertation Advisor: Professor Abraham Loeb Elijah Francis Visbal

Future Probes of Cosmology and the High-Redshift Universe

Abstract

This thesis is a study in theoretical cosmology with an emphasis on the high-redshift universe and promising directions for future observations. In Chapters 2 and 3, we propose intensity mapping of spectral line emission from galaxies. This is a technique to observe the cumulative emission from many galaxies without resolving individual sources. We use analytic calculations and N-body simulations to predict the observational signal for different emission lines, including those from oxygen, carbon monoxide, and carbon.

In Chapter 4, we utilize the Fisher matrix formalism to determine how accurately futuristic 21cm observatories, dedicated to post-reionization redshifts, can constrain cosmological parameters. We find that these experiments may yield significantly better constraints than next generation Cosmic Microwave Background (CMB) experiments such as the Planck telescope.

In Chapter 5, we perform semi-numerical simulations of reionization including a significant contribution from X-rays. We find that the large mean-free-path of X-rays adds a uniform component to reionization. Using these simulations, we compute the impact on the kinetic Sunyaev-Zel'dovich effect and find that a contribution from X-rays could result in a lower value of the so-called "patchy reionization" component of the CMB power spectrum.

In Chapter 6, we present the first realistic simulations of the 3-dimensional distribution of the first galaxies including the newly discovered relative velocity between

baryons and dark matter. We use these simulations to compute the 21cm signal at redshift 20 and find that the relative velocity effect enhances fluctuations on a scale of ≈ 100 Mpc, making observations more feasible than previously expected.

In the final chapter, we propose that the physics which sets the density profiles of dark matter halos can be understood in terms of dissipationless gravitational collapse in non-cosmological simulations. To explore this, we run N-body collapse simulations from cold and spherically symmetric initial conditions. We find that the final equilibrium states of these simulations have some common features with dark matter halos, including the form of the pseudo-phase-space density.

Contents

Abstract **iii**

Acknowledgments **ix**

Dedication **xi**

1 Introduction **1**

1.1 Galaxy Intensity Mapping 3

1.2 Cosmological Constraints from 21cm Intensity Mapping 4

1.3 Gauging the X-ray Contribution to Reionization with the kSZ Effect 4

1.4 Impact of the Baryon-Dark Matter Relative Velocity on the First Stars . . 5

1.5 Density Profiles of Dark Matter Halos 6

2 Measuring the 3D Clustering of Undetected Galaxies Through Cross Correlation of their Cumulative Flux Fluctuations from Multiple Spectral Lines **7**

2.1 Introduction 9

2.2 Method 13

2.2.1 Line Cross Power Spectrum 13

2.2.2 Average Signal, Average Bias, and Shot-noise 17

2.2.3 Cross Power Spectrum Estimation 18

2.2.4 Multiple Lines 21

2.2.5 Remaining Confusion 22
2.3 SPICA 23
2.3.1 Instrument 23
2.3.2 Relevant Lines 25
2.3.3 Results 28
2.4 Cross-correlating CO Lines with 21-cm Emission 41
2.4.1 Instruments 41
2.4.2 Results 42
2.5 Discussion and Conclusions 43
2.6 Appendix: Error on Cross Power Spectrum 47

3 Demonstrating the Feasibility of Line Intensity Mapping Using Mock Data of Galaxy Clustering from Simulations 50

3.1 Introduction 51
3.2 Method 55
3.2.1 Galaxy Line Cross Power Spectrum 55
3.2.2 Synthetic Data Set 57
3.2.3 Simulations 65
3.2.4 Cross Power Spectrum Measurement 67
3.3 SPICA 71
3.3.1 Instrument 71
3.3.2 Results 71
3.4 Intensity Mapping CO(1-0) and CO(2-1) 75
3.5 Discussion and Conclusions 76

4 Cosmological Constraints from 21cm Surveys After Reionization 81

4.1 Introduction 82
4.2 Detectability of the 21cm Signal After Reionization 85

4.3 21cm Power Spectrum 86
4.3.1 Non-Linear Effects on Baryon Acoustic Oscillations 90
4.4 Fisher Matrix Formulation 91
4.4.1 Survey Characteristics 95
4.4.2 Cosmological Parameters 98
4.5 Results 99
4.5.1 Constant Bias 107
4.5.2 Scale Dependent Bias 108
4.5.3 Other Factors 110
4.6 Discussion 113
4.7 Conclusions 117
4.8 Appendix: Modulation of 21cm PS from Ionizing Background 118

5 Gauging the Contribution of X-ray Sources to Reionization Through the Kinetic Sunyaev-Zel'dovich Effect 120

5.1 Introduction 121
5.2 Method 123
5.2.1 The Kinetic SZ Effect 123
5.2.2 Reionization Model 124
5.3 Results 129
5.4 Discussion and Conclusions 137

6 The Signature of the First Stars in Atomic Hydrogen at Redshift 20 142

6.1 Large Supplementary Information 158
6.1.1 Description of the Simulation Code 158
6.1.2 Comparison with Previous Work 160
6.1.3 Timing of Feedback Transitions 163
6.1.4 Observational Considerations 168

7 A Simple Model for the Density Profiles of Isolated Dark Matter Halos 173

7.1 Introduction 174

7.2 A Simple Example 178

7.3 The Outer Density Profile 182

7.4 The Inner Density Profile and the Radial Orbit Instability 183

7.5 A Distribution Function for the Relaxed System 188

7.6 Comparison with previous work 195

7.7 Conclusions 199

7.8 Appendix: Distribution Function of the Radial Jaffe Profile 202

8 Conclusions and Future Directions 204

References 207

Acknowledgments

I am extremely grateful to my parents, Jane and Miguel Visbal. Their constant love and encouragement throughout my life have shaped me into the person I am today. Without them, this work would not have been possible. I thank my brothers, Miguel and Alex, for their support over the course of my studies. I would also like to express my gratitude to Claire Natale for always being there when I needed her.

I feel very fortunate to have had Avi Loeb as my thesis advisor. I learned a tremendous amount from Avi both about astrophysics and how to be an effective scientist. Avi is a constant source of new and creative ideas, which ensured our meetings were always stimulating and productive. Avi's passion for science is truly an inspiration. His enthusiasm rubs off on everyone around him and helped to make my Ph.D. both exciting and enjoyable.

I would like to acknowledge Lars Hernquist, who served as an additional research advisor towards the end of my thesis. I really enjoyed working with Lars and learned a lot from him. I am also very grateful to have had the opportunity to spend August 2011 in Tel Aviv, Israel working with Rennan Barkana. Rennan was not only an excellent scientific advisor, but also a very gracious host, making sure that I felt at ease living in a new country far away from home.

I thank my undergraduate research advisors Rupert Croft and Stefan Westerhoff. Rupert introduced me to research in theoretical cosmology. Working with Rupert was a great experience and encouraged me to continue in the field. I worked with Stefan on high-energy cosmic ray experiments. I am grateful for this opportunity, which gave me a

much better appreciation of what it is like to work on an experiment.

I would also like to acknowledge my other scientific collaborators, who were all a pleasure to work with: Anastasia Fialkov, Chris Hirata, Hy Trac, Dmitriy Tseliakhovich, Mark Vogelsberger, and Stuart Wyithe. Finally, I would like to thank my officemate, Eddie Schlafly, who provided great company and conversation as I performed this research.

To my parents.

Chapter 1

Introduction

The past two decades have seen tremendous progress in cosmology, leading to a standard model (ΛCDM) consistent with a number of independent observations. This model is characterized by parameters that describe the composition and density fluctuations of the universe. Observations of the cosmic microwave background (CMB), galaxy clustering, and supernovae have accurately measured the values of these parameters and indicate that the energy density of the universe is currently dominated by dark energy and dark matter and that the geometry of space is flat (e.g. Komatsu et al. 2011).

While progress has been rapid, there remains a major observational gap in the history of the universe. The CMB provides us with a detailed picture of the cosmos at an age of 400,000 years (corresponding to a redshift of $z \approx 1,100$) and existing telescopes can observe galaxies after a cosmic age of roughly 650 million years ($z < 8$) (e.g. Bouwens et al. 2012). Thus, most of the first billion years of the universe have not been directly observed. It is during this time that the first stars appeared and the intergalactic medium (IGM) was reionized.

Using the standard model of cosmology, it is possible to make theoretical predictions for the high-redshift universe. Cosmological simulations and analytic techniques have been used to study the formation of the first stars, galaxy evolution, and reionization (Loeb 2010). However, many of these predictions are still highly uncertain. Improving them is particularly important because upcoming observations will soon provide new data on the early universe. For example, the James Webb Space Telescope (JWST) will detect galaxies at much higher redshifts than currently possible (Gardner et al. 2006). Redshifted 21cm emission from the IGM measured with radio observatories such as the Murchison Widefield Array[1] (MWA) and the Low Frequency Array[2] (LOFAR) may reveal details about reionization. Future observations will test our current theoretical understanding, potentially leading to surprises about the first stars, reionization, or even fundamental physics such as the nature of dark matter and dark energy.

The aim of this thesis is both to improve our theoretical understanding of cosmology and the high-redshift universe and to identify promising directions for future observations. Chapters 2-7 are comprised of original research on topics including intensity mapping of high-redshift galaxies, the impact of the first galaxies on the intergalactic medium, a possible X-ray contribution to reionization, and the physics which sets the density profiles of dark matter halos.

[1]http://www.haystack.mit.edu/ast/arrays/mwa

[2]http://www.lofar.org

1.1 Galaxy Intensity Mapping

Radio astronomers will soon produce 3-dimensional maps of the universe with redshifted 21cm line emission from neutral hydrogen in galaxies (see Pritchard & Loeb 2012, and references therein). Rather than resolving individual objects, these experiments will measure spatial fluctuations in the cumulative 21cm emission from *all sources*. For this reason the technique is known as "intensity mapping."

In Chapter 2, we propose intensity mapping of galaxies in emission lines besides 21cm. Using additional lines has the potential to provide valuable information about galaxy evolution and the epoch of reionization. It will be especially useful for studying high-redshift galaxies that are too faint to detect individually, but can be detected through the total signal from many sources. Compared with 21cm observations, other lines present the challenge that multiple lines with similar wavelengths can contaminate the observed signal. We demonstrate that it is possible to eliminate this contamination by cross correlating different spectral lines from the same galaxies. We also perform analytic calculations to estimate the strength of the intensity mapping signal, and derive an expression for the experimental uncertainty given a particular set of instrumental specifications. We describe hypothetical observatories that could measure the signal from various spectral lines including those from carbon monoxide and oxygen. In Chapter 3, we use cosmological simulations to create mock data for intensity mapping observations. We find that the observations could be performed successfully, as predicted in the analytic work.

1.2 Cosmological Constraints from 21cm Intensity Mapping

By making precise measurements of the matter power spectrum, intensity mapping of 21cm radiation after reionization has the potential to put tight constraints on cosmological parameters. In Chapter 4, we present results utilizing the Fisher matrix formalism to produce detailed forecasts of how accurately futuristic instruments could constrain these parameters. We find that 21cm intensity mapping can improve constraints on the dark energy density and the neutrino mass by more than an order of magnitude when compared with Planck alone. We also show how these results depend on various characteristics of the observations such as instrumental noise and bandwidth. This work will help to guide the development of future experiments.

1.3 Gauging the X-ray Contribution to Reionization with the kSZ Effect

In the most popular models of cosmic reionization, the IGM is assumed to be ionized by ultraviolet (UV) photons produced by stars in the early universe. However, it is possible that X-ray sources also provided a significant contribution. Because X-rays have a large mean-free-path through the neutral IGM, they would introduce a smooth, partial ionization in between the sharp-edged bubbles created by UV photons.

In Chapter 5, we present semi-numerical simulations of reionization including X-rays and UV photons. We use these simulations to determine how an X-ray contribution

affects the CMB due to the kinetic Sunyaev-Zel'dovich (kSZ) effect. Due to the smoother topology of reionization caused by X-rays, the angular power spectrum of CMB temperature anisotropies is reduced. We examine a number of different reionization scenarios with and without X-rays and find that even a 10% contribution from X-rays to reionization results in lower values of the power spectrum than all of the UV-only cases tested. These results and techniques can be used to interpret measurements of the kSZ power spectrum from the Atacama Cosmology Telescope (ACT), the South Pole Telescope (SPT), and other future instruments.

1.4 Impact of the Baryon-Dark Matter Relative Velocity on the First Stars

It was recently discovered that the relative motion of dark matter and baryonic material had a significant impact on star formation in the early universe (Tseliakhovich & Hirata 2010). Stars form when gas cools and condenses in the gravitational potential wells of dark matter halos. In regions with high relative velocity, gas was able to flow out of these potential wells suppressing star formation.

In Chapter 6, we present the first accurate large-scale cosmological simulations which take this velocity effect into account. We utilize a semi-numerical scheme to follow the 3-dimensional distribution of the first galaxies and their impact on the intergalactic medium (IGM) over cosmic time. Due to the coherence of the relative velocity on a 100 Mpc scale (corresponding to 0.5 degrees at $z = 20$), we find large regions where the density of galaxies is greatly reduced.

We use the simulations to compute the spatial fluctuations in 21cm emission from neutral hydrogen, which could be measured with future low-frequency radio telescopes. In the large, high-relative velocity regions with suppressed star formation, the IGM is much colder. This leads to greatly enhanced fluctuations in the 21cm signal on a scale of 0.5 degrees. This new result suggests that it may be much easier than previously thought to detect the signature of the first stars.

1.5 Density Profiles of Dark Matter Halos

Cosmological simulations make predictions for both the abundance and structure of dark matter halos, but we still lack a complete analytic description of the physical processes that set their density profiles. In Chapter 7, we investigate the possibility that the physical origin of the density structure of dark matter halos can be understood, at least in part, in terms of gravitational collapse from simple (i.e. non-cosmological) initial conditions. To explore this idea we ran simulations of gravitational collapse from cold (zero kinetic energy) and spherically symmetric distributions of particles. This was accomplished with the publicly available N-body code GADGET. We are able to describe the equilibrium states of these simulations in terms of fairly simple physics, which motivates a new model for the distribution function, $f(E, L)$. We find that the pseudo-phase-space density in the final states scales roughly the same as it does in dark matter halos, $\rho/\sigma^3 \propto r^{-1.875}$. This suggests a link between our simple collapse model and dark matter halo formation in the cosmological context.

Chapter 2

Measuring the 3D Clustering of Undetected Galaxies Through Cross Correlation of their Cumulative Flux Fluctuations from Multiple Spectral Lines

E. Visbal & A. Loeb *Journal of Cosmology and Astroparticle Physics*, Issue 11, ID 016, 2010

Abstract

We discuss a method for detecting the emission from high redshift galaxies by cross correlating flux fluctuations from multiple spectral lines. If one can fit and subtract away the continuum emission with a smooth function of frequency, the remaining signal contains fluctuations of flux with frequency and angle from line emitting galaxies. Over a particular small range of observed frequencies, these fluctuations will originate from sources corresponding to a series of different redshifts, one for each emission line. It is possible to statistically isolate the fluctuations at a particular redshift by cross correlating emission originating from the same redshift, but in different emission lines. This technique will allow detection of clustering fluctuations from the faintest galaxies which individually cannot be detected, but which contribute substantially to the total signal due to their large numbers. We describe these fluctuations quantitatively through the line cross power spectrum. As an example of a particular application of this technique, we calculate the signal-to-noise ratio for a measurement of the cross power spectrum of the OI(63 μm) and OIII(52 μm) fine structure lines with the proposed Space Infrared Telescope for Cosmology and Astrophysics (SPICA). We find that the cross power spectrum can be measured beyond a redshift of $z = 8$. Such observations could constrain the evolution of the metallicity, bias, and duty cycle of faint galaxies at high redshifts and may also be sensitive to the reionization history through its effect on the minimum mass of galaxies. As another example of this technique, we calculate the signal-to-noise ratio for the cross power spectrum of CO line emission measured with a large ground based telescope like the Cornell Caltech Atacama Telescope (CCAT) and 21-cm radiation originating from hydrogen in galaxies after reionization with an

interferometer similar in scale to the Murchison Widefield Array (MWA), but optimized for post-reionization redshifts.

2.1 Introduction

Atoms and molecules in the interstellar medium of galaxies produce line emission at particular rest frame wavelengths (Binney & Merrifield 1998). For galaxies at cosmological distances, this line emission is redshifted by a factor of $(1 + z)$ due to the expansion of the universe. Ignoring peculiar velocities, the redshift of a galaxy corresponds to its distance from the observer along the line of sight. Thus, if the redshift and angular position of many galaxies are measured, a 3D map of their distribution can be constructed. Such 3D maps contain a wealth of information about galaxies and the underlying cosmic density field which they trace. Examples of recent galaxy surveys include the Sloan Digital Sky Survey[1], the 2dF Galaxy Redshift Survey[2], the DEEP2 Redshift Survey[3], and the VIMOS-VLT Deep Survey[4].

In this work, we discuss a different way of mapping the large scale structure of the universe, namely by measuring the fluctuations in line emission from galaxies, including also those too faint to be individually detected. If the line emission fluctuations in observed frequency and angle are associated with a particular line, they can be translated

[1]http://www.sdss.org/

[2]http://www2.aao.gov.au/2dFGRS/

[3]http://deep.berkeley.edu/ marc/deep/index.html

[4]http://www.oamp.fr/virmos/vvds.htm

into a 3D map. Even though individual faint sources cannot be distinguished from noise, the cumulative emission from many such sources contributes substantially to the fluctuations over large scales. These fluctuations will trace the large scale structure of the universe and can be analyzed statistically. By contrast, a traditional galaxy survey only contains the positions of galaxies detected at high significance, and discards information from fainter sources.

Similar observations are being planned with the 21cm line of neutral hydrogen using instruments such as MWA[5], LOFAR[6], PAPER[7], 21CMA[8], and SKA[9]. These experiments will obtain angle and frequency information for large areas on the sky and will produce 3D maps of the neutral hydrogen throughout the universe. The raw signal will contain both bright sources of foreground emission (the largest being synchrotron emission from our galaxy), as well as the cosmological 21cm line signal. Since the cosmological signal varies rapidly with frequency, it is expected that the foregrounds, which are smooth in the frequency direction, can be subtracted off (Morales 2005; Wang et al. 2006; McQuinn et al. 2006a; Liu et al. 2009). If this is accomplished, one will be left with only the fluctuations in 21cm line emission.

During the epoch of reionization the 21cm signal originates from the neutral hydrogen in the intergalactic medium. HII regions ionized by stars or quasars will appear

[5]http://www.haystack.mit.edu/ast/arrays/mwa

[6]http://www.lofar.org

[7]http://www.astro.berkeley.edu/dbacker/EoR

[8]http://web.phys.cmu.edu/ past

[9]http://www.skatelescope.org

as bubbles in the signal, creating a "Swiss cheese" topology. On the other hand, the post-reionization 21cm signal is expected to originate from dense galactic regions which are self-shielded from the ultraviolet background (Wyithe & Loeb 2009; Loeb & Wyithe 2008). Thus, the post-reionization signal is very similar to other galactic emission lines. Recently, statistical analysis of the post-reionization 21cm signal has been attempted (Chang et al. 2010). Another idea related to the present work is the cross correlation of the 21cm line with the 92cm line of deuterium (Sigurdson & Furlanetto 2006).

One important issue which does not arise in 21cm observations is confusion from multiple lines. With multiple lines of different rest frame wavelengths the intensity at a particular observed frequency corresponds to emission from multiple redshifts, one for each emission line. With both angle and frequency information, the total emission corresponds to a superposition of 3D maps of galaxies at different redshifts.

Fortunately, it is possible to statistically isolate the fluctuations from a particular redshift by cross correlating the emission from two different lines. If one compares the fluctuations at two different frequencies, which correspond to the same redshift in two different emission lines, their fluctuations will be strongly correlated. However, the signal from any other lines arises from galaxies at different redshifts which are very far apart and thus will have much weaker correlation.

We propose observations of these cross correlations, and show that they can be described quantitatively by the cross power spectrum of line emission. This technique is particularly suitable for learning about a large sample of faint sources which in a reasonable amount of time can only be detected statistically. As an illustrative example, we calculate the signal-to-noise ratio of the line cross power spectrum which could be

measured by the proposed Space Infrared Telescope for Cosmology and Astrophysics (SPICA) (Swinyard et al. 2009). We find that with SPICA, our technique can potentially probe line emission from faint galaxies beyond a redshift $z = 8$. This would contain information about the evolution of distant galaxies including their metallicity, bias and duty cycle. Such observations could also potentially constrain the reionization history based on the minimum mass of galaxies. As another example, we consider cross correlating CO line emission observed with the Cornell Caltech Atacama Telescope (CCAT)[10] and 21cm radiation from galaxies measured by an interferometer similar in scale to the Murchison Widefield Array (MWA) (Bowman et al. 2009), but optimized for post-reionization redshifts.

The paper is organized as follows. In Section 2.2 we introduce and describe the 3D line cross power spectrum technique. In Sections 2.3 and 2.4 we discuss SPICA and CCAT plus our MWA-like interferometer respectively, which we use to use illustrate the effectiveness of the proposed technique. Finally, we discuss and summarize our conclusions in Section 2.5. Throughout, we assume a ΛCDM cosmology with $\Omega_\Lambda = 0.73$, $\Omega_m = 0.27$, $\Omega_b = 0.0456$, $h = 0.7$, and $\sigma_8 = 0.81$ (Komatsu et al. 2011).

[10]http://www.submm.org/

2.2 Method

2.2.1 Line Cross Power Spectrum

We begin by introducing the cross power spectrum of line emission. We assume an observation that records both spatial and spectral data over a patch of the sky. We further assume that the spectrally smooth foreground, including galaxy continuum emission can be subtracted accurately. This could be done by fitting a smooth function of frequency to the data in different locations on the sky as has been suggested for 21cm observations (Morales 2005; Wang et al. 2006; McQuinn et al. 2006a; Liu et al. 2009). Subtracting such a fit from the data would remove only the signal which varies slowly as a function of frequency. If we associate the fluctuations with emission in a particular line, we can map each pixel to a location in redshift space.

The fluctuation signal at a particular angle on the sky and observed frequency, $\Delta S(\theta_1, \theta_2, \nu) = S(\theta_1, \theta_2, \nu) - \bar{S}$, will have several different components,

$$\Delta S_1(\theta_1, \theta_2, \nu) = \Delta S_{\rm line1} + \Delta S_{\rm noise} + \Delta S_{\rm badline1} + \Delta S_{\rm badline2} + \Delta S_{\rm badline3} + \dots \qquad (2.1)$$

These include fluctuations in line emission from galaxies at the target redshift in the associated line, detector noise, and emission from galaxies at different redshifts in other lines. We term these "bad lines".

To estimate the flux amplitude of line emission fluctuations we assume that galaxies trace the underlying cosmological density field. If we consider linear scales, it follows that the line fluctuations due to galaxy clustering are given by $\Delta S = \bar{S}\bar{b}\delta(\vec{r})$, where $\bar{S}$ is the average line signal, $\bar{b}$ is the luminosity weighted average galaxy bias, and $\delta(\vec{r})$ is the cosmological over-density at a location $\vec{r}$ corresponding to the observed angle and

frequency. For the moment we ignore Poisson fluctuations due to the discrete nature of galaxies, which will be introduced later. We describe our method for estimating the average signal and bias of emission lines in the next subsection.

Ignoring peculiar velocities and using the flat sky approximation (which applies for the small fields of view we consider in this paper), we find,

$$\Delta S_{\rm line1} = \bar{S}_1 \bar{b} \delta(\vec{r}_o + \Delta\theta_1 D_A \hat{\mathbf{i}} + \Delta\theta_2 D_A \hat{\mathbf{j}} + \Delta\nu \tilde{y}_1 \hat{\mathbf{k}}), \tag{2.2}$$

where $\vec{r}_o$ is the comoving position corresponding to the center of the survey, $\Delta\theta_1$ and $\Delta\theta_2$ are the angular offsets from the center of the survey and $\Delta\nu$ is the offset from the central observed frequency, D_A is the angular diameter distance in comoving units, and $\tilde{y}$ is the derivative of comoving distance with respect to observed frequency. This last quantity is given by,

$$\tilde{y} = \frac{d\chi}{d\nu} = \frac{d\chi}{dz}\frac{dz}{d\nu} = \frac{\lambda_r (1+z)^2}{H(z)}, \tag{2.3}$$

where χ is the comoving distance to the observation, ν is the observed frequency, $\lambda_{\rm r}$ is the rest frame wavelength of a line, and $H(z)$ is the Hubble parameter. Here $\hat{\mathbf{i}}$, $\hat{\mathbf{j}}$, and $\hat{\mathbf{k}}$ are Cartesian unit vectors with $\hat{\mathbf{k}}$ pointing along the line of sight of the survey. In Figure 2.1 we show the relation between angle, frequency, and comoving position as a function of redshift.

Similarly, for the bad lines we have,

$$\Delta S_{\rm badline1} = \bar{B}_1 \bar{b}_1 \delta(\vec{r}_o + d_1 \hat{\mathbf{k}} + \Delta\theta_1 D_{A1} \hat{\mathbf{i}} + \Delta\theta_2 D_{A1} \hat{\mathbf{j}} + \Delta\nu \tilde{y}_{b1} \hat{\mathbf{k}}), \tag{2.4}$$

where d_1 is the shift along the line of sight due to each bad line being at a different redshift than the target line, $\bar{B}_1$ is the average signal from the bad line, and $\bar{b}_1$ is the average bias of the galaxies emitting in the bad line. Note that the angular diameter

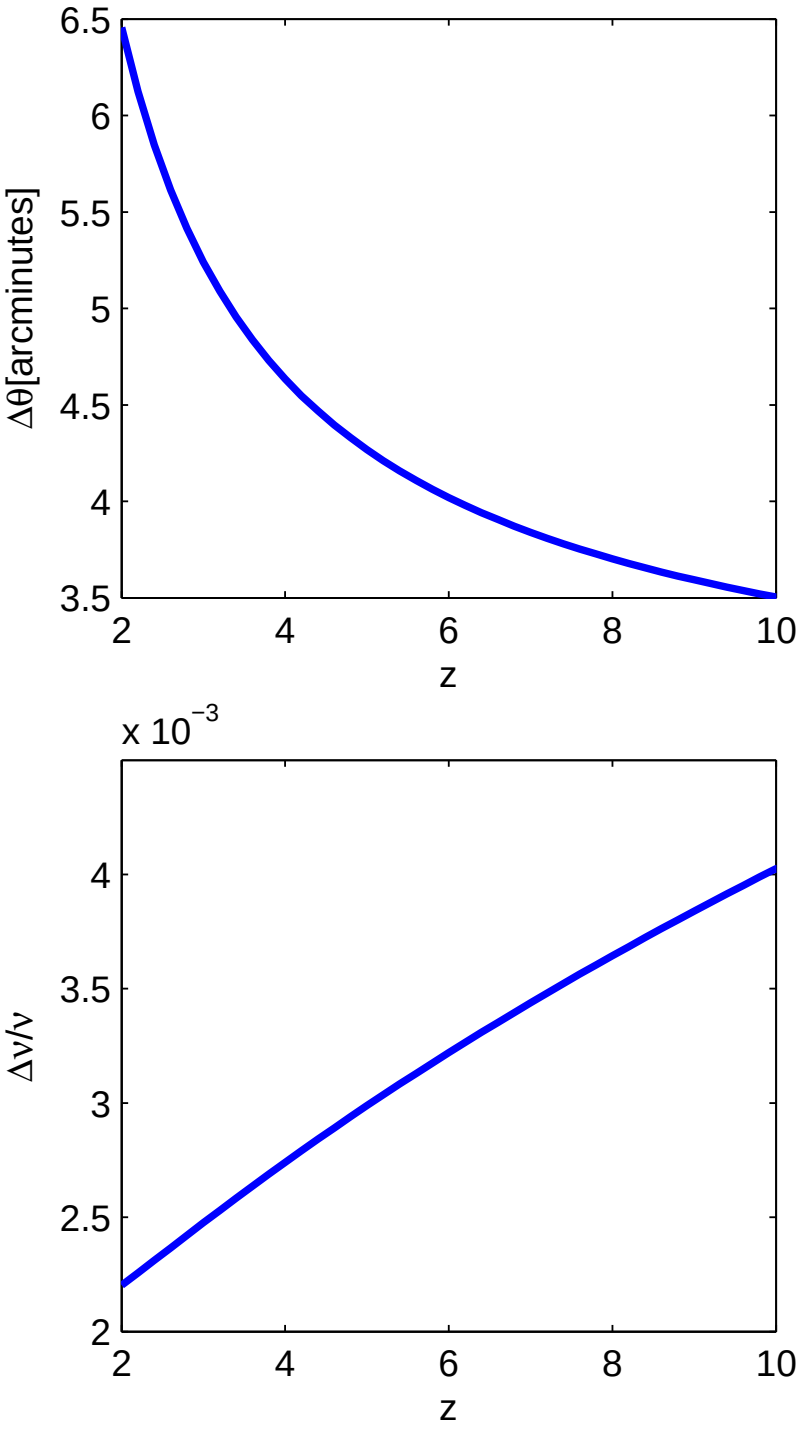

Figure 2.1.—: The angle and frequency range corresponding to 10 comoving Mpc.

distance and derivative of comoving distance with respect to observed frequency are evaluated at the redshift of the bad line galaxies which we denoted with subscripts.

Instead of angle and frequency we label our observed pixels in terms of the location in space corresponding to our target line $(\vec{r}_o, \vec{r})$, where $\vec{r} = x\hat{\mathbf{i}} + y\hat{\mathbf{j}} + z\hat{\mathbf{k}}$ is the distance from the center of the survey, with $x = \Delta\theta_1 D_A$, $y = \Delta\theta_2 D_A$, and $z = \Delta\nu\tilde{y}$. We rewrite Eq. (2.1) using these coordinates,

$$\Delta S_1(\vec{r}_o, \vec{r}) = \Delta S_{\rm noise} + \bar{S}_1\bar{b}\delta(\vec{r}_o+\vec{r}) + \bar{B}_1\bar{b}_1\delta(\vec{r}_o+d_1\hat{\mathbf{k}}+\vec{r'}_1) + \bar{B}_2\bar{b}_2\delta(\vec{r}_o+d_2\hat{\mathbf{k}}+\vec{r'}_2)+\ldots, \quad (2.5)$$

where $\vec{r'}_n = c_{xn}x\hat{\mathbf{i}} + c_{yn}y\hat{\mathbf{j}} + c_{zn}z\hat{\mathbf{k}}$ for the n'th bad line. The constants c_{xn}, c_{yn} and c_{zn} reflect the cosmological stretching of the data cube at different redshifts, which are given by $c_{xn} = c_{yn} = D_{An}/D_A$ and $c_{zn} = \tilde{y}_{bn}/\tilde{y}_1$.

As mentioned in the Introduction, we can statistically remove the contribution from bad lines by cross correlating the fluctuations from two different lines originating from nearby locations. We define the 2-point cross correlation function as,

$$\xi_{1,2}(\vec{r}) = \langle \Delta S_1(\vec{r}_o, \vec{x})\Delta S_2(\vec{r}_o, \vec{r}+\vec{x})\rangle, \quad (2.6)$$

and the cross correlation power spectrum as its Fourier transform,

$$P_{1,2}(\vec{k}) = \int d^3\vec{r}\xi_{1,2}(\vec{r})e^{i\vec{k}\cdot\vec{r}}. \quad (2.7)$$

Note that the noise in different pixels will be uncorrelated and that bad line emission from different lines will in general originate from galaxies at different redshifts which will be essentially uncorrelated. Thus, we expect the cross correlation function and power spectrum to depend only on galaxies at the target location,

$$\xi_{1,2}(\vec{r}) = \langle \Delta S_{\rm line1}(\vec{r}_o, \vec{x})\Delta S_{\rm line2}(\vec{r}_o, \vec{r}+\vec{x})\rangle = \bar{S}_1\bar{S}_2\bar{b}^2\langle\delta(\vec{x})\delta(\vec{r}+\vec{x})\rangle = \bar{S}_1\bar{S}_2\bar{b}^2\xi(\vec{r}), \quad (2.8)$$

where $\xi(\vec{r})$ is the cosmological matter correlation function.

2.2.2 Average Signal, Average Bias, and Shot-noise

To calculate the average signal and bias for a particular line, we assume that the luminosity of a galaxy in a particular line is a function of the mass of the halo hosting it: $L = L(M)$. We also assume that galaxies only emit a significant amount of radiation over some fraction of cosmic time, the duty cycle, $\epsilon_{\rm duty}$. The average signal is then (in erg/s/cm^2/Hz/Sr),

$$\bar{S} = \int_{M_{\rm min}}^{\infty} dM \frac{L(M)}{4\pi D_L^2} \epsilon_{\rm duty} \frac{dn}{dM} \tilde{y} D_A^2, \tag{2.9}$$

where $M_{\rm min}$ is the minimum mass of dark matter halos which can host galaxies, and $dn(M)$ is the comoving density of halos of mass between M and $M + dM$. Before reionization $M_{\rm min}$ is set by the requirement that gas can cool efficiently via atomic hydrogen cooling, corresponding to halos with virial temperatures greater than 10^4K, whereas after reionization this is the threshold for assembling heated gas out of the photo-ionized intergalactic medium, corresponding to a minimum virial temperature of 10^5K (Mesinger & Dijkstra 2008; Efstathiou 1992; Thoul & Weinberg 1996; Hui & Gnedin 1997; Wyithe & Loeb 2006; Shapiro et al. 1994; Babich & Loeb 2006; Haiman et al. 1997a). $L(M)$ is the line luminosity (in erg/s) from one dark matter halo of mass M, D_L is the cosmological luminosity distance, and $\frac{dn}{dM}$ is the halo mass function in units of comoving density per mass (Sheth et al. 2001).

Assuming that the flux in a line from a halo is proportional to the mass of the halo, the average bias is given by,

$$\bar{b} = \frac{\int_{M_{\rm min}}^{\infty} \frac{dn}{dM} b(M,z) M dM}{\int_{M_{\rm min}}^{\infty} \frac{dn}{dM} M dM}, \tag{2.10}$$

where $b(M, z)$ is the bias associated with halos of mass M at redshift z (Sheth et al. 2001). We can calculate the average signal and bias for both the target lines and bad

lines using Eqs. (2.9) and (2.10). Note that both of these quantities must be calculated at the appropriate redshifts for the different bad lines.

In addition to fluctuations due to the clustering of galaxies, there are also Poisson fluctuations arising from the discrete nature of galaxies which sample the cosmological density field. These fluctuations are unimportant on very large scales, but dominate on the smallest scales. Given our model of the line fluctuations, it is straightforward to show from Eqs. (2.6) and (2.7) that the cross power spectrum of galaxy line emission from two lines is given by,

$$P_{1,2}(\vec{k}) = \bar{S}_1 \bar{S}_2 \bar{b}^2 P(\vec{k}) + P_{\rm shot}, \tag{2.11}$$

where $P(\vec{k})$ is the cosmic power spectrum of density fluctuations and the Poisson or shot-noise power spectrum due to the discrete nature of galaxies is given by,

$$P_{\rm shot} = \int_{M_{min}}^{\infty} dM \left(\frac{L_1(M)}{4\pi D_L^2}\right)\left(\frac{L_2(M)}{4\pi D_L^2}\right)\epsilon_{\rm duty}\frac{dn}{dM}(\tilde{y}_1 D_A^2)(\tilde{y}_2 D_A^2), \tag{2.12}$$

where the indices 1 and 2 denote lines 1 and 2.

2.2.3 Cross Power Spectrum Estimation

Next we introduce an unbiased estimator of the cross power spectrum and use it to derive an expression for the variance in its measurement. We begin by defining the Fourier amplitude of the fluctuations,

$$f_{\vec{k}} = \int d^3\vec{r}\,\Delta S(\vec{r_o},\vec{r}) W(\vec{r}) e^{i\vec{k}\cdot\vec{r}}, \tag{2.13}$$

where $W(\vec{r})$ is a window function which is constant over the survey volume and zero outside the survey volume. It is normalized such that, $\int W d^3\vec{r} = 1$. The center of the survey volume is denoted by $\vec{r_o}$.

The Fourier amplitude can be broken up into the different sources of fluctuations,

$$f_{\vec{k}}^{(1)} = f_{\vec{k}}^{S1} + f_{\vec{k}}^{n1} + f_{\vec{k}}^{B1} + f_{\vec{k}}^{B2} \ldots, \tag{2.14}$$

the galaxy line fluctuations at the target redshift, detector noise, and each of the bad lines coming from different redshifts.

Using the convolution theorem, we rewrite the Fourier amplitude for the target line fluctuations as,

$$f_{\vec{k}}^{S1} = \frac{1}{(2\pi)^3} \int d^3\vec{k'} \bar{S}_1 \bar{b} \delta(\vec{k'}) W(\vec{k'} - \vec{k}) e^{-i\vec{k'}\cdot\vec{r_o}}. \tag{2.15}$$

A rectangular window function in real space has the k-space form,

$$W(k_x, k_y, k_z) = \frac{\sin(k_x a_x/2)}{(k_x a_x/2)} \frac{\sin(k_y a_y/2)}{(k_y a_y/2)} \frac{\sin(k_z a_z/2)}{(k_z a_z/2)}, \tag{2.16}$$

where a_x, a_y, and a_z are the spatial dimensions of the survey along the x, y, and z axes.

The Fourier amplitude defined above can now be used to estimate the cross power spectrum of different lines. If we cross correlate the Fourier amplitude of two different lines corresponding to the same location, $\langle f_{\vec{k}}^{(1)} f_{\vec{k}}^{(2)*} \rangle$, all terms except for the target lines' fluctuations are greatly suppressed as discussed above. Ignoring momentarily the fluctuations due to the discrete nature of galaxies, this results in,

$$\langle f_{\vec{k}}^{(1)} f_{\vec{k}}^{(2)*} \rangle = \frac{1}{(2\pi)^6} \int\int d^3\vec{k'} d^3\vec{k''} W(\vec{k'} - \vec{k}) W(\vec{k''} - \vec{k})^* \bar{S}_1 \bar{S}_2 \bar{b}^2 \langle \delta(\vec{k'}) \delta(\vec{k''})^* \rangle e^{i(\vec{k''} - \vec{k'})\cdot\vec{r_o}}. \tag{2.17}$$

Note that the cosmological power spectrum is defined by,

$$\langle \delta(\vec{k'}) \delta(\vec{k''})^* \rangle = (2\pi)^3 \delta^D(\vec{k'} - \vec{k''}) P(k'), \tag{2.18}$$

and that for a large survey $|W(\vec{k'} - \vec{k})|^2 \approx (2\pi)^3 \delta^D(\vec{k'} - \vec{k})/V$, where δ^D is a Dirac delta function and V is the volume of the survey. With these substitutions we find that,

$$\langle f_{\vec{k}}^{(1)} f_{\vec{k}}^{(2)*} \rangle = \bar{S}_1 \bar{S}_2 \bar{b}^2 P(\vec{k})/V, \tag{2.19}$$

which is simply the clustering component of the cross power spectrum divided by the volume of the survey. When Poisson fluctuations due to the discrete nature of galaxies are included it is straightforward to show that this will give the total line cross power spectrum divided by the volume of the survey. Thus, we take our unbiased estimator to be the real part of this quantity times the volume of the survey,

$$\hat{P}_{1,2} = \frac{V}{2}(f_{\vec{k}}^{(1)} f_{\vec{k}}^{(2)*} + f_{\vec{k}}^{(1)*} f_{\vec{k}}^{(2)}). \tag{2.20}$$

Equipped with an estimator, we can now calculate the variance on a measurement of the cross power spectrum. The error is given by,

$$\delta P_{1,2}^2 = \langle \hat{P}_{1,2}^2 \rangle - \langle \hat{P}_{1,2} \rangle^2. \tag{2.21}$$

With this estimator we find (see Section 2.6),

$$\delta P_{1,2}^2 = \frac{1}{2}(P_{1,2}^2 + P_{1\text{total}} P_{2\text{total}}), \tag{2.22}$$

where $P_{1\text{total}}$ is the total power spectrum corresponding to the first line being cross correlated,

$$P_{1\text{total}} = \bar{S}_1^2 \bar{b}^2 P(\vec{k}, z_{\text{target}}) + P_{\text{noise}} + \bar{B}_1^2 \bar{b}_1^2 \frac{P(\vec{k_1'}, z_1)}{(c_{x1} c_{y1} c_{z1})} + \bar{B}_2^2 \bar{b}_2^2 \frac{P(\vec{k_2'}, z_2)}{(c_{x2} c_{y2} c_{z2})} \ldots . \tag{2.23}$$

Here we have the total power spectrum for each line, which includes the line fluctuation power spectrum of the line at the target redshift; a power spectrum due to the detector noise fluctuations; and the power spectrum for each of the bad lines. The c's which appear in the denominators of the bad line power spectra result from the fact that the volume corresponding to the field of view on the sky and frequency interval of the survey is different for the location of each bad line. Similarly, the wave-number for the various bad lines is changed to $\vec{k_1'} = \frac{k_x}{c_{x1}}\hat{\mathbf{i}} + \frac{k_y}{c_{y1}}\hat{\mathbf{j}} + \frac{k_z}{c_{z1}}\hat{\mathbf{k}}$. To avoid an overly cumbersome equation,

we have not explicitly written the shot-noise power spectra. Note that for each clustering power spectrum which appears in this equation there is a corresponding $P_{\rm shot}$ given by Eq. (2.12).

Up to this point we have only been dealing with the error in an estimate of one k-mode. However, one can exploit the isotropy of the universe and average the value of the cross power spectrum for a thin spherical shell in k-space. The error on the cross power spectrum changes as a function of angle in k-space (due to $\vec{k'}$ appearing in Eq. 2.23). One should take a weighted average, where modes in the shell with a better signal-to-noise ratio are weighted more heavily. The optimal way to do this is an inverse variance weighted average of the cross power spectrum in the shell. It follows that the error on the averaged cross power spectrum is given by,

$$\delta P(k)_{1,2} = \left(\sum_{\rm shell} \frac{1}{\delta P_{1,2}(\vec{k})^2} \right)^{-1/2}, \tag{2.24}$$

where we are summing over all of the modes in a shell. Note that the resolution of k-space is given by $2\pi/a_i$ in the i'th direction for Cartesian coordinates. We only add modes in the upper half-plane because the power spectrum is the Fourier transform of a real-valued function. The maximum k-modes available are set by the angular and frequency resolution of the observations, while the minimum values are set by the dimensions of the survey volume.

2.2.4 Multiple Lines

One could also combine the information from the cross correlations of many lines. For instance, one could do a weighted average of the cross power spectra of all combinations

of available lines,

$$P_{\rm AVG} = w_{1,2}\hat{P}_{1,2} + w_{1,3}\hat{P}_{1,3} + w_{2,3}\hat{P}_{2,3}\ldots \tag{2.25}$$

where the w's are weighting factors which would need to be highest for the pairs of lines with the highest signal-to-noise ratio. This helps to detect the faintest galaxies.

2.2.5 Remaining Confusion

As discussed above, if one cross correlates fluctuations from two different lines at frequencies corresponding to a target redshift, each will have its own set of bad lines from various other redshifts. If a bad line from the first line originates from a redshift very close to a bad line from the second line there may be a spurious signal in the cross correlation of the fluctuations which is not from the target redshift.

Fortunately, we do not expect this type spurious signal to be very problematic. If a pair of spurious bad lines is present one should be able to cross correlate this pair directly (then the target lines will appear as a spurious pair). As long as the fluctuations from the spurious pair are not much larger than the target lines, one will be able to accurately subtract off their contribution. In the examples with SPICA considered below, we find that after all of the bright sources which can be individually detected are removed, the fluctuations from each bad line are smaller or comparable to the fluctuations in the lines we cross correlate.

A factor which will aid in subtracting off this spurious signal is that (ignoring redshift space distortions), the cross power spectrum from the target lines will only depend on the magnitude of $\vec{k}$ and not the direction. However, the signal from the spurious pair will change with the direction of the k-mode due to the stretching of the

data cube (i.e. they have different c_x, c_y, and c_z values defined above).

There is an additional effect which will further eliminate this problem. Two problematic bad lines will never originate from exactly the same redshift. Since they are from slightly different redshifts, the 3D data cube corresponding to the location of the emitting galaxies will be stretched by different amounts. That means when we cross correlate the same $\vec{k}$ in the target lines they will have slightly different $\vec{k}$ values in each of the problematic bad lines. Since k-modes which have different $\vec{k}$ are uncorrelated, this will serve to reduce the spurious signal.

2.3 SPICA

2.3.1 Instrument

We use the proposed Space Infrared Telescope for Cosmology and Astrophysics (SPICA) (Swinyard et al. 2009) as an example of an instrument which could be used to cross correlate line emission as discussed above. SPICA is a 3.5 meter space-borne infrared telescope planned for launch in 2017. It will be cooled below 5K, providing measurements which are orders of magnitude more sensitive than those from current instruments. We also consider the Atacama Large Millimeter Array (ALMA)[11], but find that it is not well suited for the cross correlations discussed in this paper. Due to the small field of view and high angular resolution of this instrument, after the detectable galaxies have been removed, we find that remaining statistical signal cannot be detected above the detector

[11]https://science.nrao.edu/facilities/alma

noise.

We focus on SPICA's proposed high performance spectrometer μ-spec (H. Moseley, private communication 2009). This instrument will provide background limited sensitivity with wavelength coverage from $250 - 700\mu m$. A number of μ-spec units will be combined to record both angle and spectral data in each pointing, which will be perfectly suited for the cross correlation technique described above. We assume that spectra for 100 diffraction limited pixels can be measured simultaneously with a resolving power of $R = \nu/\Delta\nu = 1000$, this represents an optimistic design. We expect that most of the signal contributed by galaxies which cannot be observed directly will originate from lines too narrow to be resolved with this resolution. We have checked this by associating halos of a given mass with a corresponding rotational velocity.

Since our observations are background limited, the noise fluctuations will be dominated by shot-noise from the finite number photons originating from the smooth foregrounds which we assume have been subtracted off. In the wavelength range considered, the dominant foregrounds are dust emission from the Milky Way galaxy and zodiacal light from the solar system. We use COBE FIRAS data to estimate the brightness of the total foregrounds in the faintest 10% region of the sky (Fixsen et al. 1998a). If the observation has pixels with solid angle $\Delta\Omega$ and frequency width $\Delta\nu$, the foreground flux fluctuations (in erg/s/cm^2/Sr/Hz) in one pixel will be,

$$\Delta S_{\rm noise} = \frac{E_\gamma}{At\Delta\Omega\Delta\nu}(N_\gamma - \bar{N}_\gamma), \tag{2.26}$$

where E_γ is the energy per photon coming from the foreground, A is the area of the primary dish of the telescope, t is the integration time, N_γ is the number of photons gathered in a pixel during the integration time, and $\bar{N}_\gamma$ is the average number of photons

that are collected from one pixel during the integration time. From Poisson statistics it follows that the variance due to the foregrounds in a pixel is given by,

$$\sigma^2_{\rm noise} = \frac{\bar{S}_{\rm fg} E_\gamma}{At\Delta\Omega\Delta\nu}, \tag{2.27}$$

where $\bar{S}_{\rm fg}$ is the average surface brightness from the foregrounds (in erg/s/cm^2/Sr/Hz). One can then derive (see Section 2.6) the noise power spectrum,

$$P_{\rm noise} = \bar{S}_{\rm fg1} \frac{E_\gamma D_A^2 \tilde{y}}{At}. \tag{2.28}$$

In deriving this equation we have implicitly assumed that the arrival of individual photons are statistically independent from one another. This will be true for foreground radiation at the wavelengths we consider with SPICA. However, at wavelengths longer than $\sim$ 1mm this assumption might no longer apply. In general, one needs to use the full equation for photon noise which includes correlations from photons arriving in the same quantum state. This correlation in the arrival time of photons, so called "photon bunching", will increase the noise calculated with simple Poisson statistics for individual photons (Zmuidzinas 2003; Loeb 2008).

2.3.2 Relevant Lines

Atomic and ionic fine-structure lines in the far infrared are very important in cooling the gas in galaxies. They produce bright emission lines which can be seen in distant sources. For galaxies with redshifts of $z \gtrsim 5$ many of these lines will be observed within SPICA's wavelength range.

In order to estimate the amplitude of line emission fluctuations we assume a linear relationship between line luminosity, L, and star formation rate, $\dot{M}_*$. The line luminosity

from a galaxy is then given by $L = \dot{M}_* \cdot R$, where R is the ratio between star formation rate and line luminosity for a particular line. This is similar to existing relations in different bands (see Kennicutt 1998) and was used in the past to estimate the strength of the galactic lines (Righi et al. 2008). For the first 7 lines in Table 2.1, we use the same ratios, R, as Righi et al. (2008) which were calculated by taking the geometric average of the ratios from an observational sample of lower redshift galaxies (Malhotra et al. 2001).

Table 2.1

Species	Emission Wavelength[μm]	R[$L_\odot/(M_\odot/yr)$]
CII	158	6.0×10^6
OI	145	3.3×10^5
NII	122	7.9×10^5
OIII	88	2.3×10^6
OI	63	3.8×10^6
NIII	57	2.4×10^6
OIII	52	3.0×10^6
CO(1-0)	2610	3.7×10^3
CO(2-1)	1300	2.8×10^4
CO(3-2)	866	7.0×10^4
CO(4-3)	651	9.7×10^4
CO(5-4)	521	9.6×10^4
CO(6-5)	434	9.5×10^4
CO(7-6)	372	8.9×10^4
CO(8-7)	325	7.7×10^4

Continued on Next Page...

Table 2.1 – Continued

Species	Emission Wavelength[μm]	R[$L_\odot/(M_\odot/yr)$]
CO(9-8)	289	6.9×10^4
CO(10-9)	260	5.3×10^4
CO(11-10)	237	3.8×10^4
CO(12-11)	217	2.6×10^4
CO(13-12)	200	1.4×10^4
CI	610	1.4×10^4
CI	371	4.8×10^4
NII	205	2.5×10^5

Table 2.1:: Assumed ratio between star formation rate, $\dot{M}_*$, and line luminosity, L, for various lines. For the first 7 lines this ratio is measured from a sample of low redshift galaxies. The other lines have been calibrated based the galaxy M82. We obtain the luminosity in a line from: $L[L_\odot] = R \cdot \dot{M}_*[M_\odot \text{ yr}^{-1}]$.

We also list line strengths for CO lines which could be observed with other instruments (see Section 2.4). For transitions below CO(8-7), we use the same R values as Righi et al. (2008), which are calibrated from observations of the galaxy M82 (Weiß et al. 2005). For the higher CO transitions we calibrate with the observations of M82 presented in Panuzzo et al. (2010a). The R values of M82 are representative of CO emission from high redshift galaxies (see Figure 1 in Righi et al. 2008).

We calculate the star formation rate in a halo by denoting the fraction of gas in a halo which forms stars as the star formation efficiency, f_*. We then approximate the star formation rate as constant over the duty cycle of the galaxy. Following (Wyithe & Loeb 2006; Loeb et al. 2005; Stark et al. 2007) we write,

$$\dot{M}_*(M) = \frac{f_*(\Omega_b/\Omega_m)M}{\epsilon_{duty} t_H}, \tag{2.29}$$

where $t_H = 0.97[(1+z)/7]^{-3/2}$Gyr is the age of the Universe at the high redshifts of interest. The line luminosity of a galaxy is then given by,

$$L = 6.6 \cdot 10^6 \left(\frac{R}{3.8 \cdot 10^6}\right) \left(\frac{M}{10^{10} M_\odot}\right) \left(\frac{1+z}{7}\right)^{3/2} \frac{f_*}{\epsilon_{\rm duty}} L_\odot. \tag{2.30}$$

2.3.3 Results

To demonstrate the effectiveness of the cross correlation technique, we calculate the signal-to-noise ratio for the line cross power spectrum of OI($63\mu m$) and OIII($52\mu m$) measured with SPICA. Because this technique is most useful for detecting faint galaxies which cannot be individually detected, we assume that all of the pixels containing very bright line emission have been removed. This is done for both the lines we are cross correlating and the bad lines. We assume that all pixels with line emission corresponding to 5σ peaks when compared with the foreground noise are removed. This effectively changes the upper limits of integration in Eqs. (2.9) and (2.10). We find that this only requires removing a small fraction of the available pixels. All lines in Table 2.1 are used as bad lines.

In order to calculate which dark matter halos are bright enough to be removed, we assume that all of the emission from a halo appears in one pixel. We expect this to be

a good approximation, since most of the signal from high redshift galaxies originates in halos with virial radii corresponding to angles smaller than the pixels of the instrument we consider. Additionally, sub-halos which constitute more than $\approx 10\%$ of the parent halo are expected to sink to its center by dynamical friction in less than a Hubble time (Wetzel et al. 2009; Wetzel & White 2010); this implies that each halo will most of the time have one dominant galaxy at its center and only much fainter satellites.

There is another argument which justifies our one pixel assumption for removing the detectable galaxies. For low redshift galaxies contributing to the bad line noise in the power spectrum, we find that the minimum mass of halos which have galaxies that can be directly detected and removed is smaller than halos which host more than one galaxy. The number of galaxies per halo above this mass scales roughly linearly with halo mass (Bullock et al. 2002). Thus, if the galaxies are equally luminous in halos which host multiple galaxies, all of them can be directly detected and removed. When they are not equally luminous most of the signal will originate from the brighter galaxies which will be removed.

In all of our calculations we use the linear power spectrum computed with CAMB[12]. We expect the linear power spectrum to be a good approximation. The smallest scales probed in our examples are still in the linear regime at the redshifts of interest. On these scales we may be in the nonlinear regime of the matter power spectra at lower redshifts which appear in the bad line noise terms. One way to approximate the nonlinear power spectrum is to use the so called Halo Model (see Cooray & Sheth 2002, and references therein). In this treatment, correlations are separated into two terms: the 1-halo term

[12]http://camb.info/

corresponding to correlations between matter in the same halo and the 2-halo term corresponding to correlations between matter in different halos. After removing bright sources we expect the signal to be coming from the center of halos. Thus, the 1-halo contribution to our cross power spectrum will originate only from the shot-noise power spectrum given in Eq. (2.12). The linear power spectrum should give a reasonable approximation to the 2-halo term.

We adopt fiducial values of the duty cycle and star formation efficiency of $\epsilon_{\rm duty} = 0.1$ and $f_* = 0.1$ (Stark et al. 2007). The total observation time is assumed to be 10^6 seconds. During this time we assume that 256 adjacent pointings are taken to provide a mosaic over an area of the sky. Increasing the number of pointings reduces the error in the power spectrum due to sample variance, including noise provided by bad lines, but increases the error due to the detector noise power spectrum since fewer photons are collected in each pointing. For the depth of the survey along the line of sight we assume $\Delta z = 0.1(1+z)$. We assume that the cosmological evolution across this redshift range is negligible.

In Figure 2.2, we plot the OI(63μm) and OIII(52μm) cross power spectrum with error bars. For the plot at $z = 5$, 6 and 7 we have assumed that reionization occurred at a much higher redshift, such that the minimum mass of halos which host galaxies is determined from the Jeans mass in the photo-ionized IGM with a minimum virial temperature of 10^5K (Mesinger & Dijkstra 2008; Efstathiou 1992; Thoul & Weinberg 1996; Hui & Gnedin 1997; Wyithe & Loeb 2006; Shapiro et al. 1994). For the plot at $z = 8$ we assumed that reionization occurred instantaneously at $z = 6$ so that the minimum mass of galaxies at the target redshift is set by the condition that there is efficient atomic hydrogen cooling with a minimum virial temperature of 10^4K (Babich &

Loeb 2006; Haiman et al. 1997a). Because this corresponds to a smaller minimum mass there is more signal, improving the signal-to-noise ratio. In all of the plots we show the clustering and shot-noise components which make up the power spectrum. In all cases the clustering signal dominates on large scales. The error bars are much smaller for high k-values because they represent clustering on small scales and there are many more small scale regions to sample within a given survey volume.

The OI(145μm) bad line for OI(63μm) and the NII(122μm) bad line for OIII(52μm) originate from very nearby redshifts. Thus, the cross correlation of these could produce a spurious signal. However, we find that for our $z = 5 - 6$ examples all of the galaxies emitting this spurious signal could be located with the CII(158μm) line and removed. For the $z = 7 - 8$ examples one may need to measure and subtract away some of the spurious signal as discussed above. This was not considered for Figure 2.2 and could slightly degrade the constraints on the cross power spectrum at these redshifts.

Figure 2.2.—: The cross power spectrum of the OI(63μm) and OIII(52μm) lines at redshifts of $z = 5 - 8$. Bright sources which can be individually detected have been removed. The dashed line is the clustering component, the dot-dashed line is the shot-noise power spectrum due to the discrete nature of galaxies and the solid line is their sum. The error bars show the root-mean-square error on the cross power spectrum for a 10^6 second observation with SPICA. We assume that the survey is comprised of 256 adjacent pointings on the sky and has a depth of $\Delta z = 0.1(1 + z)$. In the $z = 5 - 7$ panels we have assumed that reionization occurred at a much higher redshift. In the $z = 8$ panel we have assumed that reionization occurred instantaneously at $z = 6$; this increases the signal to noise because it reduces the minimum mass of galaxies. The errors have been determined by averaging the cross power spectrum in bins of width $\Delta k = k/5$.

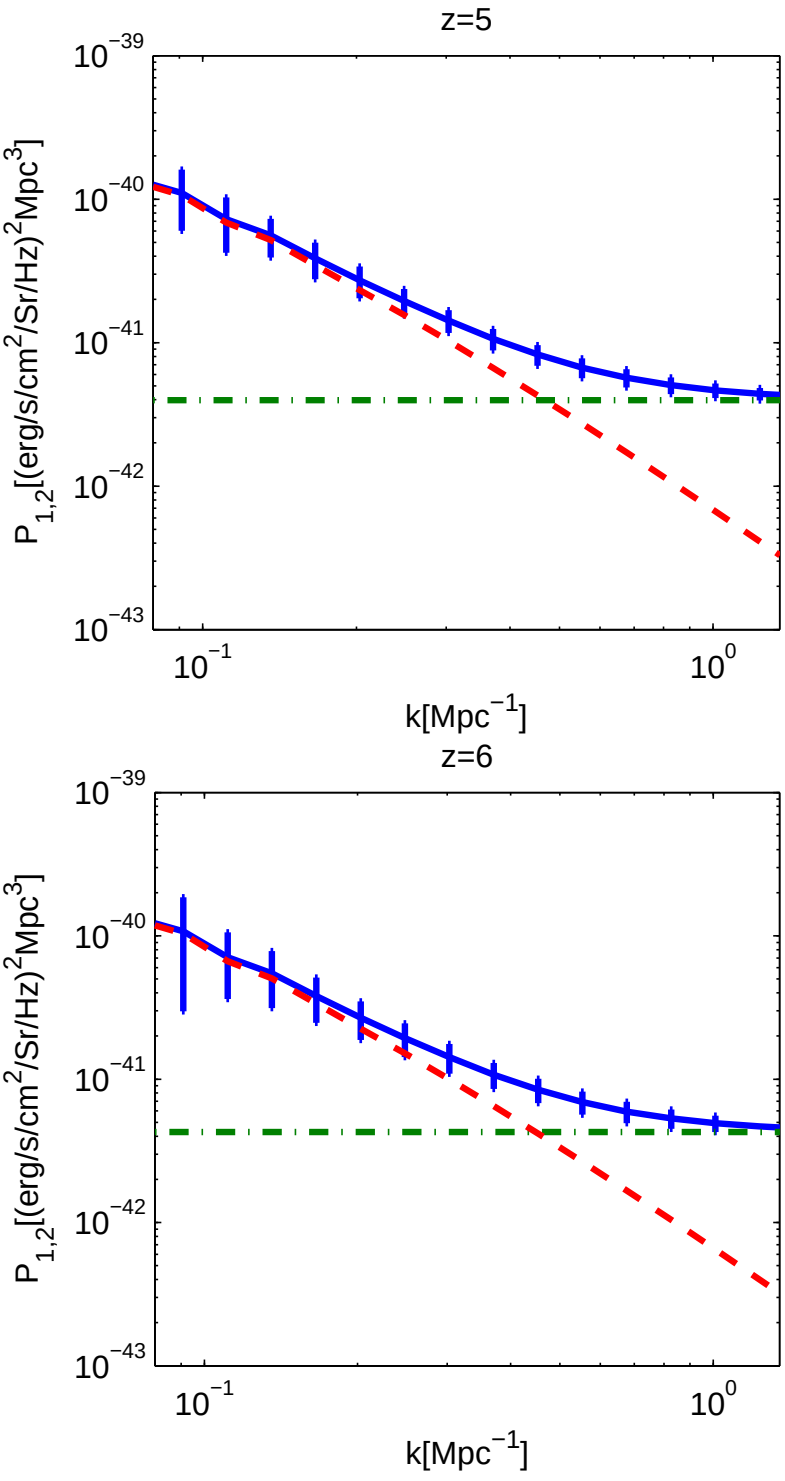

Figure 2.2.—: (Continued).

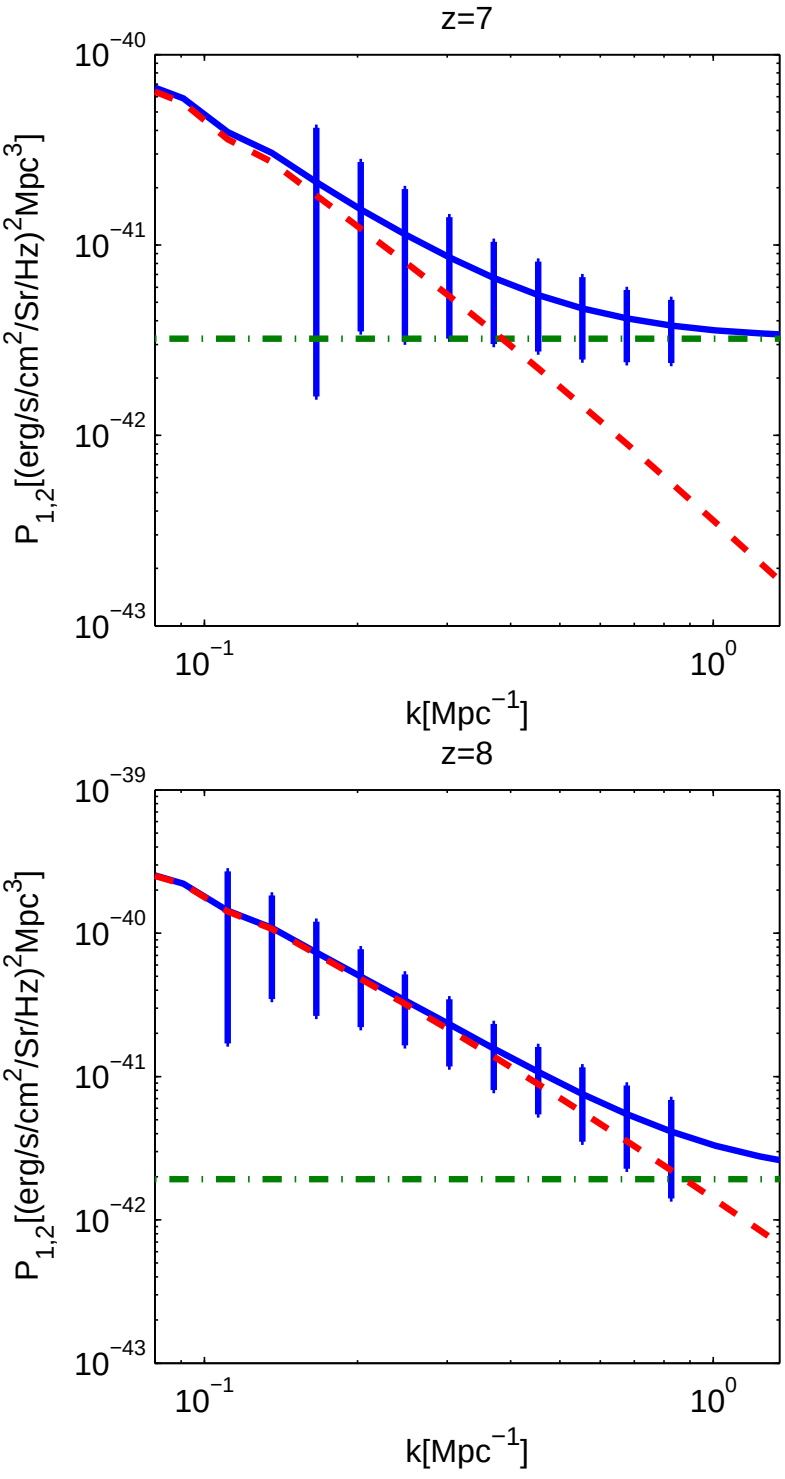

Figure 2.2.—: (Continued).

Figure 2.3 shows $M^2 \frac{dn}{dM}$ and $M^3 \frac{dn}{dM}$ versus M. The area under the first distribution is proportional to the contribution to the average signal from the corresponding halo mass range. Similarly, for the second function the area under the curve is proportional to the contribution to the shot-noise power spectrum. Fainter sources contribute more to the clustering signal because of their great numbers. By contrast, the shot-noise signal originates mainly from bright sources. If the brightest sources are removed, then the shot-noise signal should be substantially reduced while the clustering signal remains relatively unchanged. Owing to the hierarchical nature of structure formation in the universe more matter will be located in smaller halos at higher redshifts.

Figure 2.3.—: The mass distributions $M^2 \frac{dn}{dM}$ and $M^3 \frac{dn}{dM}$ versus M at various redshifts. The area under the first is proportional to the contribution to the average line signal (see Eq. (2.9)) from the corresponding mass range, while for the second it is proportional to the contribution to the shot-noise power spectrum (see Eq. (2.12)). We see that most of the average signal and thus the clustering component of the cross power spectrum comes from low mass halos.

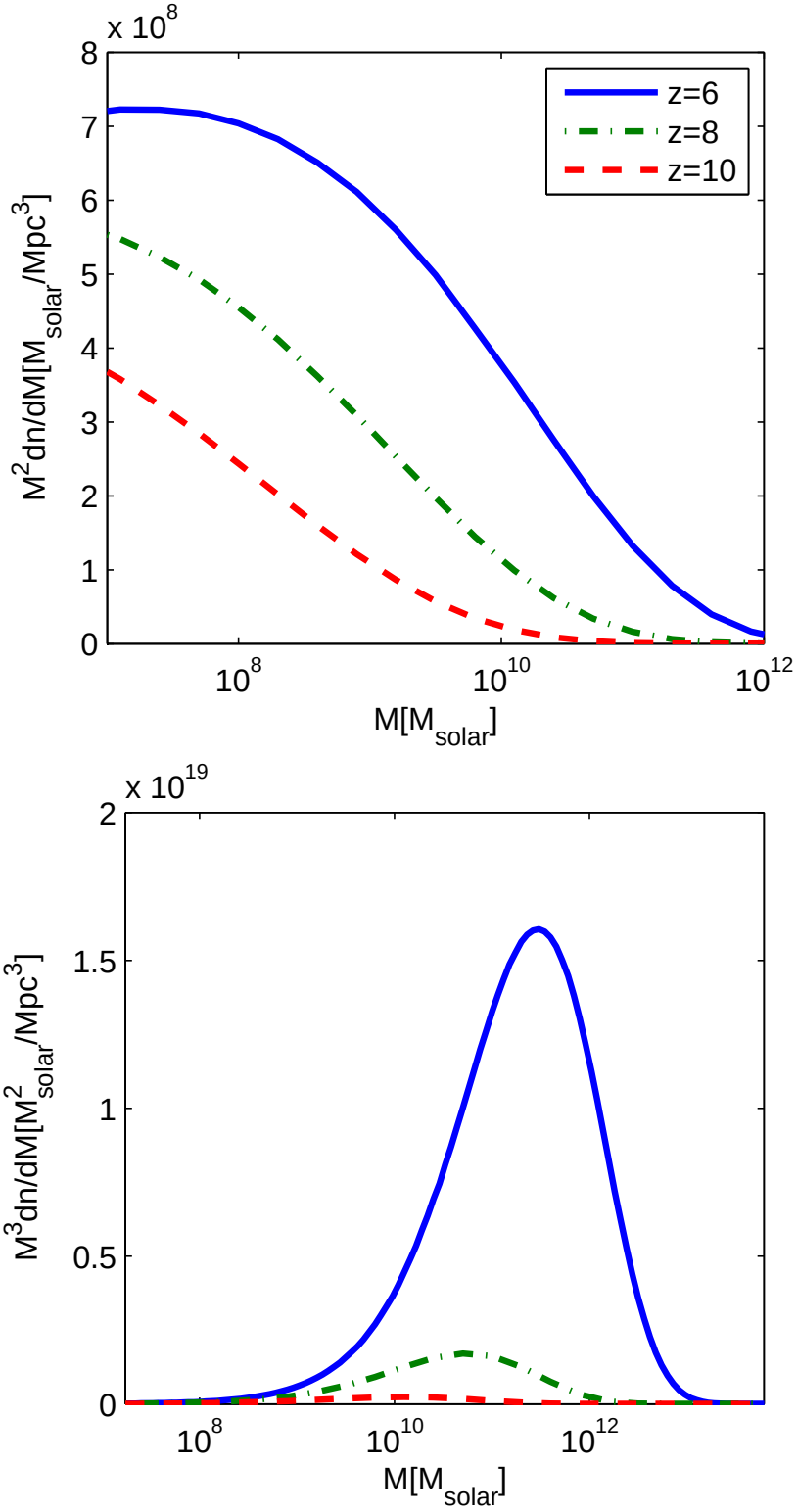

Figure 2.3.—: (Continued).

Figure 2.4 shows the fraction of the average OI(63 μm) signal which originates from lines that would be detected at less than 3σ significance for different values of the duty cycle. The average signal does not depend on the duty cycle because at lower values, the brightness of galaxies in our model goes up by the same factor that reduces the number of active galaxies. Thus, our technique is particularly effective if the duty cycle is high. This results in a higher number of fainter galaxies which would be harder to detect directly, but just as easy statistically using the cross power spectrum.

Figure 2.5 shows the average signal times the bias as a function of redshift for different reionization histories. We show one line assuming that reionization is sudden and that $M_{\rm min}$ changes instantaneously and a line which smooths the transition of $M_{\rm min}$ with an error function. For the smoothed case, the minimum mass of halos hosting galaxies is given by,

$$M_{\rm min}(z) = \left(M_1 - \frac{(M_1 - M_2)}{2}\left[1 + {\rm erf}(z - z_r)\right]\right)\left(\frac{10}{1+z}\right)^{3/2}, \qquad (2.31)$$

where $M_1 = 3 \cdot 10^9 M_\odot$, $M_2 = 10^8 M_\odot$, and the redshift of reionization $z_r = 10$. While these are not necessarily realistic reionization histories, they illustrate that the minimum mass of halos which host galaxies could be detected with the cross correlation technique. It may be difficult to observe the cross power spectrum at $z = 10$. If reionization occurs later it will be easier to study. If many different lines are used one may be able to probe higher redshifts than those shown in Figure 2.2.

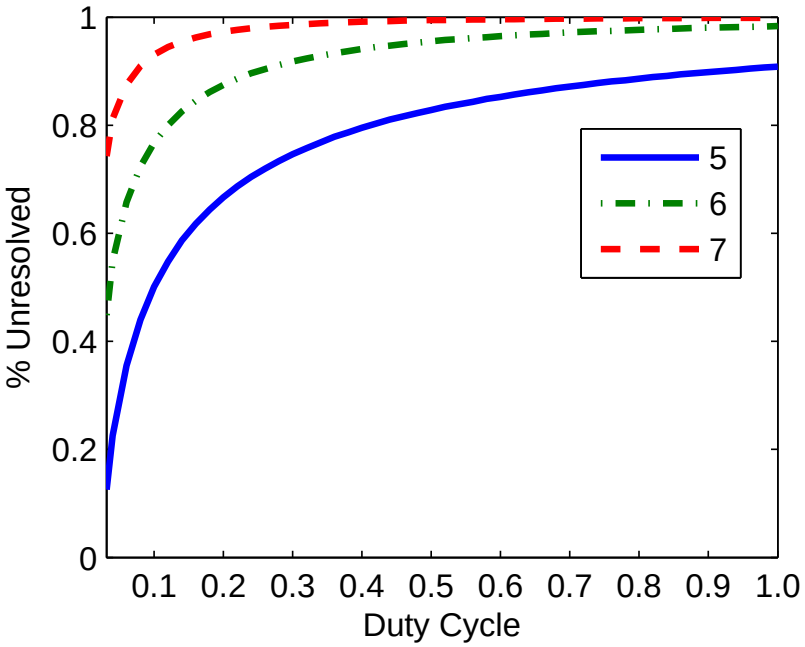

Figure 2.4.—: The percentage of the average OI(63 μm) line signal which originates from galaxies that are less than 3σ peaks in the noise versus duty cycle. We assume a 10^6s observation with 256 different pointings. As the duty cycle goes up there are more halos hosting fainter galaxies increasing the amount of signal which will come from galaxies which cannot be directly detected.

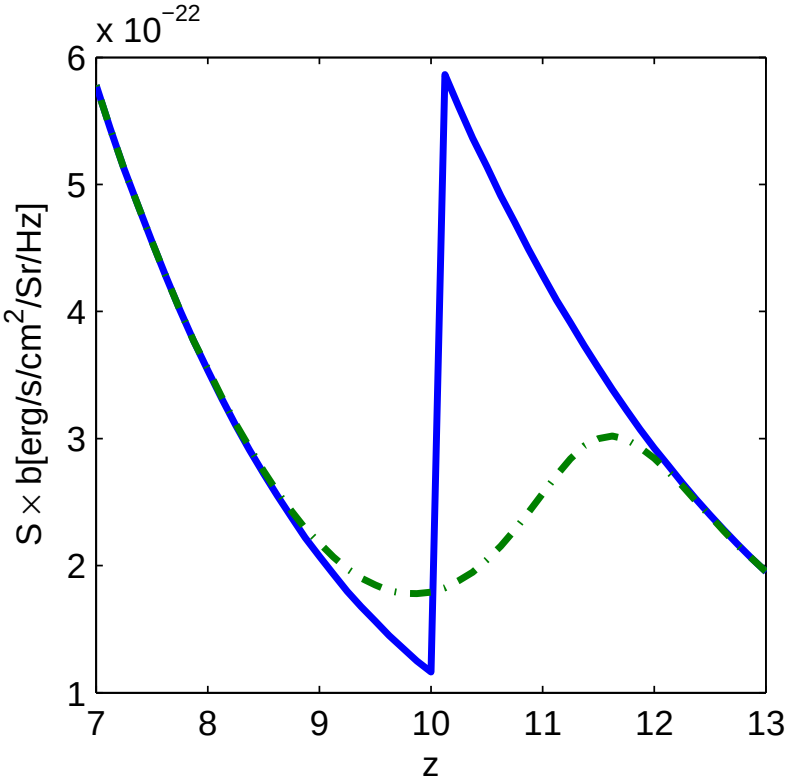

Figure 2.5.—: The average OI(63 μm) line signal times the bias as a function of redshift. For the solid curve we have assumed that reionization occurs instantaneously at $z = 10$ and that the minimum mass of galaxies changes from the requirement that hydrogen cooling is efficient to the Jean's mass after reionization. In the other curve, the change in minimum mass has been smoothed with an error function. While these may not be realistic reionization histories, this figure illustrates that one may probe the reionization history with the cross power spectrum. Though we have shown the cross power spectrum corresponding to reionization at $z = 10$, note that it may be difficult to observe this signal with SPICA.

2.4 Cross-correlating CO Lines with 21-cm Emission

2.4.1 Instruments

As another example, we consider cross correlating CO line emission measured with a large ground based telescope and 21-cm line emission from neutral hydrogen in galaxies measured with an interferometer optimized for frequencies corresponding to post-reionization redshifts. As discussed above, in order to measure fluctuations in line emission, one must first fit and subtract away the bright foreground signal. Because they will have completely different sources of foreground emission, cross correlating CO and 21-cm line emission could eliminate any residual foregrounds if they are present after this subtraction process.

The Cornell Caltech Atacama Telescope (CCAT) is a large sub-mm telescope to be built at high altitude in the Atacama region of northern Chile. It will be a 25 meter telescope with a 10 arcminute field of view. We consider a hypothetical instrument which takes spectra of 1000 adjacent diffraction limited beams simultaneously. We assume spectrometers with resolving power of $R = \nu/\Delta\nu = 1000$ and background limited sensitivity on CCAT. Specifically, we use the numbers listed in Figure 6 of Bradford et al. (2009).

For the 21cm experiment, we consider a hypothetical interferometer which is similar to the Murchison Widefield Array (MWA) (Bowman et al. 2009), but optimized to observe 21-cm emission at a redshift of z=3. We assume an array of 500 tiles each consisting of 16 dipoles with an effective area of $A_{\rm e} = 2.8{\rm m}^2$ per tile.

2.4.2 Results

To calculate the CO line signal we use the approach discussed in Section 2.3.2. As in the SPICA example, we assume a duty cycle of $\epsilon_{\rm duty} = 0.1$ and star formation efficiency of $f_* = 0.1$. After reionization 21-cm emission is expected to come from self-shielded neutral hydrogen in galaxies (Wyithe & Loeb 2009; Loeb & Wyithe 2008). After reionization, the difference between the average observed 21-cm brightness temperature from redshift z and the CMB temperature today is described by

$$\bar{T}_{\rm b} \approx 26 \bar{x}_{\rm H} \left(\frac{\Omega_{\rm b} h^2}{0.022} \right) \left(\frac{0.15}{\Omega_{\rm m} h^2} \frac{1+z}{10} \right)^{1/2} {\rm mK}, \tag{2.32}$$

where $\bar{x}_{\rm H}$ is the global mass-averaged neutral hydrogen fraction. Observations have shown that out to $z \approx 4$ the cosmological density parameter of HI is $\Omega_{\rm HI} \approx 10^{-3}$ (Prochaska et al. 2005). This corresponds to a mass-averaged neutral fraction of a few percent. For our calculations we assume a value of $\bar{x}_{\rm H} = 0.02$. In the context of the formalism discussed above, $\bar{T}_{\rm b}$ is the average line signal after converting to units of (ergs/s/cm^2/Hz/Sr) with the Rayleigh-Jeans Law. With this quantity we can also calculate the shot-noise power spectrum as we did with Eq. (2.12). For this calculation, we assume that the 21-cm flux originating from dark matter halos above $M_{\rm min}$ is proportional to their mass. The shot-noise power spectrum is lower than our previous example because we have emission from all halos above the minimum mass as opposed to a smaller fraction set by the duty cycle.

The noise power spectrum is given by

$$P_{\rm noise}(k \sin\theta) = D_{\rm A}^2 \tilde{y} \left(\frac{\lambda^2 T_{\rm sys}}{A_{\rm e}} \right)^2 \frac{1}{t_0 n(k \sin\theta)}, \tag{2.33}$$

where $\lambda = 21{\rm cm} \times (1+z)$ is the observed wavelength, $T_{\rm sys}$ is the system temperature of

the interferometer, $A_{\rm e}$ is the effective area of each tile, t_0 is the total observing time, and $n(k\sin\theta)$ is the number density of baselines where $k = |\vec{k}|$ and θ is the angle between $\vec{k}$ and the line of sight. The baseline density $n(k\sin\theta)$ depends on the geometrical configuration of the 500 antenna tiles. We have assumed a distribution of tiles with constant density within the innermost 8.9m and which falls off as r^{-2} out to 330m. We assume that $T_{\rm sys} = T_{\rm sky} + T_{\rm inst}$ where the sky temperature $T_{\rm sky} = 260\,[(1+z)/9.5]^{2.55}$ (Rogers & Bowman 2008), and that the instrumental temperature is $T_{\rm inst} = 100$K. For a derivation of the expression which gives the noise power spectrum see Ref. (McQuinn et al. 2006a).

In Figure 2.6 we plot the cross power spectrum of CO(8-7) and 21-cm line emission at $z = 3$. We show the error bars corresponding to an observation lasting 10^6 seconds for each instrument and covering the field of view of one primary beam, $\Omega = \lambda^2/A_{\rm e} = 0.25$ Sr, of our MWA-like interferometer.

2.5 Discussion and Conclusions

In this paper, we have developed a formalism for measuring the cross power spectrum of line emission from galaxies. Cross correlating the flux fluctuations in different lines from the same galaxies removes the contaminating signal from other "bad lines." We demonstrated that it is possible to statistically measure the line fluctuation signal from undetected galaxies at some target redshift. The distinct difference and advantage of this technique compared to traditional galaxy surveys is that the signal originates from *all* sources of line emission rather than just the high signal-to-noise peaks in the data. In this way it is possible to study large populations of faint galaxies in a reasonable amount

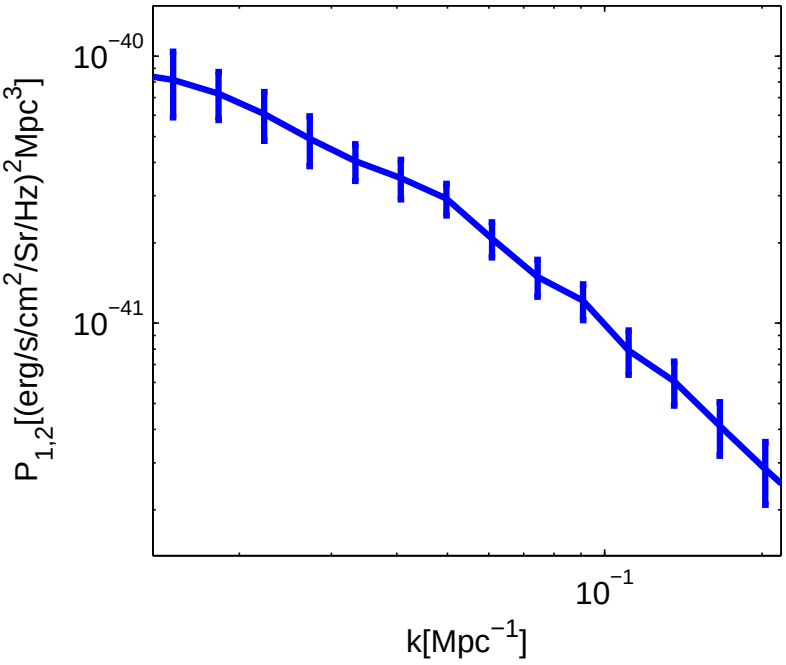

Figure 2.6.—: The cross power spectrum of CO(8-7) and 21-cm galaxy line emission at $z = 3$. The shot-noise power spectrum is negligible for the values of k shown. The error bars show the root-mean-square error on the cross power spectrum for a 10^6 second observation with CCAT and a separate 10^6 second observation with our hypothetical 21cm interferometer. We assume a survey depth of $\Delta z = 0.1(1 + z)$.

of observing time. Even though individual galaxies will be difficult to detect, their large numbers contribute significantly to the total signal. The relative contributions of different mass ranges to the clustering signal can be seen in Figure 2.3. At high redshifts, the faintest galaxies produce the most signal per logarithmic mass interval.

The cross power spectrum of line emission measures the product of the cosmic matter power spectrum, the average signal coming from a pair of lines and the luminosity weighted bias of the source galaxies. For the standard set of cosmological parameters, one knows the theoretical value of the matter power spectrum. The cross power spectrum then gives the product of the two average line signals with the bias squared. The shot-noise component of the cross power spectrum depends on the duty cycle while the clustering component does not. This allows an estimation of the duty cycle by comparing the cross power spectrum at low k-values where clustering dominates to high k values where the shot-noise component dominates.

We demonstrated this technique by showing that atomic and ionic fine structure lines from galaxies could be cross correlated using the proposed SPICA mission. We have found that for OI($63\mu m$) and OIII($52\mu m$) and an observation lasting a total of 10^6 seconds, the cross power spectrum of sources too faint to be directly detected can be measured accurately out to $z \approx 8$. This is important because depending on the duty cycle, most of the line emission signal originates from galaxies which cannot be detected otherwise.

The cross power spectrum at these redshifts allows one to measure the total emission in O and N lines from a large sample of faint galaxies as a function of redshift. This information would constrain the evolution of galaxy properties such as metallicity and

star formation rate. It also constrains the bias and duty cycles of the source galaxies. Finally, the value of the average signal is sensitive to the minimum mass of galaxies, and so the evolution in the average line signal could constrain the reionization history.

We also consider an example where we cross correlate the CO and 21-cm line emission from galaxies measured with CCAT and an interferometer similar in scale to MWA, but optimized for post-reionization redshifts. As in the SPICA example, this would yield important information about the evolution of CO emission from galaxies over cosmic time. Because we expect the foregrounds in CO and 21-cm observations to be uncorrelated, cross correlation could eliminate spurious residual foreground emission if any remained after the removal process. Of course, one could also cross correlate different lines, such as the various CO lines and CII(158μm), with an instrument like CCAT alone.

In our calculations we have assumed that the foregrounds are smooth in frequency and can be removed perfectly, leaving only the fluctuations due to line emission and detector noise. If the foregrounds vary rapidly as a function of angle on the sky it may only be possible to measure k-modes along the line of sight.

The cross correlation technique is general and may be used for many different lines (such as those listed in Table 2.1). It will be most useful for instruments which have a large field of view, but cannot detect individual faint sources effectively. Additional angular or spectral resolution will provide access to fluctuations on smaller scales, but will not improve the accuracy of the cross power spectrum on large scales.

Acknowledgments

We thank Mark Dijkstra and Jonathan Pritchard for useful comments. We also thank the referee, Asantha Cooray, for helpful suggestions. This work was supported in part by NSF grant AST-0907890 and NASA grants NNX08AL43G and NNA09DB30A.

2.6 Appendix: Error on Cross Power Spectrum

The error on an estimate for the cross power spectrum at a particular wave-vector is given by,

$$\delta P_{1,2}^2 = \langle \hat{P}_{1,2}^2 \rangle - \langle \hat{P}_{1,2} \rangle^2 = \left\langle \frac{V^2}{4} (f_{\vec{k}}^{(1)} f_{\vec{k}}^{(2)*} + f_{\vec{k}}^{(1)*} f_{\vec{k}}^{(2)})^2 \right\rangle - P_{1,2}^2, \tag{2.34}$$

where V is the survey volume and $f_{\vec{k}}$ is the Fourier amplitude defined in Eq. (2.13) with superscripts denoting the target lines being cross correlated. For each target line we break up $f_{\vec{k}}$ into terms corresponding to those in Eq. (2.1). Plugging Eq. (2.14) into Eq. (2.34) and expanding we are left with the sum of many products of four Fourier modes, many of which are not correlated and vanish. We are only left with products of Fourier amplitudes that are correlated: detector noise with itself, the bad lines' fluctuations with themselves and the target lines' fluctuations with themselves and one another. We then only need to calculate the average value of these various products.

The terms involving detector noise are easily calculated by changing the integral in Eq. (2.13) into a sum. It follows that,

$$\langle V f_{\vec{k}}^{n1} f_{\vec{k}}^{n1*} \rangle = P_{\rm noise} = \sigma_{\rm n}^2 V_{\rm pix}, \tag{2.35}$$

where $\sigma_{\rm n}^2$ is the variance of the noise in units of ergs/s/cm^2/Hz/Sr in a single pixel and

$V_{\rm pix}$ is the survey volume corresponding to each pixel.

The Fourier amplitudes corresponding to the bad lines are given by

$$f_{\vec{k}}^{B1} = \bar{B}_1 \bar{b}_1 \int d^3\vec{r}\delta(\vec{r_o} + d_1\hat{\mathbf{k}} + \vec{r'}_1)W(\vec{r})e^{i\vec{k}\cdot\vec{r}}, \tag{2.36}$$

where $\vec{r_1'} = c_{x1}x\hat{\mathbf{i}} + c_{y1}y\hat{\mathbf{j}} + c_{z1}z\hat{\mathbf{k}}$. We change integration variables from (x, y, z) to $(x_1' = c_{x1}x, y_1' = c_{y1}y, z_1' = c_{z1}z)$, and proceed as we did in Eqs. (2.15)-(2.19). We find,

$$\langle V f_{\vec{k}}^{B1} f_{\vec{k}}^{B1*}\rangle = \bar{B}_1^2\bar{b}_1^2\frac{P(\vec{k_1'}, z_1)}{(c_{x1}c_{y1}c_{z1})}, \tag{2.37}$$

where $\vec{k_1'} = \frac{k_x}{c_{x1}}\hat{\mathbf{i}} + \frac{k_y}{c_{y1}}\hat{\mathbf{j}} + \frac{k_z}{c_{z1}}\hat{\mathbf{k}}$. The $c's$ in these equations reflect the stretching and squeezing of the data cube at the redshifts of the spurious lines due to the redshift dependence of the angular diameter distance and frequency per comoving interval as described above.

It is also necessary to calculate terms like,

$$\begin{aligned} V^2\langle f_{\vec{k}}^{S1*} f_{\vec{k}}^{S1*} f_{\vec{k}}^{S2} f_{\vec{k}}^{S2}\rangle = \\ V^2\frac{1}{(2\pi)^{12}}\int\int\int\int d^3\vec{k_1}d^3\vec{k_2}d^3\vec{k_3}d^3\vec{k_4}W(\vec{k_1}-\vec{k})W(\vec{k_2}-\vec{k})^*W(\vec{k_3}-\vec{k})^*W(\vec{k_4}-\vec{k}) \\ \times \bar{S}_1^2\bar{S}_2^2\bar{b}^4\langle\delta(\vec{k_1})\delta(\vec{k_2})^*\delta(\vec{k_3})^*\delta(\vec{k_4})\rangle e^{-i(\vec{k_1}-\vec{k_2}-\vec{k_3}+\vec{k_4})\cdot\vec{r_o}} = 2\bar{S}_1^2\bar{S}_2^2\bar{b}^4P(\vec{k}), \end{aligned} \tag{2.38}$$

where to calculate this integral we have used Wick's theorem $\langle\delta_1\delta_2\delta_3\delta_4\rangle = \langle\delta_1\delta_2\rangle\langle\delta_3\delta_4\rangle + \langle\delta_1\delta_3\rangle\langle\delta_2\delta_4\rangle + \langle\delta_1\delta_4\rangle\langle\delta_2\delta_3\rangle$. We also used Eq. (2.18) and the fact that for a large survey $|W(\vec{k'}-\vec{k})|^2 \approx (2\pi)^3\delta^D(\vec{k'}-\vec{k})/V$.

Putting all of this together we find,

$$\delta P_{1,2}^2 = \frac{1}{2}(P_{1,2}^2 + P_{1\rm total}P_{2\rm total}), \tag{2.39}$$

where $P_{1\text{total}}$ is the total power spectrum corresponding to the first line being cross correlated,

$$P_{1\text{total}} = \bar{S}_1^2 \bar{b}^2 P(\vec{k}, z_{\text{target}}) + P_{\text{noise1}} + \bar{B}_1^2 \bar{b}_1^2 \frac{P(\vec{k_1'}, z_1)}{(c_{x1} c_{y1} c_{z1})} + \bar{B}_2^2 \bar{b}_2^2 \frac{P(\vec{k_2'}, z_2)}{(c_{x2} c_{y2} c_{z2})} \ldots \tag{2.40}$$

The equation corresponding to the second line being cross correlated is exactly the same, but of course contains the noise at a different frequency and will have bad lines at different redshifts. There will also be a shot-noise power spectrum for each clustering spectrum included above, which was not written to avoid a cumbersome equation.

Chapter 3

Demonstrating the Feasibility of Line Intensity Mapping Using Mock Data of Galaxy Clustering from Simulations

E. Visbal, H. Trac, & A. Loeb *Journal of Cosmology and Astroparticle Physics*, Issue 8, ID 010, 2011

Abstract

Visbal & Loeb (2010) have shown that it is possible to measure the clustering of galaxies by cross correlating the cumulative emission from two different spectral lines which

originate at the same redshift. Through this cross correlation, one can study galaxies which are too faint to be individually resolved. This technique, known as intensity mapping, is a promising probe of the global properties of high redshift galaxies. Here, we test the feasibility of such measurements with synthetic data generated from cosmological dark matter simulations. We use a simple prescription for associating galaxies with dark matter halos and create a realization of emitted radiation as a function of angular position and wavelength over a patch of the sky. This is then used to create synthetic data for two different hypothetical instruments, one aboard the Space Infrared Telescope for Cosmology and Astrophysics (SPICA) and another consisting of a pair of ground based radio telescopes designed to measure the CO(1-0) and CO(2-1) emission lines. We find that the line cross power spectrum can be measured accurately from the synthetic data with errors consistent with the analytical prediction of Visbal & Loeb (2010). Removal of astronomical backgrounds and masking bright line emission from foreground contaminating galaxies do not prevent accurate cross power spectrum measurements.

3.1 Introduction

Recently, Visbal & Loeb (2010) suggested a new technique for statistically observing the clustering of faint galaxies through intensity mapping of multiple atomic and molecular lines (see also Gong et al. 2011; Carilli 2011; Lidz et al. 2011). This method can probe galaxies which are too faint to be seen individually, but which contribute significantly to the cumulative emission due to their large numbers.

Atoms and molecules in the interstellar medium of galaxies produce line emission at particular rest frame wavelengths (Binney & Merrifield 1998). For galaxies at

cosmological distances, these wavelengths are redshifted by a factor of $(1 + z)$ due to cosmic expansion. Thus, for emission in a particular spectral line, the observed angular position and the observed wavelength correspond to a 3D spatial location. With observational data which includes both spectral and spatial information, one can then measure the three dimensional clustering of galaxies.

Before line emission can be associated with a particular location in space, one must separate it from spectrally extended emission. Galactic continuum emission and spectrally smooth astrophysical foregrounds and backgrounds (e.g., the Cosmic Microwave Background or galactic dust emission) can be removed by fitting smooth functions of frequency to data and subtracting them away; this has been discussed extensively in the context of cosmological 21cm observations (Petrovic & Oh 2011a; Morales 2005; Wang et al. 2006; McQuinn et al. 2006a; Liu et al. 2009; Liu & Tegmark 2011). After background emission is removed one still needs to avoid possible confusion with other emission lines. For multiple lines of different rest frame wavelengths the intensity at a particular observed wavelength corresponds to emission from multiple redshifts, one for each emission line. With both spatial and spectral information, the total emission over a small range in observed wavelength corresponds to a superposition of the 3D distribution of galaxies at different redshifts.

Fortunately, it is possible to statistically isolate the fluctuations from a particular redshift by cross correlating the emission in two different lines (Visbal & Loeb 2010). If one compares the fluctuations at two different wavelengths, which correspond to the same redshift for two different emission lines, the fluctuations will be strongly correlated. However, the signal from any other lines arises from galaxies at different redshifts which are very far apart and thus will have much weaker correlation (see Figure 3.1). In this

way, one can measure either the two-point correlation function or power spectrum of galaxies at some target redshift weighted by the total emission in the spectral lines being cross correlated.

We emphasize that one can measure the line cross power spectrum from galaxies which are too faint to be seen individually over detector noise. Hence, a measurement of the line cross power spectrum can provide information about the total line emission from all of the galaxies which are too faint to be directly detected. One possible application of this technique would be to measure the evolution of line emission over cosmic time to better understand galaxy evolution and the sources that reionized the Universe. Changes in the minimum mass of galaxies due to photoionization heating of the intergalactic medium during reionization could also potentially be measured (Visbal & Loeb 2010).

Here we use cosmological simulations to test the feasibility of measuring the galaxy line cross power spectrum. We create synthetic data sets for two hypothetical instruments, one on the Space Infrared Telescope for Cosmology an Astrophysics (SPICA) and the other consisting of a pair of ground based radio telescopes optimized to measure CO(1-0) and CO(2-1) emission from high redshifts. We test how well the cross power spectrum can be measured and find agreement with the analytical expectation derived in Visbal & Loeb (2010). However there are some additional complications. Small k-modes along the line of sight which are contaminated during the foreground removal process must be discarded, increasing the statistical uncertainty on large spatial scales. Additionally, when masking out contaminating emission lines from bright foreground galaxies one must be careful not to introduce a spurious correlation between the data sets being cross correlated.

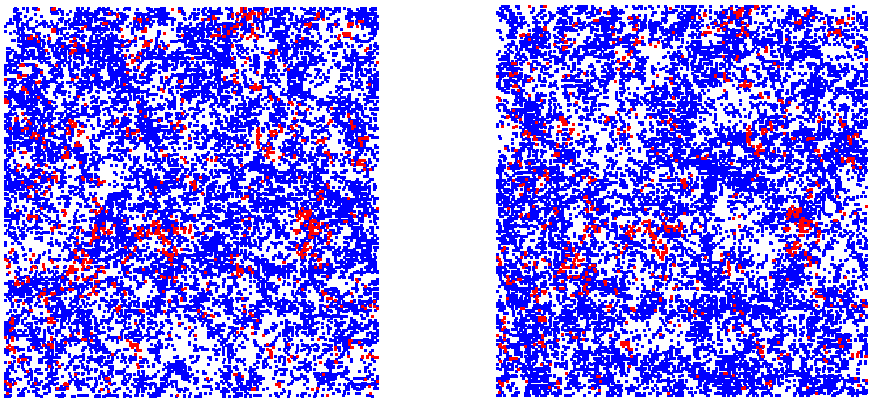

Figure 3.1.—: A slice from our simulated realization of line emission from galaxies at an observed wavelength of 441μm (left) and 364μm (right). The slice is in the plane of the sky and spans 250×250 comoving Mpc^2 with a depth of $\Delta\nu/\nu = 0.001$. The colored squares indicate pixels in our SPICA example (presented below) which have line emission greater than 200Jy/Sr for the left panel and 250Jy/Sr for the right panel. The emission from OI(63μm) and OIII(52μm) is shown in red on the left and right panels, respectively, originating from the same galaxies at $z = 6$. All of the other lines in Table 3.1 are included and plotted in blue. Cross correlating data at these two observed wavelengths would reveal the emission in OI and OIII from $z = 6$ with the other emission lines being essentially uncorrelated.

The paper is organized as follows. In Section 3.2 we describe the methods used in this paper. This includes a brief review of the galaxy line cross power spectrum, a description of the synthetic data sets, the details of the simulations, and a discussion of the steps involved in measuring the cross power spectrum. In Sections 3.3 and 3.4 we present our results for the SPICA example and the CO(1-0) and CO(2-1) telescopes, respectively. Finally, we discuss and summarize our conclusions in Section 3.5. Throughout, we assume a ΛCDM cosmology with $\Omega_\Lambda = 0.73$, $\Omega_m = 0.27$, $\Omega_b = 0.045$, $h = 0.7$, $n_\mathrm{s} = 0.96$ and $\sigma_8 = 0.8$, (Komatsu et al. 2011).

3.2 Method

3.2.1 Galaxy Line Cross Power Spectrum

First, we briefly review the galaxy line cross power spectrum. For a more complete discussion, see Visbal & Loeb (2010). We assume that emission is measured both as a function of angle on the sky and observed wavelength. If one fits a smooth function of wavelength along each direction on the sky and subtracts it from the data, one obtains the fluctuations from the average signal as a function of angle and wavelength: $\Delta S(\theta_1, \theta_2, \nu) = S(\theta_1, \theta_2, \nu) - \bar{S}$. There is a one to one correspondence between angular position and wavelength and spatial position for emission in a particular line. For convenience we use comoving coordinates at the location of the target galaxies instead of angle and wavelength. The fluctuations at a particular location results from a number of different sources,

$$\Delta S_1 = \Delta S_{\mathrm{line1}} + \Delta S_{\mathrm{noise}} + \Delta S_{\mathrm{badline1}} + \Delta S_{\mathrm{badline2}} + \dots \tag{3.1}$$

which include contributions from the target galaxies we wish to cross correlate, detector noise, and emission in different lines from galaxies at different redshifts which we refer to as "bad line" emission. One can cross correlate the fluctuations in two different lines from the same galaxies. We define the line cross correlation function as,

$$\xi_{1,2}(\vec{r}) = \langle \Delta S_1(\vec{r}_o, \vec{x}) \Delta S_2(\vec{r}_o, \vec{r} + \vec{x}) \rangle, \tag{3.2}$$

where subscripts denote different lines being cross correlated. The center of the survey volume is denoted by $\vec{r}_o$, $\vec{x}$ is the distance from the center in the first set of fluctuations, and $\vec{r} + \vec{x}$ is the distance from the center in the second set of fluctuations.

Because the noise fluctuations in the two different data sets are uncorrelated and galaxies seen in different bad lines will have very large separations and thus be essentially uncorrelated we are only left with contributions from the target galaxies. On large scales we can make the assumption that line fluctuations due to galaxy clustering are given by $\Delta S_{\rm line1} = \bar{S}_1 \bar{b} \delta(\vec{r})$, where $\bar{S}_1$ is the average target line signal, $\bar{b}$ is the luminosity weighted average galaxy bias, and $\delta(\vec{r})$ is the cosmological over-density at a location $\vec{r}$. It follows that,

$$\xi_{1,2}(\vec{r}) = \langle \Delta S_{\rm line1}(\vec{r}_o, \vec{x}) \Delta S_{\rm line2}(\vec{r}_o, \vec{r} + \vec{x}) \rangle = \bar{S}_1 \bar{S}_2 \bar{b}^2 \langle \delta(\vec{x}) \delta(\vec{r} + \vec{x}) \rangle = \bar{S}_1 \bar{S}_2 \bar{b}^2 \xi(\vec{r}), \tag{3.3}$$

where $\xi(\vec{r})$ is the cosmological matter correlation function and the subscript numbers denote the different lines being cross correlated.

The line cross power spectrum is then defined as the Fourier transform,

$$P_{1,2}(\vec{k}) = \int d^3\vec{r} \xi_{1,2}(\vec{r}) e^{i\vec{k}\cdot\vec{r}} = \bar{S}_1 \bar{S}_2 \bar{b}^2 P(\vec{k}) + P_{\rm shot}, \tag{3.4}$$

where $P_{\rm shot}$ is the shot-noise power spectrum due to the discrete nature of galaxies.

An unbiased estimator for the cross power spectrum is given by the product of the Fourier transforms of the data sets,

$$\hat{P}_{1,2} = \frac{V}{2}(f_{\vec{k}}^{(1)} f_{\vec{k}}^{(2)*} + f_{\vec{k}}^{(1)*} f_{\vec{k}}^{(2)}), \tag{3.5}$$

where V is the volume of the survey and the superscripts denote the different lines being cross correlated. The Fourier amplitude is given by,

$$f_{\vec{k}} = \int d^3\vec{r} \Delta S(\vec{r_o}, \vec{r}) W(\vec{r}) e^{i\vec{k}\cdot\vec{r}}. \tag{3.6}$$

Here $W(\vec{r})$ is a window function that is constant over the survey volume and zero at all other locations. It is normalized such that, $\int W(\vec{r}) d^3\vec{r} = 1$.

The root mean square (RMS) error in a measurement of the cross power spectrum at one particular k-value is given by Visbal & Loeb (2010),

$$\delta P_{1,2}^2 = \frac{1}{2}(P_{1,2}^2 + P_{1\text{total}} P_{2\text{total}}), \tag{3.7}$$

where $P_{1\text{total}}$ and $P_{2\text{total}}$ are the total power spectrum corresponding to the first line and second line being cross correlated. Each of these includes a term for the power spectrum for each of the bad lines, the target line, and detector noise (see Appendix A of Visbal & Loeb (2010)). When averaging nearby values of the power spectrum this error goes down by a factor of $\sqrt{N_{\text{modes}}}$, where N_{modes} is the number of statistically independent k-values at which the power spectrum is measured.

3.2.2 Synthetic Data Set

In order to test the feasibility of measuring the line cross power spectrum we create synthetic data sets for instruments measuring both spatial and spectral information.

Our goal is to produce a realization of the light from all galaxies as a function of angular position and observed wavelength on a patch of the sky. We create these data with a cosmological dark matter simulation (described in detail below). From the simulation we construct a light cone which has the distribution of dark matter halos which would be observed today in the volume corresponding to an angular patch on the sky out to a redshift of $z = 10$.

A simple prescription is used to associate galaxies with the dark matter halos from our simulation. We assign each galaxy a spectrum and assume that its intensity scales with star formation rate (SFR). The SFR versus halo mass relation is determined by matching comoving density with observed UV luminosity functions (Reddy & Steidel 2009; Arnouts et al. 2005; Oesch et al. 2010; Bouwens et al. 2007, 2011b).

We assume that galaxies are found in dark matter halos above a minimum mass, $M_{\rm min}$. After reionization $M_{\rm min}$ represents the threshold for assembling heated gas out of the photo-ionized intergalactic medium, corresponding to a minimum virial temperature of $\approx 10^5$K (Wyithe & Loeb 2006). We assume that reionization was completed by a redshift of $z \approx 10$. In all of the examples presented below, $M_{\rm min}$ is set to correspond to this post-reionization requirement.

The larger dark matter halos in our simulation may host multiple galaxies. To incorporate this effect in our synthetic data we have used a simple prescription for the halo occupation distribution. Following Kravtsov et al. (2004) for the distribution of dark matter sub-halos, we consider two different types of galaxies: central and satellite. We assume that the distribution of central galaxies is a step function: above $M_{\rm min}$ we assume each halo has one galaxy at its center. We then assume that there are a number

of satellite galaxies given by a Poisson distribution with a mean of $N_{\rm sat} = (M/M_1)^{\beta}$, here $\beta = 1$, and $M_1 = 30M_{\rm min}$ at $z = 0 - 0.5$; $M_1 = 20M_{\rm min}$ at $z = 0.5 - 2$; and $M_1 = 10M_{\rm min}$ at $z > 2$. We distribute these galaxies randomly, but weighted by an NFW profile, throughout the larger host dark matter halo. We treat the central and satellite galaxies as independent in assigning star formation rates to them as explained below. We associate half of the total halo mass to the central galaxy halos and split the remainder of the mass equally to all of the satellite galaxy halos.

After relating galaxies to dark matter halos in the simulation we produce a spectrum for each galaxy. For the continuum, we take the measured spectral energy distribution of M82 and scale it with the SFR (Silva et al. 1998). The results are insensitive to the particular choice of galaxy continuum, as it is removed in the fitting and subtraction stage of the data analysis, as discussed below.

In order to estimate the amplitude of line emission fluctuations we assume a linear relationship between line luminosity, L, and star formation rate, $\dot{M}_*$, $L = \dot{M}_* \times R$, where R is the ratio between SFR and line luminosity for a particular line. This is similar to existing relations in different bands (see Kennicutt 1998) and was used in the past to estimate the strength of the galactic lines we consider (Righi et al. 2008). The values for relevant lines are shown in Table 3.1. For the first 7 lines, we use the same ratios, R, as in Righi et al. (2008) which were calculated by taking the geometric average of the ratios from an observational sample of lower redshift galaxies (Malhotra et al. 2001). The other lines have been calibrated based on the galaxy M82 (Panuzzo et al. 2010b). We assign a width to the lines based on the circular virial velocity of the dark matter halos, but the results are mostly insensitive to this choice for the spectral resolutions we consider in our examples. This is because the majority of the signal comes from lines which are

spectrally unresolved.

Table 3.1

Species	Emission Wavelength[μm]	R[$L_\odot/(M_\odot/\mathrm{yr})$]
CII	158	6.0×10^6
OI	145	3.3×10^5
NII	122	7.9×10^5
OIII	88	2.3×10^6
OI	63	3.8×10^6
NIII	57	2.4×10^6
OIII	52	3.0×10^6
^{12}CO(1-0)	2610	3.7×10^3
^{12}CO(2-1)	1300	2.8×10^4
^{12}CO(3-2)	866	7.0×10^4
^{12}CO(4-3)	651	9.7×10^4
^{12}CO(5-4)	521	9.6×10^4
^{12}CO(6-5)	434	9.5×10^4
^{12}CO(7-6)	372	8.9×10^4
^{12}CO(8-7)	325	7.7×10^4
^{12}CO(9-8)	289	6.9×10^4
^{12}CO(10-9)	260	5.3×10^4
^{12}CO(11-10)	237	3.8×10^4
^{12}CO(12-11)	217	2.6×10^4
^{12}CO(13-12)	200	1.4×10^4

Continued on Next Page...

Table 3.1 – Continued

Species	Emission Wavelength[μm]	R[$L_\odot/(M_\odot/\mathrm{yr})$]
CI	610	1.4×10^4
CI	371	4.8×10^4
NII	205	2.5×10^5
^{13}CO(5-4)	544	3900
^{13}CO(7-6)	389	3200
^{13}CO(8-7)	340	2700
HCN(6-5)	564	2100

Table 3.1:: Ratio between line luminosity, L, and star formation rate, $\dot{M}_*$, for various lines. For the first 7 lines this ratio is measured from a sample of low redshift galaxies. The other lines have been calibrated based on the galaxy M82.

For the results presented below we have made the simplification that all galaxies have the same R value for each emission line. Even if there is random scatter in the R values in each galaxy, the line cross power spectrum will remain unchanged. This scatter will behave essentially like detector noise with intensity that is non-uniform across the data cube.

We use observed UV luminosity functions (Reddy & Steidel 2009; Arnouts et al. 2005; Oesch et al. 2010; Bouwens et al. 2007, 2011b) of galaxies to calibrate the SFR assigned to dark matter halos with an abundance matching technique. Given the

observed luminosity functions, we determine the number density of galaxies as a function of SFR through the relation,

$$L_{\rm UV} = L_\lambda \left(\frac{\dot{M}_*}{M_\odot {\rm yr}^{-1}} \right) {\rm ergs/s/Hz}, \tag{3.8}$$

where L_λ is given by $L_\lambda = 8 \times 10^{27}$ at a rest frame wavelength of $\lambda = 1500$Å. This assumes a Salpeter initial mass function from $0.1 - 125 M_\odot$ and a constant $\dot{M}_* \gtrsim 100$Myr. The relationship between halo mass, M_i, and SFR $\dot{M}_{*i}$ at some particular mass, is found from the relation $n_h(> M_i) = n_g(> \dot{M}_{*i})$. Here $n_h(> M)$ is the number density of dark matter halos above mass M in our simulation and $n_g(> \dot{M}_*)$ is the number density of galaxies implied by the UV luminosity function above the SFR value, $\dot{M}_*$. This procedure is carried out in a number of different redshift bins which cover our entire light cone. As a simple correction for attenuation due to dust we increase the SFR of all halos in each redshift bin by a factor which sets the global SFR equal to that given in the blue solid curve in Figure 10 of Oesch et al. (2010). In the highest redshift bin we do not apply any dust correction. The particular parameters used for the abundance matching procedure are listed in Table 3.2.

Finally, we add detector noise and bright astronomical foreground and background emission. For the examples below we include both the CMB and emission from dust in our galaxy. The dust emission is treated as a black body with a ν^2 emissivity scaled to match the background radiation measured by COBE FIRAS in the faintest area on the sky (Fixsen et al. 1998b). In Figure 3.2, we illustrate the different components which make up our data sets.

Table 3.2

z	$\phi^*(\times 10^{-3}\mathrm{Mpc}^{-3})$	M^*_{AB}	α	Ref.
0.0-0.5	4.07	-18.05	-1.21	Reddy & Steidel (2009)
0.5-1.0	3.0	-19.17	-1.52	Arnouts et al. (2005)
1.0-1.5	1.26	-20.08	-1.84	Arnouts et al. (2005)
1.5-2.0	2.3	-20.17	-1.60	Arnouts et al. (2005)
2.0-2.7	2.75	-20.7	-1.73	Oesch et al. (2010)
2.7-3.4	1.71	-20.97	-1.73	Oesch et al. (2010)
3.4-4.5	1.3	-20.98	-1.73	Bouwens et al. (2007)
4.5-5.5	1.0	-20.64	-1.66	Bouwens et al. (2007)
5.5-6.5	1.4	-20.24	-1.74	Bouwens et al. (2007)
6.5-10.5	0.86	-20.14	-2.01	Bouwens et al. (2011b)

Table 3.2:: Schechter function parameters for the UV Luminosity Functions used to assign SFR to dark matter halos. These parameters are used through abundance matching.

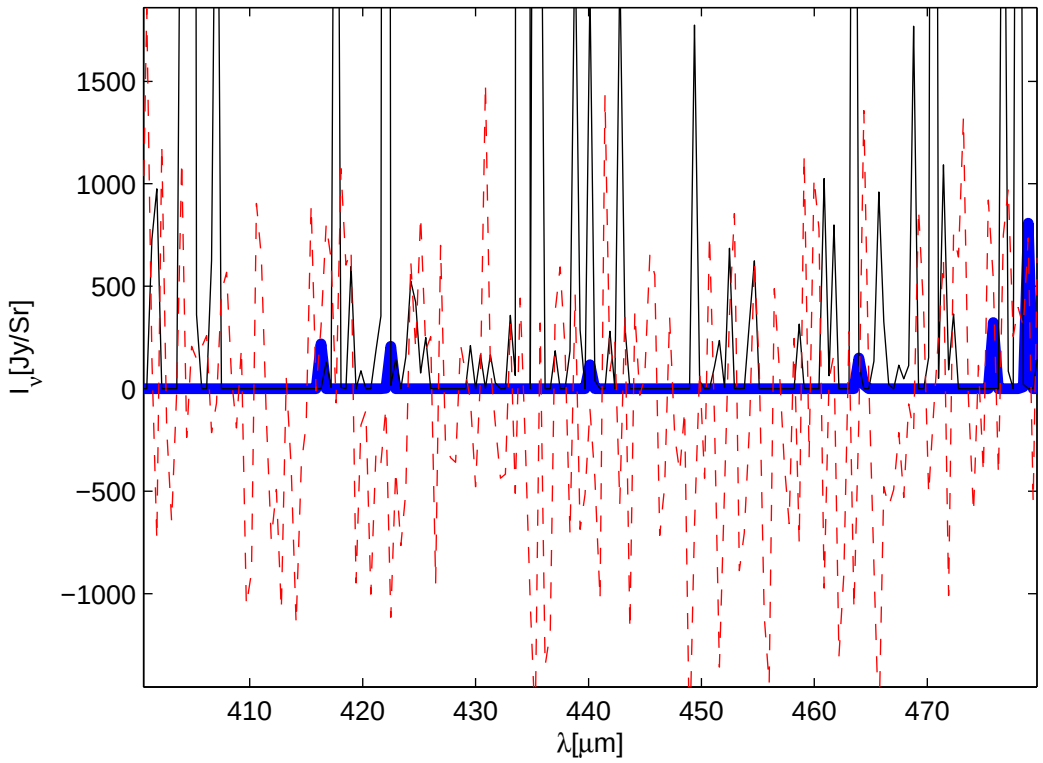

Figure 3.2.—: Various components of the synthetic data set for a typical line of sight. We plot data from the SPICA example discussed below. The thick blue curve is the line emission from the target galaxies, the thin red dashed curve is the contribution from detector noise, and the thin black curve is the emission from all of the bad lines. We have not included the bright astrophysical foregrounds because they are orders of magnitude greater than all of the components plotted here. This emission along with galaxy continuum (not plotted) is removed in the fitting and subtraction step of measuring the power spectrum discussed in the text.

3.2.3 Simulations

To create our synthetic data we simulate the light cone of dark matter in a 100×100 arcmin^2 angular patch of the sky out to high redshift. We use a particle-multi-mesh N-body code to evolve the dark matter distribution (Trac & Pen 2006). The simulation outputs are then stacked along the line of sight out to z = 10.

For most of our light cone, we use an N-body simulation with 2048^3 dark matter particles on an effective mesh with 7680^3 cells in a comoving box with a length of $200h^{-1}$Mpc on a side. This length is sufficient to cover the field of view out to the highest redshifts of interest. For low redshifts ($z < 1$), we use a second larger simulation to improve the sample variance of large halos. This simulation also contains 2048^3 dark matter particles and a mesh of 7680^3 cells, but has a length of $400h^{-1}$Mpc on each side of the box. In both simulations we identify dark matter halos using a spherical overdensity algorithm. This is done by examining snapshots taken every 20 Myr and 40 Myr in the $200h^{-1}$Mpc and $400h^{-1}$Mpc simulations respectively.

The light cone is constructed from a series of redshift zones, each zone spanning one comoving box length. Each zone is constructed from several redshift shells of thickness corresponding to a time interval of 20 or 40 Myr depending on the box size. The shells are stacked in a continuous fashion, but the zones are randomized to eliminate any very long artificial structure. This produces a discontinuity across zone boundaries. We are careful to only measure the power spectrum within one zone for our examples to avoid any problems associated with this discontinuity.

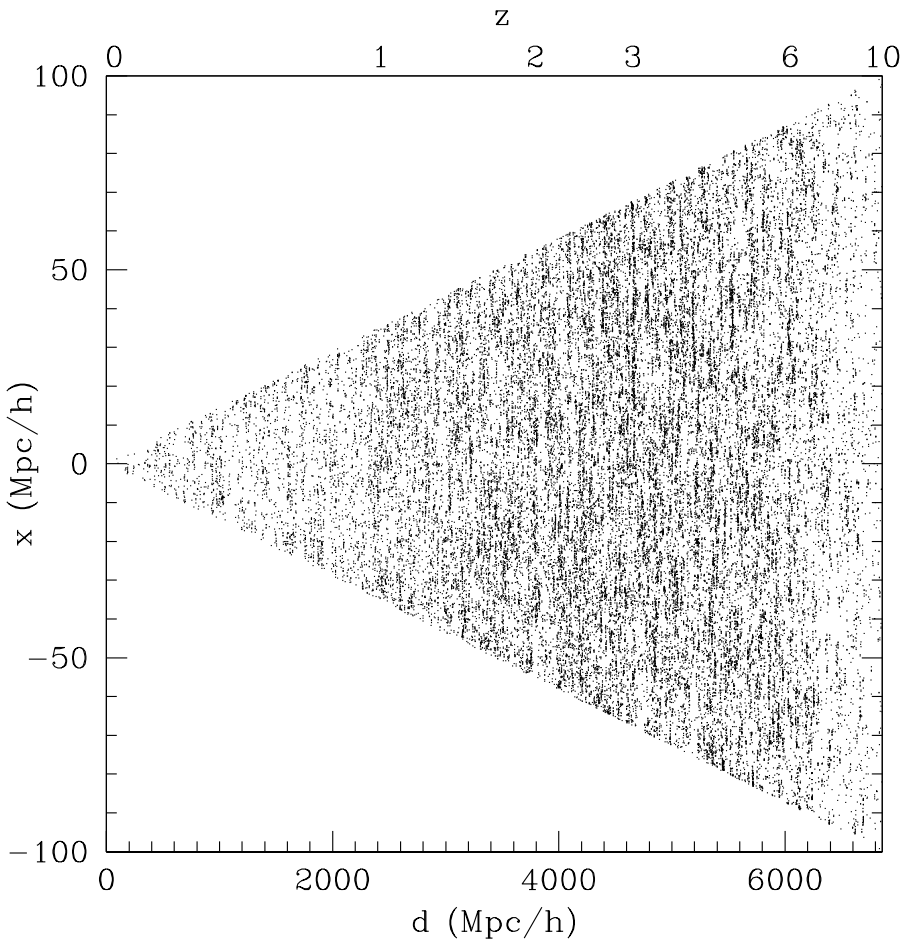

Figure 3.3.—: The positions of dark matter halos from a slice of our simulated light cone projected onto the x-z plane (where z is the direction along the line of sight). The slice has thickness $\Delta y = 0.5h^{-1}$Mpc. Each dark point represents a dark matter halo. Our light cone corresponds to 100×100 arcmin^2 on the sky. The details are explained in Section 3.2.

3.2.4 Cross Power Spectrum Measurement

Measuring the cross power spectrum consists of three main steps:

1. Fitting a smooth function of wavelength to each pixel and subtracting it away (note that we term each line of sight on the sky a "***pixel***" and each spectral component of the 3D data cube a "***voxel***").

2. Masking out *voxels* with bright bad line emission.

3. Taking the product of the Fourier modes to estimate the power spectrum and then averaging in spherical shells in k-space.

We discuss these in turn. The fitting stage is necessary because we seek to measure only the signal coming from line emission and our data contains signal from both galaxy continuum emission as well as bright astrophysical foregrounds and backgrounds. Since these other sources vary slowly in the spectral direction we can remove them by fitting a smooth function of wavelength to each *pixel* on the sky and subtracting it. This is the same procedure which has been discussed extensively in the context of cosmological measurements of 21cm radiation from neutral hydrogen (Petrovic & Oh 2011a; Morales 2005; Wang et al. 2006; McQuinn et al. 2006a; Liu et al. 2009).

More specifically, with our data sets we fit a polynomial in wavelength to the spectrum in each *pixel* and then subtract it away. This removes the foregrounds and galaxy continuum, as well as some large scale fluctuations in line emission along the line of sight. In order to minimize loss of the line signal we do not include *voxels* in our fit which contain bright line emission. We do this by an iterative fit: we fit once to remove the foregrounds and identify the bright *voxels* and then fit again excluding them.

There will necessarily be some signal lost on large scales as a result of the fitting and subtraction stage. Fortunately as discussed in Petrovic & Oh (2011a), if we decompose our signal into Fourier modes, the lost signal is only from small k-modes (corresponding to long wavelengths) along the line of sight. If we exclude these corrupted k-modes in step 3 of measuring the cross power spectrum, we still have an unbiased estimation of the cross power spectrum without subtraction losses. Note that throwing away the low k-modes does have a price. Since there are fewer statistical samples of modes this procedure increases the variance of power spectrum measurements on large scales. Because we wish to minimize the number of these corrupted modes, we fit with the lowest order polynomial which leaves no significant residual foregrounds.

After we have subtracted away the foreground and continuum emission it is necessary to remove *voxels* with very bright bad line emission. This is necessary because even though line emission from bright foreground galaxies does not bias our measurements of the power spectrum it does increase the error of our measurements due to the contribution in Eq. (3.7).

The masking procedure must be done carefully in order to not introduce spurious correlations between the two data sets being cross correlated. For example, if one simply sets all *voxels* above some threshold signal equal to zero, a spurious change to the cross power spectrum is introduced (see Figure 3.4). This is because the location of the brightest *voxels* (mainly due to contaminating bright foreground galaxies) are correlated with the distribution of target line emission. The signal from the bad lines and the target lines overlap so that bright bad lines which appear in the data at locations of over-densities in the target lines are more likely to be above the removal threshold. Thus, the bad lines left after masking in one data cube will be anti-correlated with the target

lines in the other cube. This causes the measured cross power spectrum to be lower than what would be measured from the target lines alone.

In order to avoid this type of complication one can mask out *voxels* in a way which is uncorrelated with the target line emission being measured. This can be done by identifying individual bright sources instead of just removing the brightest *voxels* in the data. The *voxels* with bright contaminating lines can then be set to zero. These sources could be identified by looking at a series of different wavelengths and identifying them with multiple lines. Entirely different surveys could also be used to determine where contaminating lines from bright foreground galaxies will appear and be removed. In our examples below, we assume that all of the galaxies which emit lines brighter than five times the RMS detector noise can be identified directly. When setting the masked *voxels* to zero we treat this as a change in the window function, $W(\vec{r})$, which appears in Eq. (3.6). We normalize this new window function such that $\int W(\vec{r})d^3\vec{r} = 1$.

In the final step, we take the discrete Fourier transform of the two 3D data cubes being cross correlated. The estimation of the power spectrum at some particular k value is then given by the real part of the product of the survey volume, the Fourier mode of one data set, and the complex conjugate of the same Fourier mode in the other data set. This is equivalent to Eq. (3.5). Finally, we break k-space into spherical shells with uniform thickness in $\log(k)$. We then take the average estimated power spectrum of all the modes contained within each shell. As discussed above, we do not include low k-modes along the line of sight which have been contaminated during the fitting and subtraction stage. Specifically, we do not include k-modes which have a component along the line of sight smaller than, $k_{\rm cut}$, the lowest value for which there is no significant contamination. In the examples below we find that for $k_{\rm cut} = 0.06h{\rm Mpc}^{-1}$ there is no

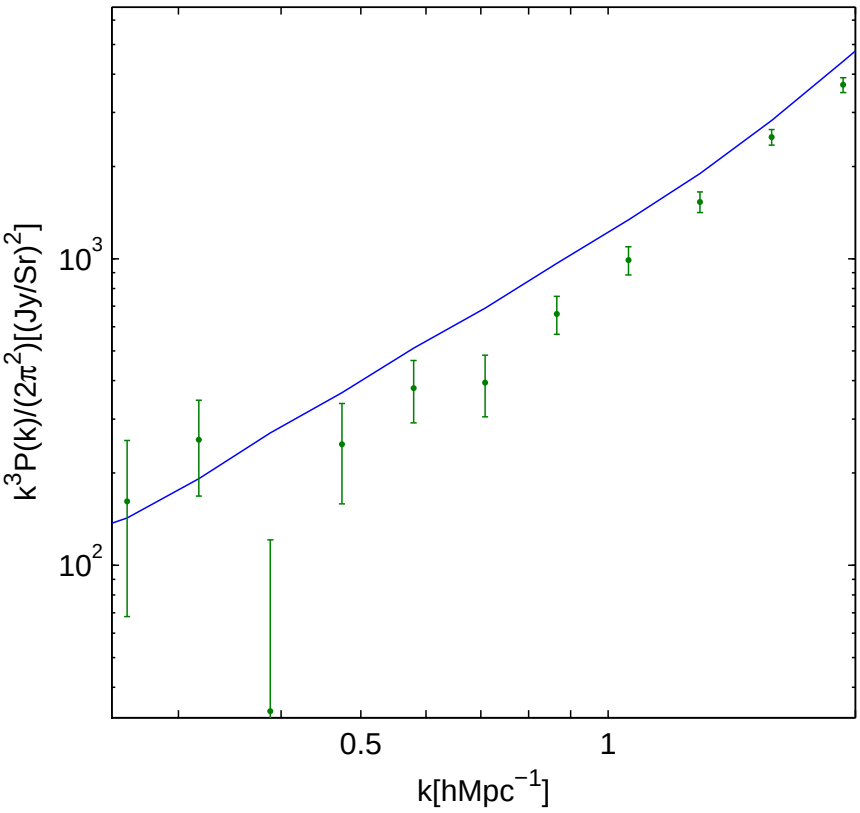

Figure 3.4.—: The measured power spectrum when masking is done by simply setting the fluctuations in all *voxels* with signal greater than five times the RMS detector noise to zero. We use the same instrumental and survey parameters as in Figure 3.5 except we set the detector noise in each data cube to zero to more clearly demonstrate the masking effect. The points plotted are the measurements of the cross power spectrum after all bright *voxels* have been masked and set to zero. The error bars show the standard deviation in the cross power spectrum of all the modes sampled at each k-value. The line is the power spectrum if only the target galaxy lines are included (but using the same mask). Clearly the anti-correlation between the masked bad lines and the target lines in opposite cubes produces a systematic shift in the power spectrum as described in the text.

significant loss of power due to the foreground removal process.

3.3 SPICA

3.3.1 Instrument

We consider two different examples of instruments and lines which could be used to measure the galaxy line cross power spectrum. In our first example, we envision an instrument on the planned Space Infrared Telescope for Cosmology and Astrophysics (SPICA) Swinyard et al. (2009). SPICA is a 3.5 meter space-borne infrared telescope planned for launch in 2017. It will be cooled below 5K, providing measurements which are orders of magnitude more sensitive than those from current instruments. We consider an instrument based on the proposed high performance spectrometer μ-spec (H. Moseley, private communication 2009). This instrument will provide background limited sensitivity with wavelength coverage from $250 - 700\mu m$. A number of μ-spec units will be combined to record both spatial and spectral data in each pointing, which will be perfectly suited for intensity mapping. We assume that spectra for 100 diffraction limited beams can be measured simultaneously with a resolving power of $R = (\nu/\Delta\nu) = 1000$.

3.3.2 Results

We use the simulation described above to create a synthetic data set and measure the cross power spectrum with the SPICA/μ-spec instrument. We cross correlate OI(63 μm) and OIII(52 μm) from galaxies at a redshift of $z = 6$. We assume the data covers a

square on the sky which is 1.7 degrees across (corresponding to 250 Mpc) and a redshift range of $\Delta z = 0.6$ (corresponding 280 Mpc). We assume a total integration time of 2×10^6 seconds spread uniformly across this survey area.

In Figure 3.5, we show that using the procedure described above we can accurately measure the cross power spectrum. We show both the cross power spectrum of the emission from the target lines alone as well as that which is recovered when bad lines, detector noise, and foregrounds are included. The error in measuring the power spectrum is consistent with the analytical prediction derived in Visbal & Loeb (2010). The details introduced in our simulation and measurements, such as removing the foregrounds and masking out bright foreground galaxies, does not bias our estimate of the power spectrum or increase the uncertainty implied by Eq. (3.7). Other details of this example are presented in Table 3.3.

In Figure 3.4, we show the effects on the measured cross power spectrum of masking out all bright *voxels*. We have plotted the power spectrum from the target lines alone and also with the bad lines using the same mask in both cases. Clearly, the anti-correlation between the masked bad lines and the target lines in the other data set described above has biased the cross power spectrum measurement.

We find that increasing the sky coverage (i.e. shorter integrations for each pointing on the sky, but larger sky coverage) increases our errors in the power spectrum. This is due to our assumptions about masking bright bad lines. As the survey becomes wider the detector noise goes up and the increased number of bright bad lines which are not masked increases the errors on the power spectrum. One would not want to go much deeper over a smaller patch of sky than we consider, because we are already masking

Table 3.3

Quantity	OI(63 μm)	OIII(52 μm)
Average Line Signals ($\bar{S}_{\rm line}$)	20Jy/Sr	14Jy/Sr
Fraction of Voxels Masked	0.097	0.11
RMS Detector Noise	700Jy/Sr	400Jy/Sr
Brightness of CMB+Dust	4MJy/Sr	2MJy/Sr
Bad line Power/Noise Power ($k = 0.3h^{-1}$Mpc)	6.5	8.1
Bad line Power/Noise Power ($k = 1h^{-1}$Mpc)	1.4	1.7
Cross Power S/N per k-mode ($k = 0.3h^{-1}$Mpc)	0.17	
Cross Power S/N per k-mode ($k = 1h^{-1}$Mpc)	0.14	

Table 3.3:: Summary of the results from the example of cross correlating OI(63 μm) and OIII(52 μm) with SPICA. The RMS detector noise is the value in each *voxel*. The bad line power to detector noise power ratio gives the relative contributions to the statistical error in the cross power spectrum due to the auto-correlations from all the bad lines and the detector noise which appear in Eq. (3.7).

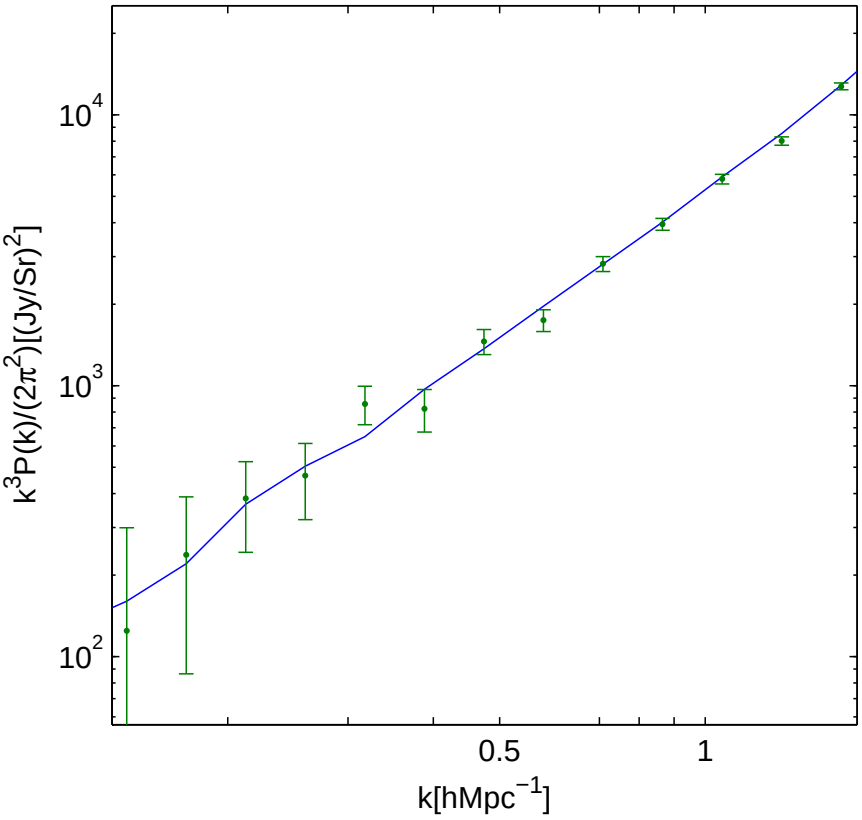

Figure 3.5.—: The cross power spectrum of OI(63 μm) and OIII(52 μm) at $z = 6$ measured from simulated data for our hypothetical instrument modeled after SPICA. The blue curve is the cross power spectrum measured when only line emission from galaxies in the target lines is included. The green points are the recovered power spectrum when detector noise, bad line emission, galaxy continuum emission, and bright astrophysical foreground and background emission (i.e. dust in our galaxy and the CMB) are included. The error bars are the theoretical prediction of the root mean square error derived in Visbal & Loeb (2010) and given by Eq. (3.7). In determining the error bars we have estimated $P_{1\text{total}}$ and $P_{2\text{total}}$ using our simulated data. These errors include detector noise, bad line emission and sample variance.

roughly 10% of each data cube. Without using the increased sensitivity to remove more of the bright bad lines, going deeper and shallower would increase the noise in the power spectrum due to increased sample variance.

If the mask were not dependent on the integration time (e.g. obtained from a different survey of foreground galaxies) it is straight forward to determine in a given time what the optimal sky coverage is for measuring power on a particular scale. Minimizing Eq. (3.7) with respect to time integrated per pointing, holding the total observation time fixed, one finds that the optimal coverage sets $P_{\rm noise1}P_{\rm noise2} = P_{1,2}^2 + (P_{\rm 1total} - P_{\rm noise1})(P_{\rm 2total} - P_{\rm noise2})$. The product of the detector noise power spectra equals the sum of the sample variance contribution to the power spectrum uncertainty.

3.4 Intensity Mapping CO(1-0) and CO(2-1)

As another example we consider intensity mapping the cross correlations between CO(1-0) and CO(2-1) at high redshifts with a dedicated instrument currently being planned (J. Bowman 2011, private communication). Other similar instruments are currently being planned (G. Bower 2011, private communication). This observation consists of two telescopes: a 20 meter dish and a 10 meter dish to observe CO(1-0) and CO(2-1) respectively. Each of these telescopes can simultaneously observe 3 deg^2 of the sky with angular resolution set by the beam size (3.5-5 arcmin at $z = 7 - 10$). We assume a spectral resolution of $R = (\nu/\Delta\nu) = 1000$. While the actual instrument will have a higher resolution this is sufficient to measure fluctuations on the scales we consider. To

determine the detector noise we use the radiometer equation (Wilson et al. 2009),

$$\sigma_T = \frac{T_{\rm sys}}{\sqrt{2t\Delta\nu}}, \tag{3.9}$$

where $T_{\rm sys}$ is the system temperature which we have assumed to be 30K, t is the integration time which we have assumed is 3×10^7s, and the factor of $\sqrt{2}$ appears in the denominator because the intensity will be mapped from dual polarization. We create a synthetic data set for this instrument centered at $z = 7.5$ and the recovered cross power spectrum is shown in Figure 3.6. We summarize some other properties of this simulated measurement in Table 3.4.

3.5 Discussion and Conclusions

By cross correlating emission in different spectral lines from the same galaxies, it is possible to measure their clustering. This clustering, quantified by the line cross power spectrum, can be measured for galaxies which are too faint to detect individually, but which can be observed in aggregate due to their large numbers (Visbal & Loeb 2010).

In this paper, we have shown that the line cross power spectrum can be accurately measured with future instruments, based on synthetic data created using cosmological dark matter simulations. We produced our synthetic data by associating dark matter halos with galaxies and assigning each a spectrum. The continuum was generated by scaling that of M82 with the SFR in each halo and line emission was set by calibrating with lower redshift galaxies. The SFR was computed for halos with an abundance matching technique calibrated to observations of galaxy UV luminosity functions. Our synthetic data also included detector noise and bright emission due to astrophysical

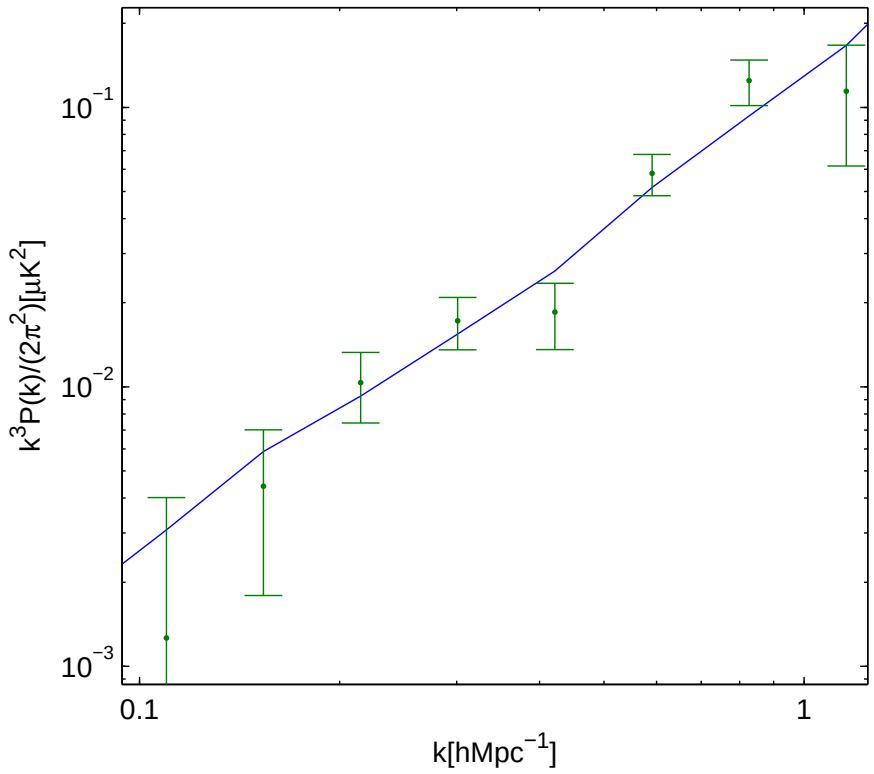

Figure 3.6.—: The cross power spectrum of CO(1-0) and CO(2-1) from a central redshift of $z = 7.5$ measured with the telescope described in Section 3.4. An integration of 3×10^7s and a redshift range of $\Delta z = 0.9$ are assumed. The solid blue line is the power spectrum of the CO line emission alone measured from our simulated data. The green points are the measurements of the power spectrum recovered when the full simulated data set is used. This includes detector noise and bad line emission from the other lines in Table 3.1. The error bars are calculated from Eq. (3.7), where we have estimated $P_{1\text{total}}$ and $P_{2\text{total}}$ using our simulated data. These errors include detector noise, bad line emission and sample variance.

Table 3.4

Quantity	CO(1-0)	CO(2-1)
Average Line Signals ($\bar{S}_{\rm line}$)	0.1μK	0.094μK
Fraction of Voxels Masked	0.0	0.015
RMS Detector Noise	1.0μK	0.7μK
Bad line Power/Noise Power ($k = 0.1h^{-1}$Mpc)	0.0	7.0
Bad line Power/Noise Power ($k = 0.3h^{-1}$Mpc)	0.0	1.5
Bad line Power/Noise Power ($k = 0.8h^{-1}$Mpc)	0.0	0.5
Cross Power S/N per k-mode ($k = 0.1h^{-1}$Mpc)	0.24	
Cross Power S/N per k-mode ($k = 0.3h^{-1}$Mpc)	0.12	
Cross Power S/N per k-mode ($k = 0.8h^{-1}$Mpc)	0.05	

Table 3.4:: Summary of the results from the example of cross correlating CO(1-0) and CO(2-1). The RMS detector noise is the value in each *voxel*. The bad line power to detector noise power ratio gives the relative contributions to the statistical error in the cross power spectrum due to the auto-correlations from all the bad lines and the detector noise which appear in Eq. (3.7).

foregrounds and backgrounds such as that from dust in our galaxy and the CMB. Even if our simple prescription deviates somewhat from reality, it still illustrates our main point, that whatever the underlying power spectrum of emission from galaxies is, it can be measured with the accuracy predicted analytically by Eq. (3.7). It is reassuring that the complications addressed in our simulations such as removal of bright astrophysical foregrounds and masking out bright bad line emission do not hinder measurement of the power spectrum compared to the analytic expectations from Visbal & Loeb (2010).

Measuring the line cross power spectrum consists of three main steps. First, a smooth function such as a polynomial is fit to each *pixel* on the sky and subtracted from the data to remove smooth foregrounds and the continuum emission from galaxies. Next, bright *voxels* are masked out. One must be careful in the masking technique as it is possible to introduce spurious correlations if the masks are correlated with the target lines which appear in both data cubes. This can be avoided if bright sources are found individually at high significance and the corresponding *voxels* with bright contaminating lines are set to zero. Finally, the data is Fourier transformed and then the power spectrum is averaged in spherical shells. Modes corresponding to long wavelengths along the line of sight are not included, because they are contaminated during the fitting and subtraction step.

We find that the line cross power spectrum can be measured with the accuracy predicted analytically by Eq. (3.7), derived in Visbal & Loeb (2010). In particular, we tested two hypothetical instruments, an instrument mounted on SPICA and a pair of large ground based telescopes designed to measure the emission of CO(1-0) and CO(2-1). Though not included in our examples, it would also be valuable to measure emission from more than two different lines from the same redshifts. This could improve statistics

and allow determination of the ratio of line emission in different lines by taking the ratio of different cross power spectra.

Our results suggest that cross correlating galaxy line emission is a promising technique for studying high redshift galaxies. It will enable one to measure the evolution of the total line signal from all galaxies at a particular redshift, even those that are too faint to be resolved individually. This could reveal details about the evolution of galaxies' properties such as SFR density or average metallicity. It may also be possible to use these observations to study the history of cosmic reionization, both by estimating the ionizing flux from faint galaxies and by looking for a sharp change in signal versus redshift due to the change in the minimum mass of halos which host galaxies.

Acknowledgments

We thank Judd Bowman for helpful discussions. This work was supported in part by NSF grant AST-0907890 and NASA grants NNA09DB30A and NNX08AL43G (for A.L.).

Chapter 4

Cosmological Constraints from 21cm Surveys After Reionization

E. Visbal, A. Loeb, & S. Wyithe *Journal of Cosmology and Astroparticle Physics*, Issue 10, ID 030, 2009

Abstract

21cm emission from residual neutral hydrogen after the epoch of reionization can be used to trace the cosmological power spectrum of density fluctuations. Using a Fisher matrix formulation, we provide a detailed forecast of the constraints on cosmological parameters that are achievable with this probe. We consider two designs: a scaled-up version of the MWA observatory as well as a Fast Fourier Transform Telescope. We find that 21cm observations dedicated to post-reionization redshifts may yield significantly better constraints than next generation Cosmic Microwave Background (CMB) experiments.

We find the constraints on Ω_Λ, $\Omega_{\rm m}h^2$, and $\Omega_\nu h^2$ to be the strongest, each improved by at least an order of magnitude over the Planck CMB satellite alone for both designs. Our results do not depend as strongly on uncertainties in the astrophysics associated with the ionization of hydrogen as similar 21cm surveys during the epoch of reionization. However, we find that modulation of the 21cm power spectrum from the ionizing background could potentially degrade constraints on the spectral index of the primordial power spectrum and its running by more than an order of magnitude. Our results also depend strongly on the maximum wavenumber of the power spectrum which can be used due to non-linearities.

4.1 Introduction

Recently, there has been much interest in the feasibility of mapping the three-dimensional distribution of cosmic hydrogen through its spin-flip transition at a resonant rest frame wavelength of 21cm (Furlanetto et al. 2006a; Barkana & Loeb 2007). Several first generation experiments are being constructed to probe the epoch of reionization (MWA[1], LOFAR[2], PAPER[3], 21CMA[4]) and more ambitious designs are being planned (SKA[5]).

One driver for mapping hydrogen through 21cm emission is to measure cosmological

[1]http://www.haystack.mit.edu/ast/arrays/mwa

[2]http://www.lofar.org

[3]http://www.astro.berkeley.edu/dbacker/EoR

[4]http://web.phys.cmu.edu/ past

[5]http://www.skatelescope.org/

parameters from the underlying cosmic power spectrum. During the epoch of reionization (EoR), the 21cm power spectrum is shaped mainly by the structure of ionized regions. Even without precise knowledge of the ionization power spectrum it is possible to isolate the cosmological power spectrum by exploiting anisotropies in redshift space due to peculiar velocities (Barkana & Loeb 2005a; McQuinn et al. 2006a).

Recent work (Mao et al. 2008; Pritchard & Pierpaoli 2008) has shown that the 21cm power spectrum accessible during the EoR has the potential to put tight constraints on cosmological parameters; however, these constraints depend on model-dependent uncertainties, the most important of which involves the ionization power spectrum.

In this paper, we explore in detail the constraints achievable from mapping the residual cosmic hydrogen after reionization (Wyithe & Loeb 2008; Wyithe et al. 2008; Chang et al. 2008; Loeb & Wyithe 2008; Pen et al. 2009b). The hydrogen resides in pockets of dense galactic regions which are self-shielded from the UV background, also known as damped Lyman-α absorbers (DLAs) in quasar spectra (Wolfe et al. 2005). In difference from traditional galaxy redshift surveys, 21cm surveys do not need to resolve individual galaxies but rather are able to monitor the smooth variation in their cumulative 21cm emission owing to their clustering on large scales (Loeb & Wyithe 2008).

Measuring the 21cm power spectrum after reionization offers several key advantages as compared to the EoR. First, the near uniformity of the UV radiation field guarantees that the 21cm power spectrum would reliably trace the underlying matter power spectrum. However, the UV background could introduce a scale dependent modulation to the 21cm power spectrum as large as one percent (Wyithe & Loeb 2009). This

modulation could introduce degeneracies that would significantly weaken constraints on the spectral index of the primordial power spectrum and its running. Another advantage of probing low redshifts is that the brightness temperature of the galactic synchrotron emission scales as $(1+z)^{2.6}$. However, this advantage is offset by the fact that the mass weighted neutral fraction of hydrogen is only a few percent at redshifts $z \lesssim 6$ (Prochaska et al. 2005).

In this paper we use the Fisher matrix formalism to quantify how effectively futuristic surveys dedicated to post-reionization redshifts ($z \lesssim 6$) can constrain cosmology. We consider both a survey with ten times the number of cross dipoles of the MWA Bowman et al. (2009) ($5000 \times 16 = 8 \times 10^4$) but operating at higher frequencies, which we term MWA5000, and a Fast Fourier Transform Telescope (FFTT) with 10^6 dipoles over a square kilometer area (Tegmark & Zaldarriaga 2009). We also show results for the combination of these surveys and a next generation Cosmic Microwave Background (CMB) experiment (Planck).

This paper is structured as follows. In Section 4.2 we discuss the detectability of the 21cm signal after reionization and in Section 4.3 we discuss its power spectrum. In Section 4.4 we consider the details of our Fisher matrix calculation and in Section 4.5 we present its results. Finally, we discuss and summarize our conclusions in Sections 4.6 and 4.7.

4.2 Detectability of the 21cm Signal After Reionization

Reionization starts with ionized (HII) regions around galaxies which grow and eventually overlap. This overlap of HII regions characterizes the end of the EoR. It was once thought that the 21cm signal would disappear after this transition because there is little neutral hydrogen left. Recent work has shown that this is not the case (Wyithe & Loeb 2008; Loeb & Wyithe 2008; Wyithe 2008; Wyithe & Loeb 2009; Pritchard & Loeb 2008). The *detectability* of the signal may not decline substantially following the end of the EoR because the Galactic synchrotron foreground is weaker at higher frequencies (lower redshifts of the 21cm emission).

After reionization most of the remaining neutral hydrogen is expected to reside in DLAs. Observations have shown that out to $z \approx 4$ the cosmological density parameter of HI is $\Omega_{\rm HI} \approx 10^{-3}$ (Prochaska et al. 2005). This corresponds to a mass-averaged neutral fraction of a few percent. It does not contribute significantly to the Lyα forest, which is mostly shaped by the much smaller volume-averaged neutral fraction. A 21cm survey like the ones we discuss are sensitive to all neutral hydrogen within the survey volume because no galaxies are individually identified and thus there is no minimum threshold for the detection of individual galaxies.

Even though the majority of the neutral hydrogen resides in self shielded clumps, self absorption is not expected to significantly reduce the 21cm signal. This is supported by 21cm absorption studies of DLAs over the redshift interval $0 < z \lesssim 3.4$, which exhibit an optical depth to 21cm absorption of the radio flux from a background quasar

of less than a few percent (Kanekar & Chengalur 2003; Curran et al. 2007). These observations are supported by theoretical calculations of the 21cm optical depth of neutral gas in high redshift minihalos (Furlanetto & Loeb 2002). We also note that the spin temperature in DLAs is much higher than the CMB temperature and thus the 21cm signal is independent of the kinetic temperature of the gas (Kanekar & Chengalur 2003).

At $z \approx 4$ the 21cm brightness temperature contrast with the CMB will be roughly 0.5 mK. On scales of 10 comoving Mpc, the *rms* amplitude of density fluctuations is roughly $\sigma \approx 0.2$, so we expect 21cm fluctuations at a level of ≈ 0.1mK. This is only an order of magnitude or so less than the largest fluctuations expected during the EoR (Wyithe & Morales 2007). These fluctuations combined with the lower brightness temperature of galactic synchrotron emission, which scales as $(1+z)^{2.6}$, should provide a detectable signal. Previous work (e.g. Figure 10 in Ref.(Pritchard & Loeb 2008)) shows that the signal to noise ratio of the 21cm signal after reionization may be similar or even higher than that during the EoR. However, it is important to note that it will be necessary to build special instruments which are optimized to these redshifts to obtain the type of results discussed in this paper.

4.3 21cm Power Spectrum

Next, we describe the 21cm power spectrum after the epoch of reionization. A complete discussion of the relevant physics can be found in Refs. (Furlanetto et al. 2006a; Loeb & Wyithe 2008; Wyithe & Loeb 2008, 2009). The difference between the average brightness

temperature of 21cm emission at redshift z and the CMB temperature is described by

$$\bar{T}_{\rm b} \approx 26 \bar{x}_{\rm H} \left(\frac{\bar{T}_{\rm s} - T_{\rm CMB}}{\bar{T}_{\rm s}} \frac{\Omega_{\rm b} h^2}{0.022} \right) \left(\frac{0.15}{\Omega_{\rm m} h^2} \frac{1+z}{10} \right)^{1/2} {\rm mK}, \tag{4.1}$$

where $\bar{x}_{\rm H}$ is the global neutral hydrogen fraction and $T_{\rm s}$ is the HI spin temperature. In Fourier space, the power spectrum of 21cm brightness fluctuations is defined by $(2\pi)^3 \delta^3(\mathbf{k} - \mathbf{k}') P_{21}(\mathbf{k}) \equiv \langle \Delta T_{\rm b}(\mathbf{k})^* \Delta T_{\rm b}(\mathbf{k}') \rangle$, where $\mathbf{k}$ is the wave-vector of a given Fourier mode and $\Delta T_{\rm b}(\mathbf{k})$ is the brightness temperature fluctuation in Fourier space.

Before giving its exact form, we stress that the most important feature of $P_{21}(\mathbf{k})$ after reionization is that it essentially traces the cosmological matter power spectrum, $P(k)$. Extracting the cosmological power spectrum will make it possible to place tight constraints on many cosmological parameters. During the EoR the situation is more complicated. $P_{21}(\mathbf{k})$ contains additional terms which depend on the ionization power spectrum and the cross power-spectrum between the ionization and matter distributions.

Following the derivation of Ref. (Wyithe & Loeb 2009) we find that after reionization

$$P_{21}(\mathbf{k}) = \tilde{T}_{\rm b}^2 \bar{x}_{\rm HI}^2 P(k) \left[B(\mathbf{k}) + f\mu^2 \right]^2 . \tag{4.2}$$

Here $\tilde{T}_{\rm b} = \bar{T}_{\rm b} / (\bar{x}_{\rm HI}(\bar{T}_{\rm s} - T_{\rm CMB})/T_{\rm S})$, $B(\mathbf{k})$ is the average scale dependent, $\bar{x}_{\rm HI}$ mass-weighted bias for the DLA host galaxies, and $\mu = \cos\theta$ where θ is the angle between the line of sight and the wave-vector $\mathbf{k}$ (Wyithe 2008; Wyithe & Loeb 2009). The factor $[B(\mathbf{k}) + f\mu^2]^2$ arises due to redshift space anisotropies from line of sight peculiar velocities (Kaiser 1987; Bharadwaj & Ali 2004; Barkana & Loeb 2005a). Here the growth index is defined as $f = d\ln D / d\ln a$, where $D(z)$ is the growth factor of density perturbations and a is the cosmic scale factor. The bias factor arises because the residual neutral hydrogen is located in host galaxies which are biased with respect to the underlying dark

matter distribution. This bias and the neutral hydrogen fraction are the only quantities in the above equation which do not depend solely on fundamental physics.

While the near uniformity of the ionizing UV background causes $P_{21}(\mathbf{k})$ to trace the cosmological power spectrum, fluctuations introduce a modulation that could modify the power spectrum by less than one percent (Wyithe & Loeb 2009). This modulation of the power spectrum adds a scale dependent correction factor to the host galaxy bias. The average bias $B(\mathbf{k})$ is equal to the mean halo bias $\bar{b}$, multiplied by a factor $(1 - K(k))$. In Section 4.8, we derive an expression for $K(k)$ for the case where the mean-free-path of ionizing photons is independent of position. If the effect of the ionizing background is near the maximum which could be expected it may be necessary to model it in order to estimate cosmological parameters reliably. In Section 4.5, we show how cosmological constraints would likely be affected by degeneracies with nuisance parameters introduced by a scale dependent bias model.

The bias, b, for halos of a particular mass M can be derived using the Press-Schechter formalism modified to include non-spherical collapse (Sheth et al. 2001)

$$b(M,z) = 1 + \frac{1}{\delta_{\rm c}}\left[\nu'^2 + b\nu'^{2(1-c)} - \frac{\nu'^{2c}/\sqrt{a}}{\nu'^{2c} + b(1-c)(1-c/2)}\right], \tag{4.3}$$

where $\nu'^2 = a\delta_{\rm c}^2/\sigma^2(M,z)$, $a = 0.707$, $b = 0.5$, and $c = 0.6$. Here $\sigma^2(M,z)$ is the variance of the density field smoothed on a mass scale M and $\delta_{\rm c}$ is the linear over-density threshold for collapse at redshift z.

Assuming that the neutral gas to halo mass ratio is independent of mass, we can derive the mean bias at a particular redshift, $\bar{b}$, as the weighted average

$$\bar{b} = \frac{\int_{M_{\rm min}}^{\infty} \frac{dn}{dM} b(M,z) M dM}{\int_{M_{\rm min}}^{\infty} \frac{dn}{dM} M dM}, \tag{4.4}$$

where dn/dM is the Sheth-Tormen mass function of dark matter halos (Sheth et al. 2001). The minimum halo mass $M_{\rm min}$ defines the threshold for assembling heated gas out of the photo-ionized intergalactic medium, corresponding to a minimum virial temperature $T_{\rm vir} \approx 10^5 K$ (Wyithe & Loeb 2006; Efstathiou 1992; Shapiro et al. 1994; Thoul & Weinberg 1996; Hui & Gnedin 1997; Mesinger & Dijkstra 2008). The appropriate value of $M_{\rm min}$ will depend on the mass of galaxies which host DLAs, however we find our results insensitive to the exact choice of $M_{\rm min}$ (see Section 4.5).

A constant virial temperature leads to the redshift dependence $M_{\rm min} = 5.3 \times 10^9 \left((1+z)/4.5\right)^{-1.5} M_\odot$. Based on observations of DLAs (Prochaska et al. 2005), we assume a fiducial value of neutral hydrogen density to be $x_{\rm HI1} = 0.02$.

Previous work has suggested that at high redshifts the galaxy power spectrum may be affected by reionization (Babich & Loeb 2006; Wyithe & Loeb 2007b). In Babich & Loeb (2006) it is shown that fluctuations in the redshift of reionization in different locations leads to variation in the minimum mass of galaxies which can be assembled. This creates a scale dependent modulation of the power spectrum. Recent observations find that at $z \approx 3$ galaxies with virial velocities $< 50 - 70$km/s contribute little to DLAs and that most DLAs are hosted within halos having viral velocities between $V = 100 - 150$ km/s (Barnes & Haehnelt 2009). Since DLAs and thus most of the remaining neutral hydrogen after reionization is not found in the smallest galaxies we do not expect changes in the minimum mass of galaxies which are assembled to have an important effect on the 21cm power spectrum.

In Wyithe & Loeb (2007b), the effects of reionization on the galaxy power spectrum for more massive galaxies are explored. Reionization is found to change the power

spectrum, but this was due to reionization modifying the average stellar age of galaxies and hence the mass to light ratio. We do not expect this to significantly effect the neutral hydrogen hosted in galaxies. Additionally the modulation of the power spectrum was found to be approximately scale independent, which would not be degenerate with cosmological parameters discussed in this work.

4.3.1 Non-Linear Effects on Baryon Acoustic Oscillations

It has been recently shown that non-linear effects may change the baryon acoustic oscillations (BAO) signature at larger scales than those previously considered (Seo & Eisenstein 2007). The erasure of BAO information due to non-linear effects can be written as

$$P_{\rm b,nl}(k,\mu) = P_{\rm b,lin}(k) \times \exp\left[-\frac{k^2}{2}\left((1-\mu^2)\Sigma_\perp^2 + \mu^2\Sigma_\parallel^2\right)\right], \tag{4.5}$$

where $P_{\rm b}$ is the part of the power spectrum which contains the wiggles from the BAO, $\Sigma_\perp = \Sigma_0 D(z)$, $\Sigma_\parallel = \Sigma_0(1+f)D(z)$, $\Sigma_0 = 11.6h^{-1}$Mpc, and $D(z)$ is the growth function normalized to $(1+z)^{-1}$ at high redshifts. In our Fisher matrix calculations $(P_{\rm b,nl}(k) + P_{\rm smooth}(k))$ is used in place of $P(k)$ in Eq. 4.2. $P_{\rm b,lin}(k) = P(k) - P_{\rm smooth}(k)$, where $P_{\rm smooth}(k)$ is a low order polynomial fit to $P(k)$ in log-log space. This fit removes the wiggles from the BAO, such that $P_{\rm b}$ is just the part of the power spectrum containing the BAO wiggles. Our choice of Σ_0 corresponds to the value determined by simulations and scaled linearly with σ_8 to fit our fiducial cosmology. The scales implied by $\Sigma_\perp$ and $\Sigma_\parallel$ are held fixed in observable units such that the exponential suppression can be taken outside of the derivatives in the Fisher matrix formalism described below. This ensures that the BAO erasure does not in any way improve the forecasted errors on cosmological

parameters.

We emphasize that the exponential suppression of the power spectrum in Eq. 4.5 is only applied to the the BAO wiggles after the smooth linear power has been subtracted off. The power spectrum used in the derivatives which enter the Fisher matrix described below is the sum of the wiggles suppressed by Eq. 4.5 and the unsuppressed smooth linear power spectrum. For the error on P_{21} which enters the Fisher matrix we do not suppress either the wiggles or the smooth part of the power spectrum.

4.4 Fisher Matrix Formulation

Given a set of parameters λ_i, the Fisher matrix formalism provides an estimation of the error for each of the parameters associated with some data set (Tegmark et al. 1997). The 1σ errors on parameters can be estimated as

$$\Delta\lambda_i = \sqrt{F_{ii}^{-1}}, \tag{4.6}$$

where

$$F_{ij} = \sum_{pixels} \frac{1}{\delta P_{12}^2} \left(\frac{\partial P_{21}}{\partial \lambda_i}\right) \left(\frac{\partial P_{21}}{\partial \lambda_j}\right), \tag{4.7}$$

(McQuinn et al. 2006a; Mao et al. 2008), P_{21} is the total 21cm power spectrum, and δP_{21} is the uncertainty on a measurement of the power spectrum. The relevant derivatives have been calculated using the transfer functions from CAMB[6].

We work in **u**-space rather than **k**-space as described in Mao et al. (2008); McQuinn et al. (2006a) to simplify calculating Alcock-Paczynski effects. A radio interferometer

[6]http://camb.info/

directly measures visibilities,

$$V(u,v,\nu) = \int d\hat{\mathbf{n}} \Delta T_{\rm b}(\hat{\mathbf{n}},\nu) A_\nu(\hat{\mathbf{n}}) e^{2\pi i (u,v)\cdot\hat{\mathbf{n}}}, \tag{4.8}$$

where V is the visibility for a pair of antennae and A_ν is the contribution to the primary beam in the $\hat{\mathbf{n}}$ direction. Here we have used the flat sky approximation. This is appropriate even in the case of the FFTT, which images the entire hemisphere, because essentially all of the cosmological information in our surveys is found on small angular scales. The vector $\mathbf{u}_\perp = (u,v)$ corresponds to the number of wavelengths between the pair of antennae. Performing the Fourier transform $I(\mathbf{u}) = \int d\nu V(u,v,\nu)\exp(2\pi i\nu\eta)$, we obtain a signal in terms of $\mathbf{u} = u\hat{\mathbf{i}} + v\hat{\mathbf{j}} + \eta\hat{\mathbf{k}}$, where η has units of time and $\hat{\mathbf{k}}$ is the unit vector along the line of sight. Note that there is a one to one correspondence between $\mathbf{k}$ and $\mathbf{u}$ given by $2\pi\mathbf{u}_\perp/d_A = \mathbf{k}_\perp$ perpendicular to the line of sight and $2\pi\mathbf{u}_\parallel/\tilde{y} = \mathbf{k}_\parallel$ along the line of sight, where d_A is the angular diameter distance to the observation and $\tilde{y}$ is the ratio of comoving distance to frequency interval. With the Fourier conventions above we have $P_{21}(\mathbf{k}) = P_{21}(\mathbf{u})d_A^2\tilde{y}$. Working in $\mathbf{u}$-space simplifies our calculation because $P_{21}(\mathbf{u})$ is measurable without cosmological assumptions and thus Eq. (4.7) can be applied directly. If we were to work in $\mathbf{k}$-space, the Alcock-Paczynski effect would distort $P_{21}(\mathbf{k})$ from Eq. (4.2) when we take derivatives with respect to cosmological parameters.

Because we are considering discrete sources, the total 21cm power spectrum will be the sum of Eq. (4.2) and a shot noise term $P_{\rm shot} = P_{21}(k)/(\bar{b}^2 P(k) n_{\rm DLA})$, where $n_{\rm DLA}$ is the effective number density of the galaxies which host DLAs, $P_{21}(k)$ is $P_{21}(\mathbf{k})$ along the line of sight, and $\bar{b}^2 P(k)$ is the power spectrum of DLA hosting galaxies along the line of sight.

Any constant $|\mathbf{k}|$ and θ define an annulus of constant $P_{21}(\mathbf{u})$. The Fisher matrix

is calculated from Eq. (4.7) by summing the contribution from annuli which fill all of **k**-space accessible to an observation. We divide a 21cm survey into redshift bins small enough for the redshift evolution of $P(k)$ across a bin to be negligible. A separate Fisher matrix is calculated for each redshift bin and then summed into a Fisher matrix which reflects the information about the entire survey.

To calculate the error in Eq. (4.7) we follow the work of McQuinn et al. (2006a); Morales (2005). The error on P_{21} for a particular $|\mathbf{k}|$ and θ is

$$\delta P_{21} = \frac{P_{21} + P_{\rm shot} + P_N}{\sqrt{N_{\rm c} \times N_{\rm fields} \times B_{\rm tot}/B}}, \tag{4.9}$$

where P_N is the noise power spectrum of an interferometer, B is the bandwidth over which foregrounds can be removed, $B_{\rm tot}$ is the total accessible bandwidth, $N_{\rm fields}$ is the number of fields being imaged, and $N_{\rm c}$ is the number of independent cells in **k**-space. The number of cells in an annulus of constant $P_{21}(\mathbf{u})$ is well approximated by

$$N_{\rm c} = 2\pi k^2 \sin\theta \Delta k \Delta\theta \frac{V}{(2\pi)^3}, \tag{4.10}$$

where V is the comoving volume observed by the experiment, $\Delta\theta$ and Δk are the angular and **k**-space widths of the annulus. We choose Δk and $\Delta\theta$ such that $P_{21}(\mathbf{u})$ is essentially constant. The noise of an interferometer is given by

$$P_{\rm N}(u_\perp) = \left(\frac{\lambda^2 T_{\rm sys}}{A_{\rm e}}\right)^2 \frac{1}{t_0 n(u_\perp)}, \tag{4.11}$$

where $\lambda = 21{\rm cm} \times (1+z)$ is the observed wavelength, $T_{\rm sys}$ is the system temperature of the interferometer, $A_{\rm e}$ is the effective area, t_0 is the total observing time, and $n(u_\perp)$ is the number density of baselines. This error is identical to that applicable in studies of the EoR with the exception of the shot noise (Mao et al. 2008; McQuinn et al. 2006a).

The sensitivity of 21cm measurements will be impacted by how effectively foregrounds such as the galactic synchrotron emission can be removed. Wang et al. (2006); McQuinn et al. (2006a); Jelić et al. (2008) suggest that after fitting out a low order polynomial, residual foregrounds in the power spectrum will be negligible if the frequency band over which foregrounds are removed, B, is substantially smaller than the total band-pass available. This is true for wave-vectors greater than $k_{\rm min} = 2\pi/(\tilde{y}B)$. Recent work estimating errors on cosmological parameters with 21cm surveys during the EoR has used this assumption in modeling foreground removal (Mao et al. 2008; Pritchard & Pierpaoli 2008; McQuinn et al. 2006a). It is encouraging that we find parameter constraints to depend relatively weakly on the exact value of the bandwidth over which foregrounds are removed (see Section 4.5). We note that while we expect these assumptions pertaining to foreground removal to be robust, the true ability to remove foregrounds may not be known until first generation 21cm instruments are operational.

There are several factors which limit the scales accessible to 21cm surveys for parameter determination. As discussed above, we assume that foregrounds can not be effectively removed from pixels with $k < k_{\rm min}$. There is also a minimum accessible value of $k \sin\theta$ imposed by the minimum baseline, $b_{\rm min} \approx \sqrt{A_{\rm phys}}$. We exclude information for k values above the linear scale. We compare the linear power spectrum for our fiducial cosmology to a non-linear power spectrum produced by HALOFIT in CAMB, and define our non-linear cutoff as the k value where there is a 10% discrepancy.

The precision of the measurements discussed in this paper will require a theoretical prediction of the matter power spectrum which is accurate to better than one percent. The k cutoff is meant to represent the scale to which future N-body simulations, such

as those discussed in (Heitmann et al. 2009, 2010), will be able to calculate the power spectrum to the required accuracy. Since the exact value of this scale is unknown we present the dependence of varying it on cosmological parameter constraints below.

The value of this cutoff is fairly conservative when compared to the criterion of Seo & Eisenstein (2003) which chooses $k_{\rm nl} = \pi/2R$ for a value of R giving an *rms* density fluctuation amplitude $\sigma(R) = 0.5$. The latter criterion has been used for 21cm parameter constraints at higher redshifts than we explore (Pritchard & Pierpaoli 2008). The $k_{\rm max}$ values corresponding to different levels of discrepancy between the linear and non-linear power spectra are shown in Figure 4.1.

We also include constraints when combined with future data from the Planck satellite[7]. The method used to calculate the corresponding Fisher matrix was adopted from (Jungman et al. 1996; Zaldarriaga & Seljak 1997).

4.4.1 Survey Characteristics

We apply the Fisher matrix formulation to future surveys dedicated to low redshifts similar in design to MWA5000 and a Fast Fourier Transform Telescope (FFTT). We show results with surveys designed for a central redshift of 3.5 and 1.5 that each span a factor of 3 in $(1 + z)$.

We model the MWA5000 observatory as an interferometer with 5000 tiles each containing 16 dipole antennae. For the survey centered at $z = 3.5(1.5)$ we assume a constant core of antennae out to 40(22)m and then a r^{-2} distribution out to 580(278)m.

[7]http://sci.esa.int/planck/

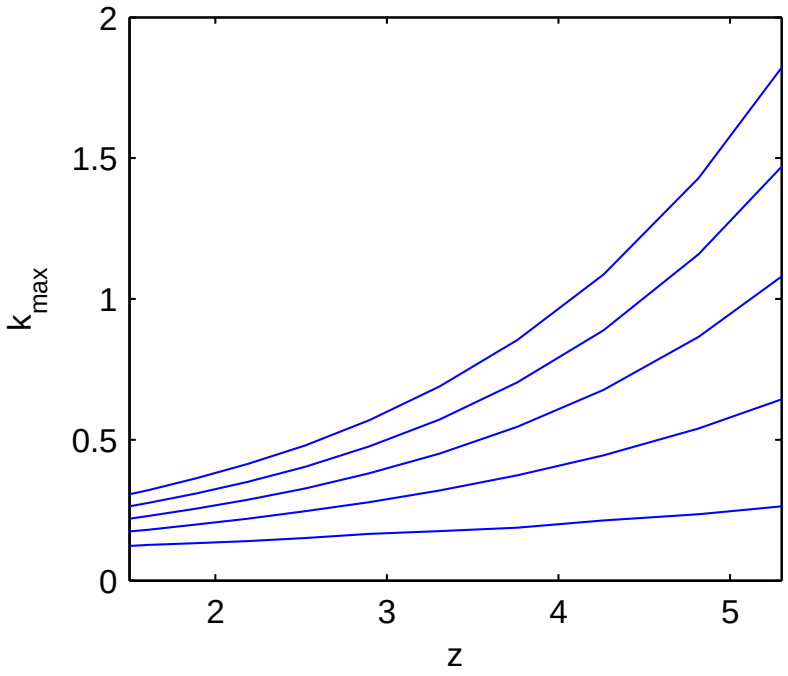

Figure 4.1.—: Maximal wavenumber, $k_{\rm max}$, above which the non-linear power-spectrum deviates from the linear power-spectrum by more than $25\%, 20\%, 15\%, 10\%$ and 5% (top to bottom). Larger discrepancies produce higher values of $k_{\rm max}$.

This layout gives roughly the same baseline density distribution as MWA does at higher redshifts (McQuinn et al. 2006a).

The angular resolution of the telescope is set by the baseline density distribution. The longest baseline corresponds to the highest value of $k_\perp$ that can be probed, $2\pi \mathbf{u}_{\perp,max}/d_A = \mathbf{k}_{\perp,max}$. The above distribution of antennae contains baselines which are long enough to resolve k_{max} at all redshifts. We assume a frequency resolution of 0.01 MHz for all surveys considered. These arrays will have better resolution than this, but this is sufficient to resolve the scales set by k_{max}.

For the survey centered around $z = 3.5$ the effective area of each tile $A_{\rm e} \approx N_{\rm dip}\lambda^2/4$ and is limited by the physical area of the tile, $A_{\rm phys}$ (Bowman et al. 2006). The values of $A_{\rm phys}$ are chosen such that $A_{\rm phys} \approx A_{\rm e}$ at the central redshift. For the low-redshift case, we assume that dishes are used instead of antennae, resulting in $A_{\rm e} \approx A_{\rm phys}$.

We model an FFTT observatory (Tegmark & Zaldarriaga 2009) as an interferometer with 10^6 evenly spaced dipoles over a square kilometer that can all be correlated. The noise in each dipole is calculated separately with $A_{\rm e} \approx \lambda^2/4$ limited by $A_{\rm phys} = S^2$, where S is the spacing of the dipoles on a square grid.

We have assumed that foregrounds can be removed on scales of up to $30[4.5/(1+z)]$MHz. This corresponds to the value that Loeb & Wyithe (2008) cite as desirable to measure the neutrino signal. The exact choice of this bandwidth is relatively unimportant, as our results depend weakly on this value (see Section 4.5). We assume that 0.65 of the sky in one hemisphere is imaged for 2000 hours. This corresponds to roughly 16 fields of view. The partial coverage is due to foregrounds which can not be removed in the vicinity of the galactic plane. We also show results for a more

conservative case using MWA5000 over three fields of view rather than 16.

For all surveys we assume a redshift range corresponding to a factor of 3 in frequency and break each observation into redshift bins of width $\Delta z = 0.1(1+z)$. The factor of 3 corresponds to the largest frequency bandwidth over which a low frequency dipole antenna has suitable sensitivity. In our lower redshift case we have assumed that dishes will be used. These could potentially have a larger bandwidth than the dipole antennae, but we conservatively use the same factor of 3 in frequency. We also assume that $T_{\rm sys} = T_{\rm sky} + T_{\rm inst}$ where the sky temperature $T_{\rm sky} = 260\,[(1+z)/9.5]^{2.55}$ (Rogers & Bowman 2008), and that the instrumental temperature is 30K in an optimistic case and 100K in a pessimistic case, corresponding to what is reasonable with current technology and what might be expected by the time the hypothetical experiments we discuss will be built.

4.4.2 Cosmological Parameters

Throughout this work we assume that the true background cosmology is that of a flat ΛCDM Universe with density parameters $\Omega_\Lambda = 0.7$ in dark energy, $\Omega_{\rm m}h^2 = 0.147$ in matter, $\Omega_{\rm b}h^2 = 0.023$ in baryons, and $\Omega_\nu h^2 = 0.00054$ in neutrinos, and with values of $A_{\rm s}^2 = 25.0 \times 10^{-10}$, $n_{\rm s} = 0.95$, and $\alpha = 0.0$ for the spectral index, amplitude, and running of the primordial power spectrum. The chosen value of $A_{\rm s}$ corresponds to an *rms* fluctuation amplitude on a $8h^{-1}$ Mpc scale of $\sigma_8 = 0.84$. We have assumed a neutrino hierarchy with one dominant species having a neutrino mass of 0.05eV. We assume a fiducial value of $\tau = 0.1$ for the optical depth to electron scattering during reionization, and a helium mass fraction from big bang nucleosynthesis of $Y_{\rm He} = 0.24$. In a lower

redshift example we also leave the dark energy equation of state as a free parameter with a fiducial value of $w = -1$.

4.5 Results

We present the results of our Fisher matrix calculations in Tables 4.1-4.7. We consider several different sets of assumptions regarding the effects of the ionizing background, which as explained above, may introduce a weakly scale dependent bias. In principle this could produce degeneracies which would weaken constraints on cosmological parameters. First we present the case where the scale dependence of the bias is insignificant compared with the precision of the power spectrum measurements. Then we assume that the effect is large enough to require using a model with additional parameters to accurately fit the data. We also discuss a very pessimistic scenario where the form of the bias is completely unknown.

Table 4.1

		Ω_Λ	$\Omega_m h^2$	$\Omega_b h^2$	n_s	$A_s^2 \times 10^{10}$	α	$\Omega_\nu h^2$	τ	Y_{He}
Fiducial Values		0.7	0.147	0.023	0.95	25.0	0.0	0.00054	0.10	0.24
MWA5k-Hemisphere	PESS	0.0041	0.0098	0.0024	0.03	–	0.012	0.0018	–	–
	OPT	0.0024	0.0041	0.001	0.014	–	0.0068	0.00095	–	–
	CVL	0.00059	0.00025	0.000074	0.003	–	0.0013	0.0003	–	–
MWA5k-3 Fields	PESS	0.0095	0.023	0.0056	0.07	–	0.029	0.0042	–	–
	OPT	0.0055	0.0096	0.0023	0.034	–	0.016	0.0022	–	–
	CVL	0.0014	0.00059	0.00017	0.007	–	0.003	0.00071	–	–
FFTT		0.00076	0.00032	0.000087	0.0034	–	0.0016	0.00032	–	–
Planck		0.038	0.0041	0.00024	0.0094	0.25	0.007	0.0039	0.0046	0.014
+MWA5k-Hemisphere		0.0023	0.00044	0.00013	0.0037	0.21	0.0028	0.00041	0.004	0.0057
+MWA5k-3 Fields		0.0053	0.00074	0.00017	0.0056	0.22	0.004	0.00077	0.0041	0.0082
+FFTT		0.00076	0.00022	0.000076	0.0027	0.2	0.0013	0.00026	0.004	0.0043

Table 4.1:: Constant Bias: 1σ Errors on cosmological parameters with surveys centered at $z = 3.5$. OPT refers to an antenna temperature of 30K, PESS 100K, and CVL to the cosmic variance limited case. OPT and PESS correspond to what may be possible by the time these experiments will be built and what is achievable today.

Table 4.2

		Ω_Λ	$\Omega_{\rm m}h^2$	$\Omega_{\rm b}h^2$	$n_{\rm s}$	$A_{\rm s}^2 \times 10^{10}$	α	$\Omega_\nu h^2$	τ	$Y_{\rm He}$
Fiducial Values		0.7	0.147	0.023	0.95	25.0	0.0	0.00054	0.10	0.24
MWA5k-Hemisphere	PESS	0.0033	0.016	0.004	0.051	–	0.019	0.0027	–	–
	OPT	0.0023	0.011	0.0027	0.036	–	0.014	0.002	–	–
	CVL	0.0018	0.0085	0.0021	0.029	–	0.011	0.0016	–	–
MWA5k-3 Fields	PESS	0.0077	0.038	0.0093	0.12	–	0.044	0.0063	–	–
	OPT	0.0054	0.026	0.0063	0.084	–	0.032	0.0046	–	–
	CVL	0.0042	0.02	0.0048	0.068	–	0.026	0.0038	–	–
Planck		0.038	0.0041	0.00024	0.0094	0.25	0.007	0.0039	0.0046	0.014
+MWA5k-Hemisphere		0.0021	0.00042	0.00014	0.0042	0.22	0.0033	0.00041	0.0041	0.0065
+MWA5k-3 Fields		0.0047	0.00068	0.00018	0.0064	0.22	0.0048	0.00075	0.0041	0.0097

Table 4.2:: Constant Bias: 1σ Errors on cosmological parameters with surveys centered at $z = 1.5$. OPT refers to an antenna temperature of 30K, PESS 100K, and CVL to the cosmic variance limited case. OPT and PESS correspond to what may be possible by the time these experiments will be built and what is achievable today.

Table 4.3

		Ω_Λ	$\Omega_{\rm m}h^2$	$\Omega_{\rm b}h^2$	$n_{\rm s}$	$A_{\rm s}^2$	α	$\Omega_\nu h^2$	τ	$Y_{\rm He}$
MWA5k-Hemisphere	$z = 3.5$	0.061	0.11	0.54	0.39	0.84	0.4	0.11	0.87	0.41
MWA5k-3 Fields	$z = 3.5$	0.14	0.18	0.71	0.6	0.88	0.57	0.2	0.89	0.59
FFTT	$z = 3.5$	0.02	0.054	0.32	0.29	0.8	0.19	0.067	0.87	0.31
MWA5k-Hemisphere	$z = 1.5$	0.055	0.1	0.58	0.45	0.88	0.47	0.11	0.89	0.46
MWA5k-3 Fields	$z = 1.5$	0.12	0.17	0.75	0.68	0.88	0.69	0.19	0.89	0.69

Table 4.3:: Ratio of 1σ Errors for surveys combined with Planck to Errors from Planck alone.

Table 4.4

		Ω_Λ	$\Omega_m h^2$	$\Omega_b h^2$	n_s	$A_s^2 \times 10^{10}$	α	$\Omega_\nu h^2$	w	τ	Y_{He}
Fiducial Values		0.7	0.147	0.023	0.95	25.0	0.0	0.00054	-1.0	0.10	0.24
MWA5k-Hemisphere	PESS	0.0052	0.017	0.004	0.051	–	0.019	0.003	0.047	–	–
	OPT	0.0047	0.012	0.0027	0.036	–	0.014	0.0022	0.039	–	–
	CVL	0.0046	0.0088	0.0021	0.029	–	0.012	0.0018	0.036	–	–
MWA5k-3 Fields	PESS	0.012	0.039	0.0094	0.12	–	0.045	0.0069	0.11	–	–
	OPT	0.011	0.027	0.0064	0.084	–	0.033	0.0051	0.092	–	–
	CVL	0.011	0.02	0.0048	0.068	–	0.027	0.0043	0.083	–	–
Planck		0.096	0.0061	0.00024	0.0094	0.27	0.0071	0.0059	0.16	0.0051	0.015
+MWA5k-Hemisphere		0.0038	0.00056	0.00014	0.0042	0.22	0.0033	0.00049	0.023	0.0041	0.0065
+MWA5k-3 Fields		0.0082	0.00097	0.00018	0.0064	0.22	0.0048	0.0009	0.045	0.0041	0.0097

Table 4.4:: Constant Bias: 1σ Errors on cosmological parameters with surveys centered at $z = 1.5$ with w as a free parameter. OPT refers to an antenna temperature of 30K, PESS 100K, and CVL to the cosmic variance limited case. OPT and PESS correspond to what may be possible by the time these experiments will be built and what is achievable today.

Table 4.5

		Ω_Λ	$\Omega_m h^2$	$\Omega_b h^2$	n_s	$A_s^2 \times 10^{10}$	α	$\Omega_\nu h^2$	τ	Y_{He}
Fiducial Values		0.7	0.147	0.023	0.95	25.0	0.0	0.00054	0.10	0.24
MWA5k-Hemisphere	PESS	0.0043	0.011	0.0027	0.047	–	0.028	0.002	–	–
	OPT	0.0025	0.0046	0.0011	0.028	–	0.017	0.001	–	–
	CVL	0.00061	0.00026	0.000077	0.007	–	0.0031	0.00033	–	–
MWA5k-3 Fields	PESS	0.01	0.026	0.0062	0.11	–	0.066	0.0047	–	–
	OPT	0.0058	0.011	0.0026	0.065	–	0.04	0.0024	–	–
	CVL	0.0014	0.0006	0.00018	0.016	–	0.0072	0.00078	–	–
FFTT		0.00079	0.00033	0.000089	0.0085	–	0.0041	0.00035	–	–
Planck		0.038	0.0041	0.00024	0.0094	0.25	0.007	0.0039	0.0046	0.014
+MWA5k-Hemisphere		0.0024	0.00052	0.00013	0.0042	0.22	0.0032	0.00051	0.0041	0.007
+MWA5k-3 Fields		0.0055	0.00078	0.00017	0.0063	0.22	0.0048	0.00094	0.0041	0.01
+FFTT		0.00079	0.00025	0.000078	0.0034	0.21	0.0017	0.00029	0.004	0.0052

Table 4.5:: Fit to Scale Dependent Bias: 1σ Errors on cosmological parameters with surveys centered at $z = 3.5$. OPT refers to an antenna temperature of 30K, PESS 100K, and CVL to the cosmic variance limited case. OPT and PESS correspond to what may be possible by the time these experiments will be built and what is achievable today.

Table 4.6

		Ω_Λ	$\Omega_m h^2$	$\Omega_b h^2$	n_s	$A_s^2 \times 10^{10}$	α	$\Omega_\nu h^2$	τ	Y_{He}
Fiducial Values		0.7	0.147	0.023	0.95	25.0	0.0	0.00054	0.10	0.24
MWA5k-Hemisphere	PESS	0.0034	0.019	0.0047	0.067	–	0.034	0.0032	–	–
	OPT	0.0024	0.013	0.0031	0.048	–	0.025	0.0023	–	–
	CVL	0.0019	0.0095	0.0023	0.039	–	0.02	0.0019	–	–
MWA5k-3 Fields	PESS	0.008	0.045	0.011	0.16	–	0.08	0.0076	–	–
	OPT	0.0056	0.03	0.0072	0.11	–	0.058	0.0054	–	–
	CVL	0.0043	0.022	0.0053	0.09	–	0.046	0.0044	–	–
Planck		0.038	0.0041	0.00024	0.0094	0.25	0.007	0.0039	0.0046	0.014
+MWA5k-Hemisphere		0.0021	0.00049	0.00014	0.0045	0.22	0.0037	0.00053	0.0041	0.0073
+MWA5k-3 Fields		0.0048	0.00071	0.00018	0.0069	0.22	0.0052	0.00092	0.0042	0.011

Table 4.6:: Fit to Scale Dependent Bias: 1σ Errors on cosmological parameters with surveys centered at $z = 1.5$. OPT refers to an antenna temperature of 30K, PESS 100K, and CVL to the cosmic variance limited case. OPT and PESS correspond to what may be possible by the time these experiments will be built and what is achievable today.

Table 4.7

	Ω_Λ	$\Omega_{\rm m}h^2$	$\Omega_{\rm b}h^2$	$n_{\rm s}$	$A_{\rm s}^2 \times 10^{10}$	α	$\Omega_\nu h^2$
Fiducial Values	0.7	0.147	0.023	0.95	25.0	0.0	0.00054
constant bias	0.00076	0.00032	0.000087	0.0034	–	0.0016	0.00032
n=0	0.00079	0.00033	0.000089	0.0085	–	0.0041	0.00035
n=1	0.00084	0.00033	0.00009	0.011	–	0.0071	0.00036
n=2	0.00092	0.00035	0.000093	0.016	–	0.014	0.00036
n=3	0.00093	0.00037	0.000097	0.017	–	0.015	0.00037
n=4	0.00093	0.00038	0.0001	0.017	–	0.015	0.00037

Table 4.7:: Polynomial Corrections to Bias: 1σ Errors on cosmological parameters for FFTT centered around $z = 3.5$. Effects of fitting small polynomial corrections to the scale dependent bias. Here n is the degree of the polynomial marginalized over. The case with n=0 corresponds to the value from Table4.5.

We calculate constraints for both optimistic and pessimistic antenna temperature, which are 30K and 100K respectively. We also show results for a cosmic variance limited version of each survey where the detector noise is assumed to make no contribution. This case represents the best conditions imaginable for constraining cosmological parameters given the finite volume of space that is observed. As it turns out, an FFTT is nearly cosmic variance limited at the redshifts of interest here. In this case, we only show results for the optimistic antenna temperature case.

We consider a flat ΛCDM cosmology except for one case centered around $z = 1.5$ where we leave w as a free parameter.

4.5.1 Constant Bias

We begin with the case where the ionizing background does not introduce any significant modulation to the power spectrum. Thus, the bias, $B(\mathbf{k}) = \bar{b}$ can be taken as a constant in each redshift bin. Note that the value of the bias is different in each redshift bin, by constant we are referring to its dependence on scale. This is the most optimistic model one could hope for. Here we assume that the shot noise, neutral fraction and the bias in each redshift bin are unknown. Each is marginalized over as a free parameter in the Fisher matrix. We use Eqs. (4.3) and (4.4) to determine the fiducial values of the bias. The shot noise is determined from the Press-Schechter mass function of dark matter halos modified to include non-spherical collapse. The fiducial value of the neutral fraction is set to $x_{\rm HI} = 0.02$. The results are presented in Tables 4.1-4.4.

4.5.2 Scale Dependent Bias

We consider the case where the fluctuations of the 21cm power spectrum due to the ionizing background are large enough to require fitting additional nuisance parameters. We do not claim to derive the exact form of the modulation, instead we assume an idealized form and fit, and then see how cosmological constraints are degraded as more flexibility is introduced. As discussed above the scale dependent bias, $B(\mathbf{k})$, is the product of the average galaxy bias, $\bar{b}$ and $(1 - K(\mathbf{k}))$. In Wyithe & Loeb (2009) , $K(\mathbf{k})$ is calculated for the case where all photons travel the same distance. Here we consider the more realistic case of a constant mean-free-path. In this case, as calculated in Section 4.8, the modulation takes the form $K(\mathbf{k}) = K_0 \arctan(k\lambda_{\rm mfp})/\lambda_{\rm mfp}k$. We use the following approximation (given here in proper distance, but appearing in comoving distance in $K(\mathbf{k})$) for the fiducial values of the mean-free-path: $\lambda_{\rm mfp} = 85\,((1+z)/4)^{-4}\,$Mpc Faucher-Giguère et al. (2008). As before, in our Fisher matrix calculations we marginalize over shot noise, neutral fraction and average bias in each redshift bin. Additionally, we marginalize over K_0 and $\lambda_{\rm mfp}$ in each redshift bin. Our results are shown in Tables 4.5-4.6.

To see how constraints are affected as we increase the flexibility of the fit, we consider a case with small corrections to the form used above. Here we assume that the modulation is of the form

$$K(\mathbf{k}) = K_0 \arctan(k\lambda_{\rm mfp})/\lambda_{\rm mfp}k + c_1 k + c_2 k^2 + c_3 k^3 ... \tag{4.12}$$

where the c_n's are set to fiducial values of zero and marginalized over in each redshift bin. Aside from marginalizing over these new parameters, the Fisher matrix calculation is done the same as described above.

Table 4.7 shows the results for FFTT for marginalizing over all of the c_n's up to degree n. This illustrates how parameter constraints will be degraded as there is more flexibility in the fit for $K(\mathbf{k})$. We find that most cosmological parameters are not degenerate with scale dependent changes to the bias. However, the spectral index of the primordial power spectrum and its running are degraded significantly. This is because a change in these parameters smoothly modifies the 21cm power spectrum as a function of k, which mimics changes due to scale dependent bias parameters. A change in other parameters alters features in the power spectrum that can be distinguished from the scale dependent bias. For example, one might expect $\Omega_\nu h^2$ to be strongly degenerate as well, since neutrinos change the power spectrum in a smooth way. However, with our choice of cosmological parameters, we hold $\Omega_m h^2$ constant when taking derivatives of $\Omega_\nu h^2$. This means that changing the energy density of neutrinos also changes the energy density of cold dark matter. The associated change in the cold dark matter component alters features in the power spectrum which break the degeneracy with the scale dependent bias.

Note that while the above fit gives a range of how much fitting the scale dependent bias could weaken cosmological constraints, future work will have to determine the exact form of the fit which should be used. This will require detailed numerical simulations.

We have also considered the extremely pessimistic case where the form of the scale dependent bias is completely unknown. It has been found that it may be possible to isolate the part of the power spectrum containing only cosmological information by exploiting the angular dependence of the power spectrum. We use the PESS ionization power spectrum model described in (Mao et al. 2008) to calculate Fisher matrices. This isolates the term in the 21cm power spectrum which does not depend on the bias. We

find that even FFTT cannot constrain cosmological effectively and does not improve constraints from Planck significantly. This is probably overly pessimistic since the changes to the bias from the ionizing background are expected to be small, but it shows the importance of understanding the form of the bias.

4.5.3 Other Factors

There are several other factors that affect the constraints attainable with post-reionization 21cm surveys. We investigate how these factors change our constraints in the case of a constant bias. In Figure 4.2, we have plotted the dependence of the 1σ uncertainty on the bandwidth over which foregrounds are removed. Larger values for the bandwidth allow measurement of smaller k values which are otherwise not accessible. Overall, the sensitivity to the bandwidth variation is relatively modest.

In Figure 4.3, we show how the constraints vary for different choices of $k_{\rm max}$, the maximum wavenumber being used. We show how the parameter uncertainties change if we impose the cutoff at different levels of discrepancy between the non-linear and linear power spectra. As $k_{\rm max}$ is lowered errors on parameters are substantially increased. For a discrepancy of 0.1 and 0.05, $k_{\rm max}$ ranges from $0.68 - 0.16{\rm Mpc}^{-1}$ and $0.28 - 0.12{\rm Mpc}^{-1}$ respectively, see Figure 4.1. For a discrepancy of 0.01 $k_{\rm max} \approx 0.06{\rm Mpc}^{-1}$ for each redshift bin.

In Figure 4.4, we show how the constraints depend on $M_{\rm min}$, the minimum halo mass above which significant amounts of neutral hydrogen may assemble. A high value of $M_{\rm min}$ increases the shot noise and degrades the constraints. We find that the shot noise only affects the results significantly above $\sim 10^{12} M_{\odot}$, which is unrealistic since

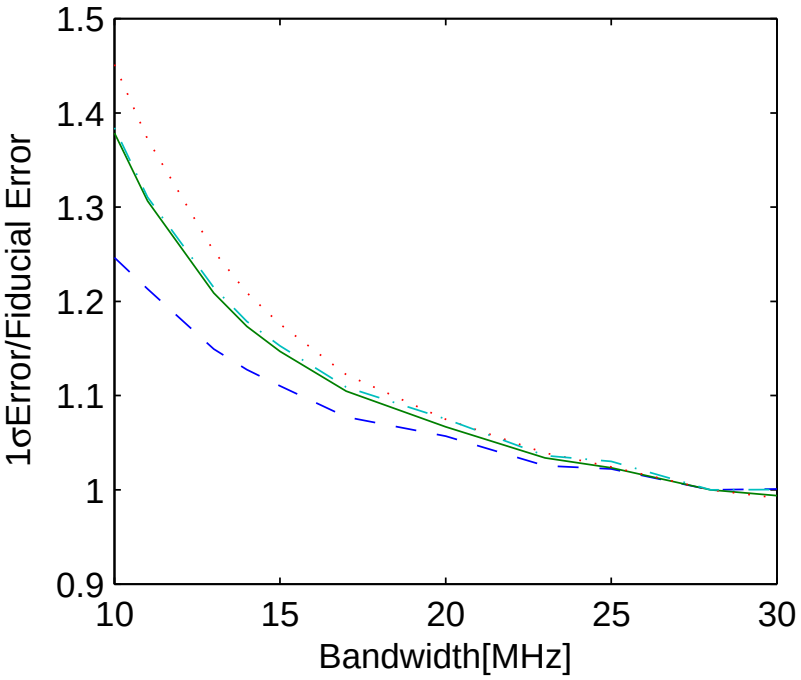

Figure 4.2.—: Sensitivity of the relative 1σ error bar to the bandwidth over which foregrounds can be removed for FFTT. Errors have been normalized such that they equal unity for the assumptions in Table 4.1. The dashed line gives the error for Ω_Λ, the dotted line for $\Omega_\nu h^2$, the solid line for $n_{\rm s}$ and the dot-dash line for α.

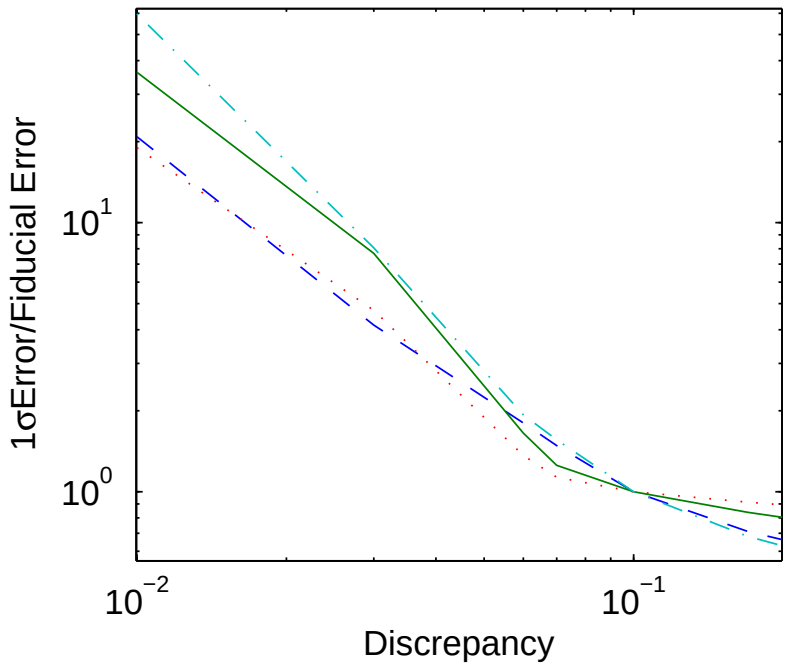

Figure 4.3.—: Sensitivity of the relative 1σ error bar to the maximal wavenumber $k_{\rm max}$ for FFTT. Errors have been normalized such that they equal one for the assumptions in Table 4.1. The dashed line gives the error for Ω_Λ, the dotted line for $\Omega_\nu h^2$, the solid line for $n_{\rm s}$ and the dot-dash line for α.

hydrogen is found in lower mass galaxies in the local Universe (Davies et al. 2001).

4.6 Discussion

The above results are very promising. We find that using the angular dependence of the power spectrum to isolate the term which only depends on cosmology cannot effectively constrain cosmological parameters. For this reason, it is crucial that the modulation of the 21cm power spectrum from the ionizing background is modeled reliably.

Our results show approximately how constraints would be degraded if a fit were to be necessary. Table 4.7 illustrates how more freedom in the fit affects cosmological constraints. We find that the only parameters which are strongly degenerate with the new fitting parameters are n_s and α, the spectral index and the running of the primordial power spectrum. The 1σ errors on these parameters could increase by an order of magnitude. The other 1σ cosmological parameter errors are increased by roughly 20% or less.

For comparison, the constraints from 21cm surveys that focus on the EoR (Mao et al. 2008) vary considerably under different ionization power spectrum model assumptions. The robustness of our post-reionization constraints is mainly due to the fact that we do not have to consider the ionization power spectrum, only small scale dependent changes to the bias.

Our results also depend strongly on the maximum wavenumber of the power spectrum which can be used to reliably measure cosmological parameters, $k_{\rm max}$. It will be desirable for theoretical predictions of the matter power spectrum, presumably

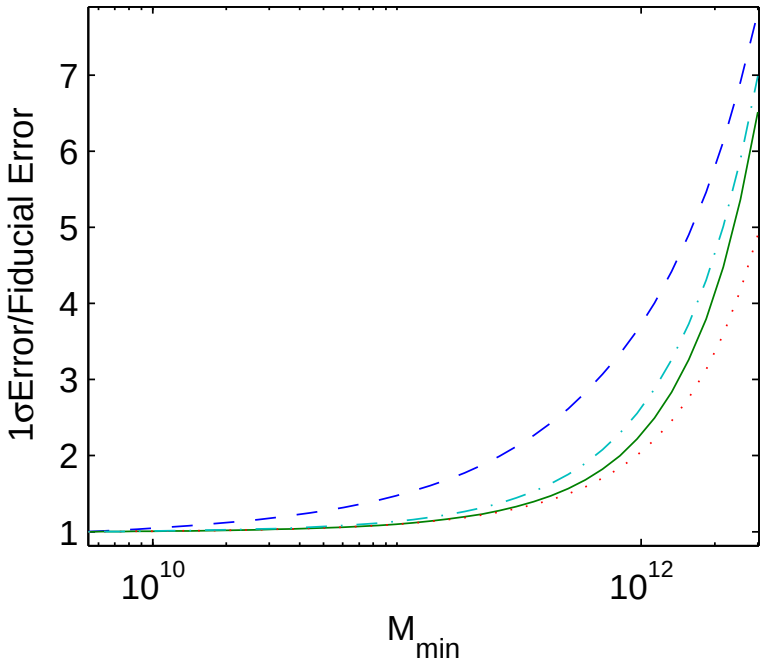

Figure 4.4.—: Dependence of constraints on M_{min} (in units of solar mass) for FFTT. Errors have been normalized such that they equal one for the assumptions in Table4.1. The dashed line gives the error for Ω_Λ, the dotted line for $\Omega_\nu h^2$, the solid line for $n_{\rm s}$ and the dot-dash line for α.

from N-body simulations, to be computed to a fraction of a percent for k_{max} values corresponding to a 5% descrepancy in the linear and non-linear power spectra shown in Figure 4.1. If the matter power spectrum can not be computed to this accuracy, the value of $k_{\rm max}$ may be the limiting factor for measuring cosmological parameters with experiments similar to those described in this paper.

The noise in the interferometers is lower at lower redshift due to the redshift scaling of the galactic synchrotron emission. This advantage is offset by the fact that at higher redshifts the neutral fraction is higher and the observed power spectrum stays linear up to a higher $k_{\rm max}$ value. The FFTT and the MWA5000 at $z = 1.5$ are nearly cosmic variance limited. These experiments would be close to capturing all the information available from the power spectrum available to us on linear scales at the relevant redshifts. The MWA5000 with optimistic antenna temperature centered at $z = 3.5$ gives errors roughly five times larger than the cosmic variance limited case.

Current cosmological information sets the upper limit on neutrino mass to ~ 0.62 eV Goobar et al. (2006); Seljak et al. (2006). For FFTT with a constant bias, we find a 1σ error corresponding to 0.030eV. As expected Loeb & Wyithe (2008), this is clearly much better than existing constraints and is sufficiently small to probe the neutrino mass differences implied by neutrino oscillations.

It is also interesting to compare how well these surveys constrain cosmology with respect to other future probes. The FFTT survey will perform much better than the Planck satellite for almost all of the parameters under consideration. When combined with Planck, essentially all of the constraints are improved. In Table 4.3 we explicitly show how the constraint on each parameter from Planck would improve if combined

with post-reionization 21cm surveys. The most improved parameters are Ω_Λ, $\Omega_\mathrm{m}h^2$, and $\Omega_\nu h^2$, which for FFTT are 2.0%, 5.4%, and 6.7% of the errors from Planck alone.

Since most of the remaining neutral hydrogen after the EoR is found in DLAs hosted by galaxies, we expect our results to be similar to galaxy redshift surveys over similar redshift ranges. In Pritchard & Pierpaoli (2008) an all sky galaxy survey centered around $z = 1$, termed G3, is considered. We find the cosmological constraints they calculate to be very similar to those in our MWA5000 case with a constant bias centered around $z = 1.5$. They also consider a Lyman break survey centered around $z = 3$, which they term G2. This survey contains roughly 1% of the volume included in our MWA5000-hemisphere and FFTT cases. Since the error on the power spectrum scales as the square root of the volume of a survey, this should cause parameter errors in G2 to be roughly an order of magnitude larger. We find that this falls roughly into the range we calculate above for the constant bias MWA5000 case centered around $z = 3.5$. Note that if the degeneracies due to the UV background discussed above are present, galaxy surveys may do significantly better than 21cm at measuring the n_s and α, the spectral index of the primordial power spectrum and its running.

In the case where we allow w to vary as a free parameter we find the constraints on most parameters essentially unchanged. The main exception is Ω_Λ, where we find that our constraints are increased by roughly a factor of two. The constraints achievable for w are interesting, about 3.9% if the whole hemisphere is observed, and 9.2% with only three fields of view.

4.7 Conclusions

A 21cm survey after reionization provides a promising probe of cosmology and fundamental physics (Loeb & Wyithe 2008). We find the simple form of the 21cm power spectrum after reionization provides less uncertainty in forecasting constraints than 21cm during the EoR. However, we find that errors on estimates of the spectral index and the running of the primordial power spectrum could be increased by an order of magnitude if the ionizing background introduces scale dependent effects into the post reionization 21cm power spectrum.

Aside from its greater simplicity, the measurement sensitivity after reionization is improved over EoR surveys due to lower foreground brightness temperature, a bias that is greater than unity, and a larger growth factor of density perturbations. These advantages are somewhat offset by the fact that there is less neutral hydrogen after reionization.

The constraints we derive are competitive with those from the EoR and for the FFTT are significantly better than next generation CMB experiments on their own. We find errors on Ω_Λ, $\Omega_{\rm m}h^2$, and $\Omega_\nu h^2$ to be improved the most, each lowering the errors from Planck alone by at least an order of magnitude for both FFTT and the survey similar in design to MWA5000.

4.8 Appendix: Modulation of 21cm PS from Ionizing Background

We derive the form of the modulation of the 21cm power spectrum due to the ionizing background in the case of a constant mean-free-path. The only difference in the derivation presented in Wyithe & Loeb (2009) is the form of the fluctuations of the ionizing flux $\delta_J(\mathbf{x})$. We convolve the real-space density field with a filter function to account for the effects of a finite mean-free-path and the inverse squared dependence of ionizing flux. The fluctuation in flux is given by

$$\delta_J(\mathbf{x}) \propto \int d\mathbf{x}' G(\mathbf{x},\mathbf{x}')\delta(\mathbf{x}'). \tag{4.13}$$

We assume a mean-free-path of ionizing photons which is independent of position such that,

$$G(\mathbf{x},\mathbf{x}') \propto \frac{\exp(-|\mathbf{x}'-\mathbf{x}|/\lambda_{\rm mfp})}{|\mathbf{x}'-\mathbf{x}|^2}, \tag{4.14}$$

where $\lambda_{\rm mfp}$ is the mean free path of ionizing photons. The convolution theorem gives

$$\delta_J(\mathbf{k}) \propto g(\mathbf{k})\delta_k, \tag{4.15}$$

where $g(\mathbf{k})$ and δ_k are the Fourier transforms of the filter function and the fluctuation in ionizing flux. We find that

$$g(\mathbf{k}) \propto \arctan(k\lambda_{\rm mfp})/k. \tag{4.16}$$

From the derivation presented in Wyithe & Loeb (2009), this implies that the power spectrum is given by Eqn. 4.2 with

$$K(k) = K_0 \arctan(k\lambda_{\rm mfp})/\lambda_{\rm mfp}k, \tag{4.17}$$

where K_0 is a constant of the order of 0.01 or smaller (Wyithe & Loeb 2009).

Acknowledgments

This work was supported in part by a NASA LA grant and by Harvard University funds. We thank Matt McQuinn and Jonathan Pritchard for useful discussions.

Chapter 5

Gauging the Contribution of X-ray Sources to Reionization Through the Kinetic Sunyaev-Zel'dovich Effect

E. Visbal & A. Loeb *Journal of Cosmology and Astroparticle Physics*, Issue 5, ID 007, 2012

Abstract

Measurements of the kinetic Sunyaev-Zel'dovich (kSZ) effect from instruments such as the South Pole Telescope (SPT) and the Atacama Cosmology Telescope (ACT) will soon put improved constraints on reionization. Popular models assume that UV photons alone are responsible for reionization of the intergalactic medium. We explore the effects of a significant contribution of X-rays to reionization on the kSZ signal. Because X-rays have

a large mean free path through the neutral intergalactic medium, they introduce partial ionization in between the sharp-edged bubbles created by UV photons. This smooth ionization component changes the power spectrum of the cosmic microwave background (CMB) temperature anisotropies. We quantify this effect by running semi-numerical simulations of reionization. We test a number of different models of reionization without X-rays that have varying physical parameters, but which are constrained to have similar total optical depths to electron scattering. These are then compared to models with varying levels of contribution to reionization from X-rays. We find that models with more than a 10% contribution from X-rays produce a significantly lower power spectrum of temperature anisotropies than all the UV-only models tested. The expected sensitivity of SPT and ACT may be insufficient to distinguish between our models, however, a non-detection of the kSZ signal from the epoch of reionization could result from the contribution of X-rays. It will be important for future missions with improved sensitivity to consider the impact of X-ray sources on reionization.

5.1 Introduction

The epoch of reionization (EoR) is an important milestone in the history of our universe (Loeb 2010). There has been much theoretical work in this area, but currently there are no definitive observational constraints on the morphology or duration of reionization. An important probe of this process is the small scale temperature fluctuations in the cosmic microwave background (CMB). In particular, secondary anisotropies are imprinted on top of the primordial CMB from the Doppler shift associated with CMB photons scattering off free electrons in between the observer and the surface of last scattering at

$z \approx 1100$. This is known as the kinetic Sunyaev-Zel'dovich (kSZ) effect. Because only ionized regions can contribute to this effect, the power spectrum of kSZ fluctuations is sensitive to details of the reionization history (McQuinn et al. 2005; Zahn et al. 2005; Iliev et al. 2007; Gruzinov & Hu 1998; Knox et al. 1998).

The most popular models of reionization assume that the UV photons from early stars drive the ionization of the intergalactic medium (IGM). Due to the short mean free path (MFP) of UV photons through the neutral IGM, the resulting topology of reionization is a two phase IGM consisting of ionized bubbles surrounded by regions of neutral gas (Barkana & Loeb 2001).

Another possibility is that X-ray photons make a significant contribution to reionization (e.g. Ricotti & Ostriker 2004; Haiman et al. 2000a; Venkatesan et al. 2001; Warszawski et al. 2009; Volonteri & Gnedin 2009). These X-rays could originate from accretion onto massive black holes in galactic nuclei, X-ray binaries, or inverse Compton scattering in supernova remnants (Furlanetto et al. 2006a). Because the MFP of X-rays through the IGM is much longer than UV photons this will result in a more uniform background of ionizing photons. Thus, a significant contribution of X-rays can qualitatively change reionization by creating a partially ionized IGM in between the bubbles produced by UV photons.

In this paper we use semi-numerical simulations to gauge the imprint of X-ray sources during reionization on the kSZ signal. Because of the smooth ionization caused by X-rays, the so called "patchy" component of the kSZ power spectrum can be substantially reduced. We find that models with more than a 10% contribution from X-rays produce a significantly lower power spectrum of temperature anisotropies than all

the UV-only models tested.

The paper is structured as follows. In Section 5.2, we describe our method of estimating the kSZ signal including a description of our semi-numerical simulations of reionization with and without a contribution from X-rays. In Section 5.3, we report our results, which include changes in the CMB power spectrum due to the contribution of X-ray sources to reionization. In Section 5.4 we summarize our main conclusions. Throughout, we assume a ΛCDM cosmology with $\Omega_\Lambda = 0.73$, $\Omega_m = 0.27$, $\Omega_b = 0.0456$, $h = 0.7$, and $\sigma_8 = 0.81$ Komatsu et al. (2011).

5.2 Method

5.2.1 The Kinetic SZ Effect

The kSZ effect is the contribution to fluctuations in the CMB temperature associated with the Doppler shift of CMB photons Thompson scattered off free electrons moving at some radial velocity relative to the observer. The kSZ temperature fluctuation in a particular direction is given by

$$\frac{\Delta T}{T} = \sigma_{\rm T} \int d\eta e^{-\tau(\eta)} a n_e v_{||}, \tag{5.1}$$

where $\sigma_{\rm T}$ is the Thomson cross section, $\tau(\eta)$ is the optical depth from the observer to the position corresponding to conformal time η, a is the cosmic scale factor, n_e is the number density of free electrons, and $v_{||}$ is the component of the velocity along the line of sight.

We wish to calculate the impact on the kSZ effect from an X-ray contribution to reionization using semi-numerical simulations of the EoR. These simulations will examine

varying levels of X-ray contribution to reionization. We generate a number of simulation cubes that each span a solid angle of one square degree on the sky (corresponding to a comoving length of $L \approx 150 - 200$ Mpc from $z = 6 - 20$) and have a resolution of 256^3 separate volume elements. In each 3D element of the simulation we calculate the matter over-density, velocity, and ionization fraction. Cubes are produced at appropriate cosmic times and stacked along the line of sight to give continuous coverage from a redshift of $z = 6$ to $z = 20$, corresponding to the EoR. We then perform the integral in Eq. (5.1) along each line of sight to produce a 2D map of CMB temperature fluctuations.

We compute the density and velocity fields of our simulations using the 21cmFAST software package (Mesinger et al. 2011a). Non-linearities are included using leading order perturbation theory (Zel'dovich approximation). We expect this to be a reasonable approximation, as the power spectra of the density field using this approach agree well with that from detailed hydrodynamic simulations at the redshifts and scales relevant for our calculations (Mesinger et al. 2011a). We generate our ionization fields with the model described below. Note that we do not produce data cubes at redshifts below $z = 6$. The kSZ fluctuations from these redshifts will be independent of reionization history and we incorporate their effect analytically.

5.2.2 Reionization Model

To simulate the reionization history we use a semi-numerical approach similar to that described in Warszawski et al. (2009). The basic assumption in our prescription is that there is a fixed number of hydrogen ionizations, $N_{\rm ion}$, in the IGM for each baryon which is incorporated into galaxies. From extended Press-Schechter theory it is possible to

calculate the rate at which matter will collapse into dark matter halos (Bond et al. 1991). In this way one can calculate the ionized fraction in a region of a given size and density analytically. For the case without X-rays where all ionizing photons are assumed to be UV, the evolution of the ionization in a spherical region of comoving radius R with over-density δ relative to the cosmic mean is given by Wyithe & Loeb (2007a)

$$\frac{dQ_{R,\delta}}{dt} = \frac{N_{\rm ion}}{0.76}\left(Q_{R,\delta}\frac{dF(M_{\rm ion})}{dt} + (1-Q_{R,\delta})\frac{dF(M_{\rm min})}{dt}\right) - B, \tag{5.2}$$

where the 0.76 accounts for the cosmic mass fraction of hydrogen, $Q_{R,\delta}$ is the mass averaged ionized fraction of hydrogen, and $F(M)$ (which depends implicitly on δ and R) is the fraction of mass which has collapsed into dark matter halos above mass M,

$$F(M) = {\rm erfc}\left(\frac{\delta_c(z) - \delta(z=0)}{\sqrt{2(\sigma(M)^2 - \sigma(M_R)^2)}}\right), \tag{5.3}$$

where $\delta_c = 1.686/D(z)$ is the threshold for spherical collapse at $z \gg 1$ extrapolated to redshift zero with linear theory, $D(z)$ is the linear growth factor of density fluctuations, $\delta(z=0)$ is the linear over-density of the region at the current time, and the σ's are the root mean squared density fluctuations on scales corresponding to mass M and radius R today. The minimum mass of dark matter halos that can host galaxies is denoted by $M_{\rm min}$ in the neutral IGM and by $M_{\rm ion}$ in the ionized and photo-heated IGM. We parameterize this mass in terms of the virial temperature which for $z \gg 1$ is given by

$$T_{\rm vir} = 10^4\left(\frac{M}{10^8 M_\odot}\right)^{2/3}\left(\frac{1+z}{10}\right){\rm K}. \tag{5.4}$$

The recombination rate is given by

$$B = \alpha_{\rm B} C n_{\rm H}^0 (1+z)^3 (1+\delta) Q_{R,\delta}, \tag{5.5}$$

where $\alpha_{\rm B} = 2.6\times10^{-13}{\rm cm}^3/{\rm s}$ is the case B recombination coefficient for $T = 10^4$ K (Osterbrock & Ferland 2006), $C = \langle n_e^2\rangle/\langle n_e\rangle^2$ is the clumpiness of the ionized gas in the IGM and $n_{\rm H}^0$ is the mean density of hydrogen gas today.

In order to produce the 3D simulation of the ionization fraction we smooth a random realization of the linear density field in our simulation in spheres of varying radius and solve Eq. (5.2) as a function of the size and over-density at each point. At this stage, regions for which $Q_{R,\delta} > 1$ are taken to be bubbles and the ionization fraction is set to one while other regions are taken to be completely neutral. Next, the equation is solved on the scale of each spatial pixel and then used to determine the ionization fraction in regions not encompassed by ionization bubbles.

We use a similar approach to calculate the ionization fraction when X-rays make a significant contribution to reionization. This approach has been adapted from Warszawski et al. (2009). The key simplifying assumption we make is that X-rays have a fixed comoving MFP and that X-ray photons uniformly ionize regions of that size. The comoving MFP of X-rays of energy E_X through a neutral medium is given by Madau et al. (2004); Furlanetto et al. (2006a),

$$\lambda \approx 180 \left(\frac{1+z}{15}\right)^{-2} \left(\frac{E_X}{1\mathrm{keV}}\right)^{3} \mathrm{Mpc}. \tag{5.6}$$

We assume a constant MFP of $\lambda = 20$ Mpc, but find that the measured angular power spectrum of temperature anisotropies is essentially unchanged if we set $\lambda = 50$ Mpc. UV photons have a very short MFP compared to the size of the spatial pixels in our simulation. Thus, when considering a region smaller than the MFP of X-rays one must consider the X-ray sources from a larger surrounding region with a radius equal to the X-ray MFP, λ, while the ionization from UV photons will only depend on the local over-density. We capture this behavior by solving a system of 6 coupled ordinary differential equations (ODEs) which compute the ionization history (including the relative amounts from X-rays versus UV photons) on various scales. As in the

UV-only case, we smooth the density field on all scales to identify ionized bubbles, but in addition simultaneously track the ionization history and production of X-ray photons from surrounding regions with radius equal to the X-ray MFP (λ). The system of 6 ODEs (adapted from Warszawski et al. 2009) is

$$\frac{dQ_R}{dt} = \frac{dQ_{R,UV}}{dt} + \frac{dQ_{R,X}}{dt} \tag{5.7}$$

$$\frac{dQ_\lambda}{dt} = \frac{dQ_{\lambda,UV}}{dt} + \frac{dQ_{\lambda,X}}{dt} \tag{5.8}$$

$$\frac{dQ_{R,UV}}{dt} = (1 - X_{\rm frac})\frac{N_{\rm ion}}{0.76}\left(Q_R\frac{dF(M_{\rm ion})}{dt} + (1 - Q_R)\frac{dF(M_{\rm min})}{dt}\right) - B_3 \tag{5.9}$$

$$\frac{dQ_{\lambda,UV}}{dt} = (1 - X_{\rm frac})\frac{N_{\rm ion}}{0.76}\left(Q_\lambda\frac{dF(M_{\rm ion})}{dt} + (1 - Q_\lambda)\frac{dF(M_{\rm min})}{dt}\right) - B_4 \tag{5.10}$$

$$\frac{dQ_{R,X}}{dt} = X_{\rm frac}\frac{N_{\rm ion}}{0.76}\left(Q_R\frac{dF(M_{\rm ion})}{dt} + (1 - Q_R)\frac{dF(M_{\rm min})}{dt}\right) - B_5 \quad \text{if} \quad R > \lambda \tag{5.11}$$

$$\frac{dQ_{R,X}}{dt} = X_{\rm frac}\frac{N_{\rm ion}}{0.76}\left(\frac{1+\delta_\lambda}{1+\delta_R}\right)\left(Q_\lambda\frac{dF(M_{\rm ion})}{dt} + (1 - Q_\lambda)\frac{dF(M_{\rm min})}{dt}\right) - B_5 \quad \text{if} \quad R < \lambda \tag{5.12}$$

$$\frac{dQ_{\lambda,X}}{dt} = X_{\rm frac}\frac{N_{\rm ion}}{0.76}\left(Q_\lambda\frac{dF(M_{\rm ion})}{dt} + (1 - Q_\lambda)\frac{dF(M_{\rm min})}{dt}\right) - B_6, \tag{5.13}$$

where Q_R and Q_λ are the mass averaged ionization fractions on scales of R and λ respectively. $Q_{R,UV}$ is the ionization on scale R due to UV photons and $Q_{R,X}$, $Q_{\lambda,X}$, and

$Q_{\lambda,UV}$ are the various ionization fractions from either X-rays or UV photons ionization on the two scales of interest. The fraction of hydrogen ionizations due to X-rays is denoted by $X_{\rm frac}$. Note that the time derivative of the collapsed fraction in each equation is evaluated on the same scale as the Q value it is multiplied with.

An X-ray photon contains more energy than required to ionize a hydrogen or helium atom in the IGM. The remaining energy contributes to additional secondary ionizations and heating (Shull & van Steenberg 1985; Venkatesan et al. 2001). In our model with an X-ray contribution to reionization $N_{\rm ion} \times X_{\rm frac}$ corresponds to the total number of primary and secondary ionizations caused by X-rays for each baryon which collapses into galaxies. For background ionization levels exceeding 10%, the number of secondary ionizations will be greatly reduced, with most of the energy heating the IGM instead. Though not included here, future work could incorporate this effect by multiplying the ionization terms in Eqs. (5.11-5.13) by a function which suppresses X-ray ionizations above $Q = 0.10$.

The various B_i terms are recombination rates. In the UV case, Eq. (5.5) was derived by assuming that all regions are either completely ionized or neutral. With a significant contribution from X-rays this will not be the case. We assume that X-rays uniformly ionize the IGM on scale λ and UV photons completely ionize bubbles in the IGM around their sources. In order to calculate the recombination terms we calculate the volume of the IGM which is uniformly ionized, $V_{\rm uniform}$, and the fraction in ionized bubbles, $V_{\rm bub}$. The uniform X-ray ionization also allows bubbles to grow larger than they would from the UV photons alone; we denote this additional "fringe" volume with $V_{\rm fringe}$. These add

up to the total volume of the spherical regions we consider, V, and are described by

$$V_{\rm bub}/V = Q_{UV} \tag{5.14}$$

$$V_{\rm fringe}/V = \frac{Q_{UV}Q_X}{1-Q_X} \tag{5.15}$$

$$V_{\rm uniform} = V - V_{\rm bub} - V_{\rm fringe}, \tag{5.16}$$

where either the UV or X-ray ionization must be evaluated on the relevant length scale. It follows that the recombination rate terms are given by

$$B_3 = \alpha_{\rm B} C n_{\rm H}^0 (1+z)^3 (1+\delta_R) \frac{V_{\rm bub}}{V}, \tag{5.17}$$

$$B_5 = \alpha_{\rm B} C n_{\rm H}^0 (1+z)^3 (1+\delta_R) \left(\frac{V_{\rm fringe}}{V} + Q_{R,X}^2 \frac{V_{\rm uniform}}{V} \right). \tag{5.18}$$

B_4 and B_6 are the same as B_3 and B_5 except that the appropriate values for δ_λ and the volumes corresponding to scale λ must be used. Note that this treatment of the recombination rates was not included in previous work. We do not include heating due to X-rays which could further suppress the formation of low mass galaxies. This would be straightforward to incorporate in the future (Warszawski et al. 2009).

We smooth our density field on all scales and if $Q_R > 1$ the region R is set to be completely ionized. After the entire cube has been searched on all relevant scales we solve Eqs. (5.7-5.13) on the scale of each spatial pixel to determine the ionization fraction outside of the completely ionized bubbles.

5.3 Results

In order to test the impact of X-ray contribution to reionization on the kSZ effect we produce several different simulations using the model above. The model parameters

which can be adjusted are $N_{\rm ion}$, C, $M_{\rm min}$, $M_{\rm ion}$, $X_{\rm frac}$, and λ. We produce several simulations with different parametrizations, but which have an optical depth to the surface of last scattering, τ, consistent with WMAP measurements ($\tau = 0.088 \pm 0.015$) (Komatsu et al. 2011). For simplicity, we ignore the residual ionization from cosmological recombination (prior to reionization). From these models we can evaluate the effect of a varying level of X-ray contribution to reionization. The values of the various parameters for each model are listed in Table 5.1. Due to the constraint on τ, our models have fairly similar global reionization histories. These are shown in Figure 5.1.

The main difference with X-rays is that their relatively long MFP would cause some smooth ionization fraction throughout the IGM in regions which are not inside bubbles. This is illustrated clearly in Figure 5.2. We plot the ionization fraction through a slice of our simulation at $z = 9$ for the "fiducial" and "50% X-ray" models. In both cases we have used the same underlying density field and the global mass weighted ionization fraction is roughly the same. There is a striking difference in the character of reionization between these two models. The UV-only case is dominated by completely ionized bubbles with surrounding neutral regions. The model with X-rays has smaller bubbles surrounded by a partially ionized IGM.

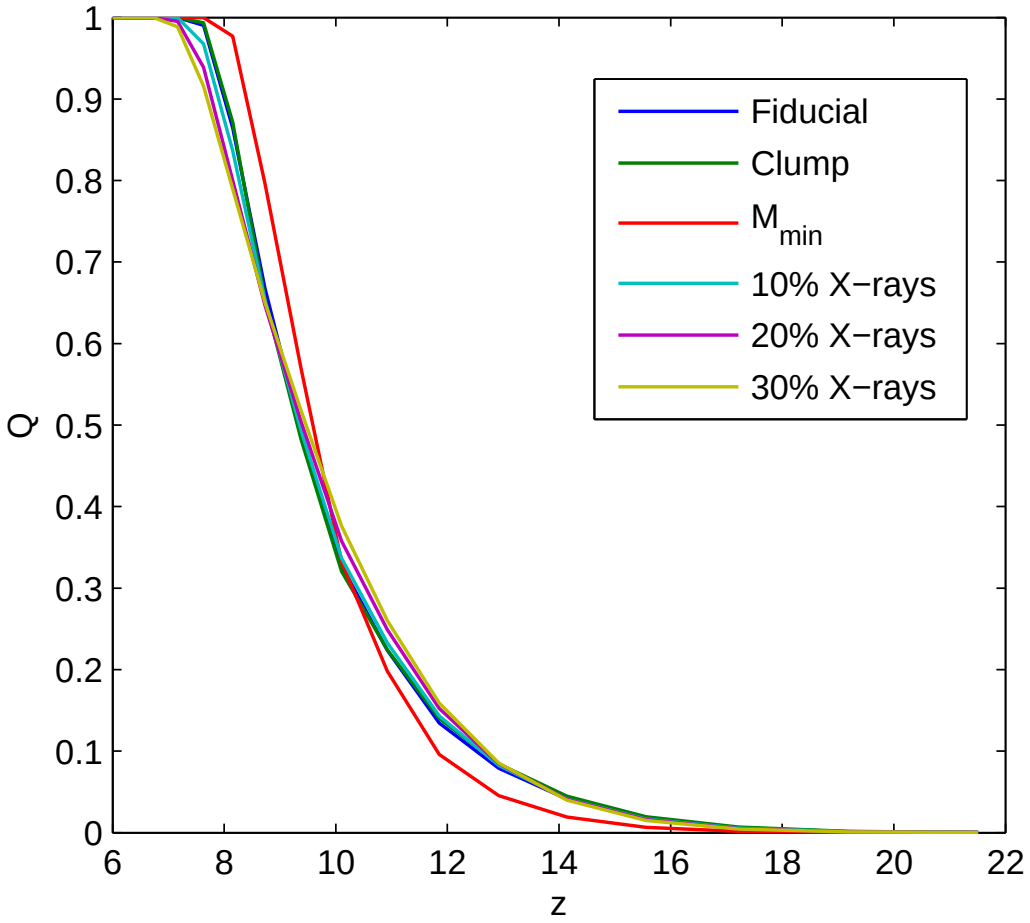

Figure 5.1.—: The mass weighted global ionization fraction as a function of redshift for the different reionization models.

Table 5.1

Model	$N_{\rm ion}$	C	$\rm T_{vir}(M_{min})$	$\rm T_{vir}(M_{ion})$	$X_{\rm frac}$	λ	τ
Fiducial	60	2	10^4K	10^5K	0	-	0.088
Clump	355	20	10^4K	10^5K	0	-	0.088
$M_{\rm min}$	115	2	5×10^4K	10^5K	0	-	0.088
10% X-ray	53	2	10^4K	10^5K	0.1	20 Mpc	0.088
30% X-ray	45	2	10^4K	10^5K	0.3	20 Mpc	0.088
50% X-ray	40	2	10^4K	10^5K	0.5	20 Mpc	0.088

Table 5.1:: Parameters for the different reionization models used. For the minimum masses of dark matter halos which host galaxies, the corresponding virial temperature (assumed to be constant) is listed instead of the mass (see Eq. (5.4) in the text).

Figure 5.2.—: The ionization fraction through a slice of our "fiducial" (top panel) and "50% X-ray" (bottom panel) model at $z = 9$. Note that the same underlying density field has been used for both. The slice corresponds to a $170 \times 170 \times 0.66\,\mathrm{Mpc}^3$ volume in the simulation. The color bar gives the mass weighted neutral fraction in each pixel.

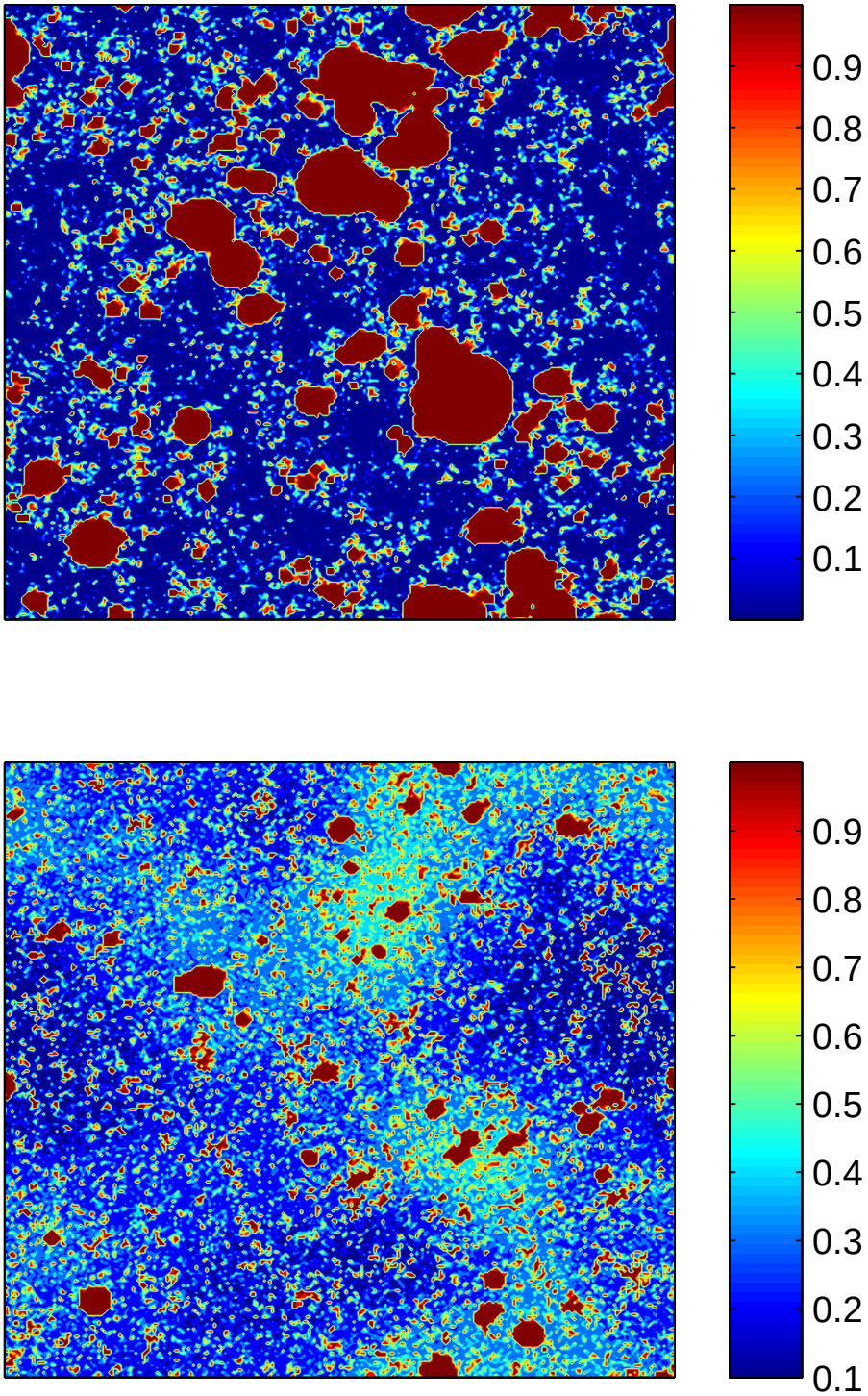

Figure 5.2.—: (Continued).

In order to quantify the change in the kSZ signal due to X-rays, we compute the angular power spectrum of CMB temperature fluctuations, C_l. We calculate the kSZ temperature fluctuations from the EoR ($z = 6 - 20$) by integrating Eq. (5.1) through our simulations. The resulting 2D temperature field is then Fourier transformed to compute the power spectrum. We include the kSZ signal from lower redshift by calculating the power spectrum analytically and adding it to the EoR result. This is necessary because at low redshifts non-linear effects become significant and they are not accurately captured with the density fields we use from 21cmFAST. We calculate the analytic power spectrum using the method described in McQuinn et al. (2005) (see their Eq. (4)). To account for the primordial temperature fluctuations, which dominate on large angular scales, we add the lensed C_l's calculated from CAMB[1]. We make the assumption that the thermal Sunyaev-Zel'dovich effect, with its distinctive spectral signature, will be removed completely.

All of the models tested were designed to have nearly identical optical depth due to electron scattering. Of course there will always be some uncertainty in value of this quantity. For example, Planck measurements will constrain τ to within ≈ 0.005 (The Planck Collaboration 2006). We find that this uncertainty should not strongly affect our results. As an example, for the "fiducial" model, we vary $N_{\rm ion}$ within the corresponding uncertainty in τ and find that the power spectrum never goes as low as the 10% X-ray model for the l values in Figure 5.3.

In addition to plotting the theoretical estimates, we show the error bars of SPT in Figure 5.4 (Ruhl et al. 2004). SPT will only be sensitive to the kSZ signal at $l \approx 3000$

[1]http://camb.info/

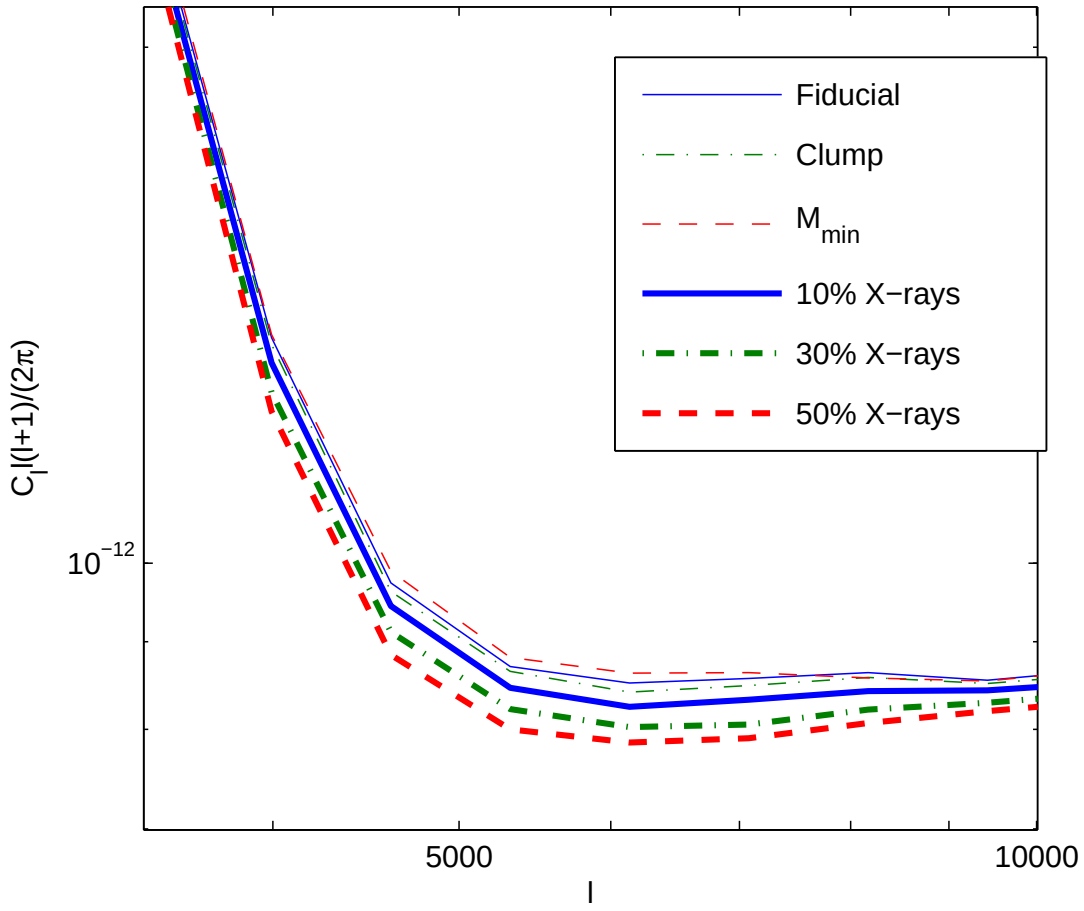

Figure 5.3.—: The angular power spectrum of temperature fluctuations for the different reionization models tested.

due to the high amplitude of the primordial temperature fluctuations at lower l and dusty star-forming galaxies at higher l. Detailed estimates by the SPT team project an ultimate sensitivity of $\Delta\left(C_l l(1+l)/(2\pi)\right) = 1\mu\mathrm{K}^2/\bar{\mathrm{T}}^2_{\mathrm{CMB}}$. ACT (Kosowsky 2003) will be a couple times less sensitive (Matthew McQuinn, private communication 2011), (Mesinger et al. 2011c; Reichardt et al. 2011). In Table 5.2 we show the contribution to the kSZ power spectrum from the EoR ($z = 6 - 20$) at $l = 3000$. If X-rays contribute significantly to reionization this power may be smaller than the projected uncertainty of SPT and ACT, resulting in a non-detection of a signal from reionization.

5.4 Discussion and Conclusions

We have calculated the effect of an X-ray contribution to reionization on the fluctuations in the CMB from the kSZ effect. This was accomplished with semi-numerical simulations of reionization. For the case with no X-ray contribution, we tested how changes in the physical parameters, including the number of ionizing photons produced, the clumpiness of the IGM and the minimum mass of dark matter halos which can host galaxies affect the kSZ signal. This was then compared with various levels of X-ray contribution to reionization parametrized by the fraction of hydrogen ionizations due to X-rays, X_{frac}.

Our reionization model assumes that a constant number of ionizing photons are produced for each baryon which is incorporated into galaxies. We then calculate how many baryons have collapsed into dark matter halos at a given redshift using the extended Press-Schechter formalism. UV photons have a MFP much smaller than the pixel scale in our simulations while X-rays are assumed to uniformly ionize regions with a fixed comoving MFP, for simplicity. Varying the MFP between $\lambda = 20$ Mpc and $\lambda = 50$

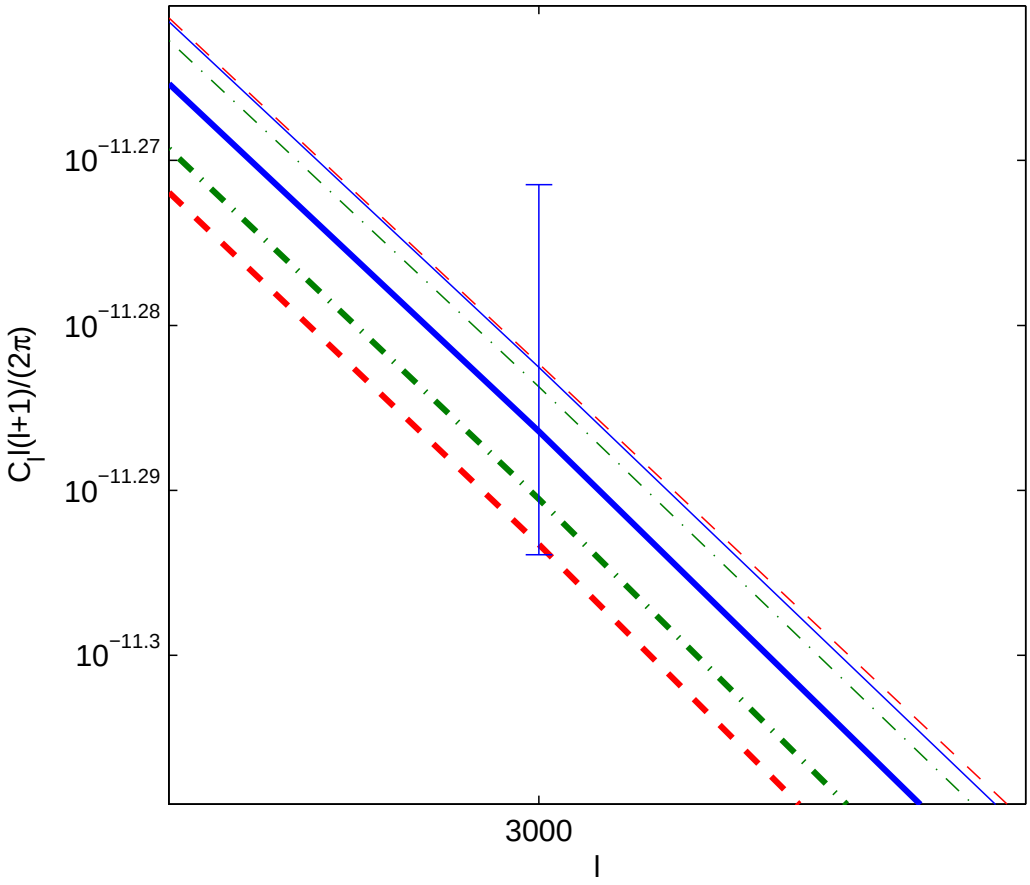

Figure 5.4.—: The angular power spectrum of temperature fluctuations at $l = 3000$, where ACT and SPT will be sensitive to kSZ signal. The expected accuracy of SPT, $\Delta\left(C_l l(1+l)/(2\pi)\right) = 1\mu\mathrm{K}^2/\bar{\mathrm{T}}^2_{\mathrm{CMB}}$, is shown as an error bar. The various reionization models are shown with the same lines as Figure 5.3.

Mpc yields very similar results, suggesting that our conclusions are robust.

Note that our method does not include the effects of X-rays from earlier epochs which redshift into UV photons and cause ionizations. Since photons from earlier epochs will have traveled very long distances, we expect they will create a fairly uniform background on the scales relevant to kSZ observations. In future work, it may be accurate to model this background as constant in space and calibrate its intensity by estimating the number density and spectral energy distribution of sources over cosmic time.

Semi-analytic techniques in the UV-only case have been shown to agree well with detailed numerical simulations that include radiative transfer (Zahn et al. 2011). Similarly, it will be interesting for future studies to compare the semi-analytic model in this paper with analogous simulations. From these comparisons it will be possible to determine what refinements in the model (e.g. X-ray heating, suppression of secondary ionizations at high ionization fraction) need to be made.

Due to the comparatively long MFP of X-rays, they can partially ionize the regions in between the ionized bubbles created by UV photons. For a fixed number of total hydrogen ionizations this results in smaller bubbles surrounded by partially ionized IGM. This affects the kSZ signal by reducing the "patchy" component of the fluctuations, associated with the non-uniform topology of reionization. In this way it is possible to distinguish models which have a very similar global reionization history but different X-ray contributions.

In particular, we find that an X-ray contribution greater than $X_{\rm frac} = 10\%$ produces a substantially lower power spectrum than our UV-only models constrained to have

equal total optical depth to electron scattering. This suggests that it may be possible to constrain the X-ray contribution to reionization with future kSZ observations. Unfortunately, the sensitivity of SPT and ACT may be insufficient to distinguish the models presented in this paper. However, a non-detection of the kSZ signal from the EoR may suggest a significant X-ray contribution. We find that our X-ray models push the kSZ power from reionization below the anticipated sensitivity of SPT and ACT. Because annihilation or decay of dark matter particles could imprint a similar uniform ionization component, such a non-detection could also be used to constrain the properties of dark matter.

Future radio observations of 21cm emission from neutral hydrogen in the IGM with instruments like the Murchison Widefield Array (MWA)[2] and the Low Frequency Array (LOFAR)[3] may also constrain the possible X-ray contribution to reionization (Venkatesan & Benson 2011; Thomas & Zaroubi 2008; Warszawski et al. 2009). Combining 21cm measurements and the kSZ results from SPT and ACT could improve the constraints and provide an important cross-check.

Acknowledgments

This work was supported in part by NSF grant AST-0907890 and NASA grants NNA09DB30A and NNX08AL43G (for A.L.).

[2]http://www.mwatelescope.org/

[3]http://www.lofar.org/

Table 5.2

Model	$C_l l(l+1)/(2\pi)$ at $l = 3000$
Fiducial	1.8×10^{-13}
Clump	1.7×10^{-13}
$M_{\rm min}$	1.8×10^{-13}
10% X-ray	1.4×10^{-13}
30% X-ray	0.86×10^{-13}
50% X-ray	0.53×10^{-13}

Table 5.2:: The contribution to the kSZ power spectrum from the EoR ($z = 6 - 20$) at $l = 3000$. The projected sensitivity of SPT is $\approx 1.4 \times 10^{-13}$.

Chapter 6

The Signature of the First Stars in Atomic Hydrogen at Redshift 20

E. Visbal, R. Barkana, A. Fialkov, D. Tseliakhovich, & C. Hirata *Nature*, Vol. 487, pp. 70-73, 2012

Dark and baryonic matter moved at different velocities in the early Universe, which strongly suppressed star formation in some regions (Tseliakhovich & Hirata 2010). This was estimated (Dalal et al. 2010b) to imprint a large-scale fluctuation signal of about 2 mK in the 21-cm spectral line of atomic hydrogen associated with stars at a redshift of 20, although this estimate ignored the critical contribution of gas heating due to X-rays (Madau et al. 1997; Pritchard & Furlanetto 2007) and major enhancements of the suppression. A large velocity difference reduces the abundance of halos (Tseliakhovich & Hirata 2010; Maio et al. 2011; Naoz et al. 2012) and requires the first stars to form in halos of about a million solar masses

(Stacy et al. 2011; Greif et al. 2011), substantially greater than previously expected (Abel et al. 2002; Bromm et al. 1999). Here we report a simulation of the distribution of the first stars at $z = 20$ (cosmic age of ~ 180 Myr), incorporating all these ingredients within a 400 Mpc box. We find that the 21-cm signature of these stars is an enhanced (10 mK) fluctuation signal on the 100-Mpc scale, characterized (Dalal et al. 2010b) by a flat power spectrum with prominent baryon acoustic oscillations. The required sensitivity to see this signal is achievable with an integration time of a thousand hours with an instrument like the Murchison Wide-field Array (Bowman et al. 2009) or the Low Frequency Array (Harker et al. 2010) but designed to operate in the range of 50–100 MHz.

The relative velocity between the dark matter and baryons also reduces the gas content of each halo. Previous work (Dalal et al. 2010b) assumed that this reduces star formation, but it mainly affects smaller halos that do not form stars (Tseliakhovich et al. 2011; Fialkov et al. 2012a). Another critical issue for observations of early stars is timing, since on the one hand, early times bring us closer to the primeval era of the very first stars (Abel et al. 2002; Bromm et al. 1999; Naoz et al. 2006; Fialkov et al. 2012a), but on the other hand, the cosmological 21-cm signal is obscured by the foreground (mainly Galactic synchrotron), which is brighter at longer wavelengths (corresponding to higher redshifts). Unlike the fluctuations at $z \sim 20$ from inhomogeneous gas heating, previously considered sources (Dalal et al. 2010b) produce smaller fluctuations and are likely to be effective only at $z \sim 30$ (Holzbauer & Furlanetto 2012).

We use a hybrid method to produce realistic, three-dimensional images of the expected global distribution of the first stars. We use the known statistical properties of

the initial perturbations of density and of the relative dark matter to baryon velocity to generate a realistic sample universe on large, linear scales. Then, we calculate the stellar content of each pixel using analytical models and the results of small-scale numerical simulations. In this approach we build upon previous hybrid methods used for high-redshift galaxy formation (Tseliakhovich & Hirata 2010; Dalal et al. 2010b; Mesinger et al. 2011b), and include a fit (Fialkov et al. 2012a) to recent simulation results on the effect of the relative velocity (Stacy et al. 2011; Greif et al. 2011) (for further details, see Supplementary Information section 6.1). Note that numerical simulations (even if limited to following gravity) cannot on their own cover the full range of scales needed to find the large-scale distribution of high-redshift galaxies (Barkana & Loeb 2004).

We assume standard initial perturbations (e.g., from a period of inflation), where the density and velocity components are Gaussian random fields. Velocities are coherent on larger scales than the density, due to the extra factor of $1/k$ in the velocity from the continuity equation that relates the two fields (where k is the wavenumber). Indeed, velocity fluctuations have significant power over the range $k \sim 0.01 - 0.5$ Mpc^{-1}, with prominent BAOs (Tseliakhovich & Hirata 2010).

We find a remarkable cosmic web (Figure 6.1), reminiscent of that seen in the distribution of massive galaxies in the present universe (Aihara et al. 2011; Colless et al. 2001; Springel et al. 2006). The large coherence length of the velocity makes it the dominant factor (relative to density) in the large-scale pattern. The resulting enhanced structure on 100 Mpc scales becomes especially notable at the highest redshifts (Figure. 6.2). This large-scale structure has momentous implications for cosmology at high redshift and for observational prospects. As the first stars formed, their radiation

(plus emission from stellar remnants) produced feedback that radically affected both the intergalactic medium and the character of newly-forming stars. Prior to reionization, three major transitions are expected due to energetic photons. Lyman-α photons couple the hyperfine levels of hydrogen to the kinetic temperature and thus make possible 21-cm observations of this cosmic era, while X-rays heat the cosmic gas (Madau et al. 1997). Meanwhile, Lyman-Werner (LW) photons dissociate molecular hydrogen and eventually end the era of primordial star formation driven by molecular cooling (Haiman et al. 1997b), leading to the dominance of larger halos (which are more weakly affected by the relative velocities). Due to the strong spatial fluctuations in the stellar sources (Barkana & Loeb 2004), these radiation backgrounds are inhomogeneous and should produce rich structure in 21-cm maps (Barkana & Loeb 2005b; Pritchard & Furlanetto 2007; Holzbauer & Furlanetto 2012; Naoz & Barkana 2008).

Figure 6.1.—: The effect of relative velocity on the distribution of star-forming halos at $\mathbf{z = 20}$. A two-dimensional slice (thickness = 3 Mpc) of a simulated volume of 384 Mpc (comoving) on a side at $z = 20$. To illustrate the previous expectations we show the overdensity (i.e., the relative fluctuation in density; **b**) and the relative fluctuation of the gas fraction in star-forming halos with the effect of density only (**d**). To illustrate the new predictions we show the magnitude of the relative baryon to dark-matter velocity (**a**), and the relative fluctuation of the gas fraction in star-forming halos including the effect of relative velocity (**c**). The relative velocity is given in units of the root-mean-square value. For the gas fraction, the colors correspond to the logarithm of the fraction normalized by the mean values, 0.0012 and 0.0021 for the case with and without the velocity effect, respectively; for ease of comparison, the scale in each plot ranges from 1/5 to 5 times the mean. In each panel, we indicate the scale of 130 comoving Mpc, which corresponds to the large-scale peak in the 21-cm power spectrum (see Figure 6.4). The no-velocity gas fraction map is a biased version of the density map, while the velocity effect increases the large-scale power and the map's contrast, producing larger, emptier voids.

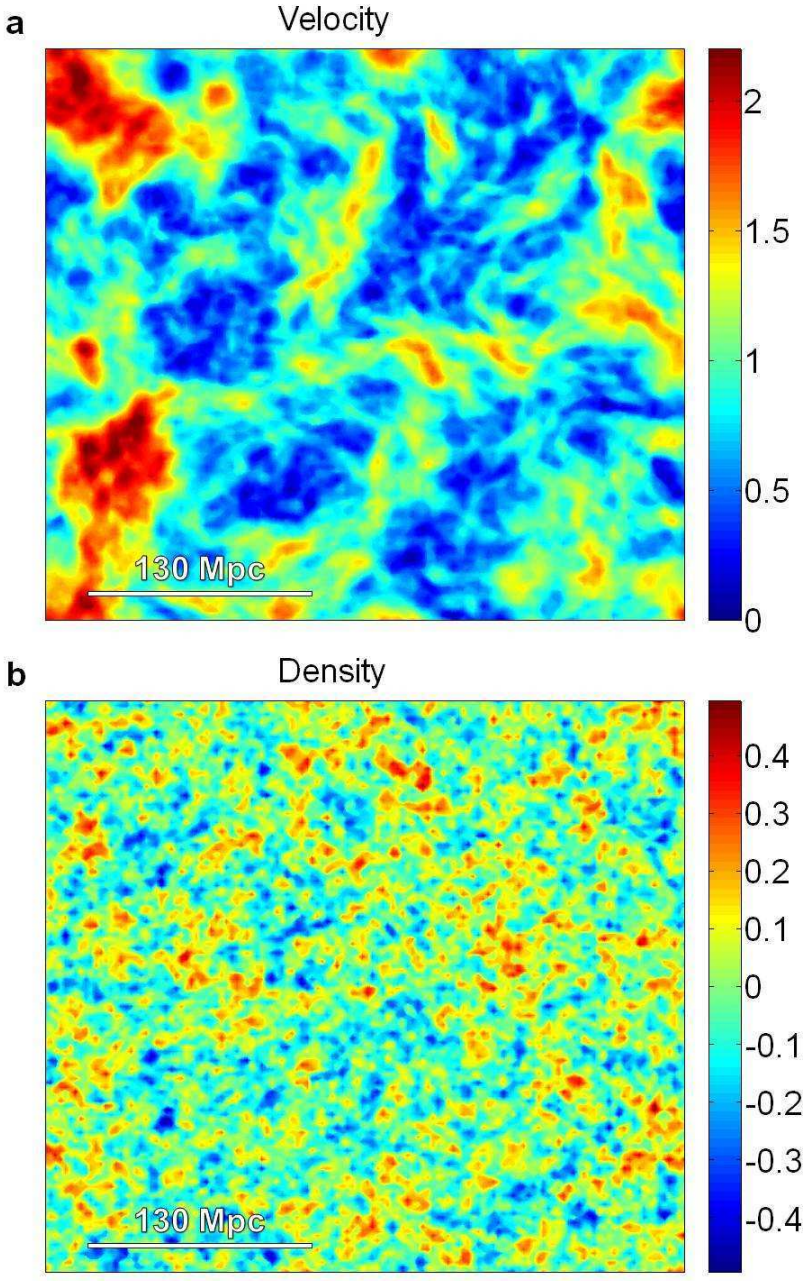

Figure 6.1.—: (Continued).

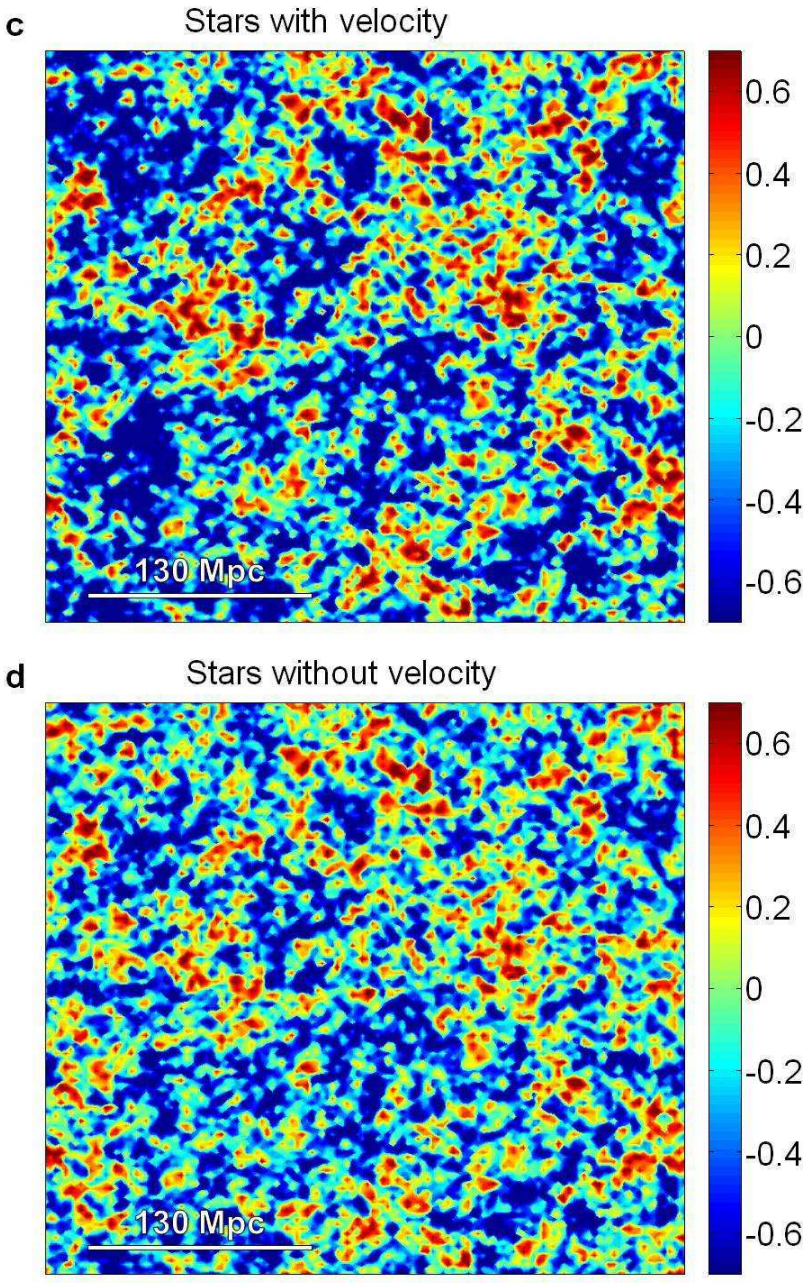

Figure 6.1.—: (Continued).

Figure 6.2.—: The effect of relative velocity on the distribution of star-forming halos at $\mathbf{z = 40}$. The gas fraction in star-forming halos in the same two-dimensional slice as in Figure 6.1 but at $z = 40$, with (**a**) and without (**b**) the relative velocity effect. The colors correspond to the logarithm of the gas fraction normalized by the mean values, 1.5×10^{-8} and 1.1×10^{-7} for the case with and without the relative velocity effect, respectively. The trends seen at $z = 20$ with the velocity effect are much stronger at $z = 40$, with 100 Mpc scales characterized by nearly isolated star-forming concentrations surrounded by deep voids; this implies a much more complex stellar feedback history, with the star-forming centers affected long before the voids.

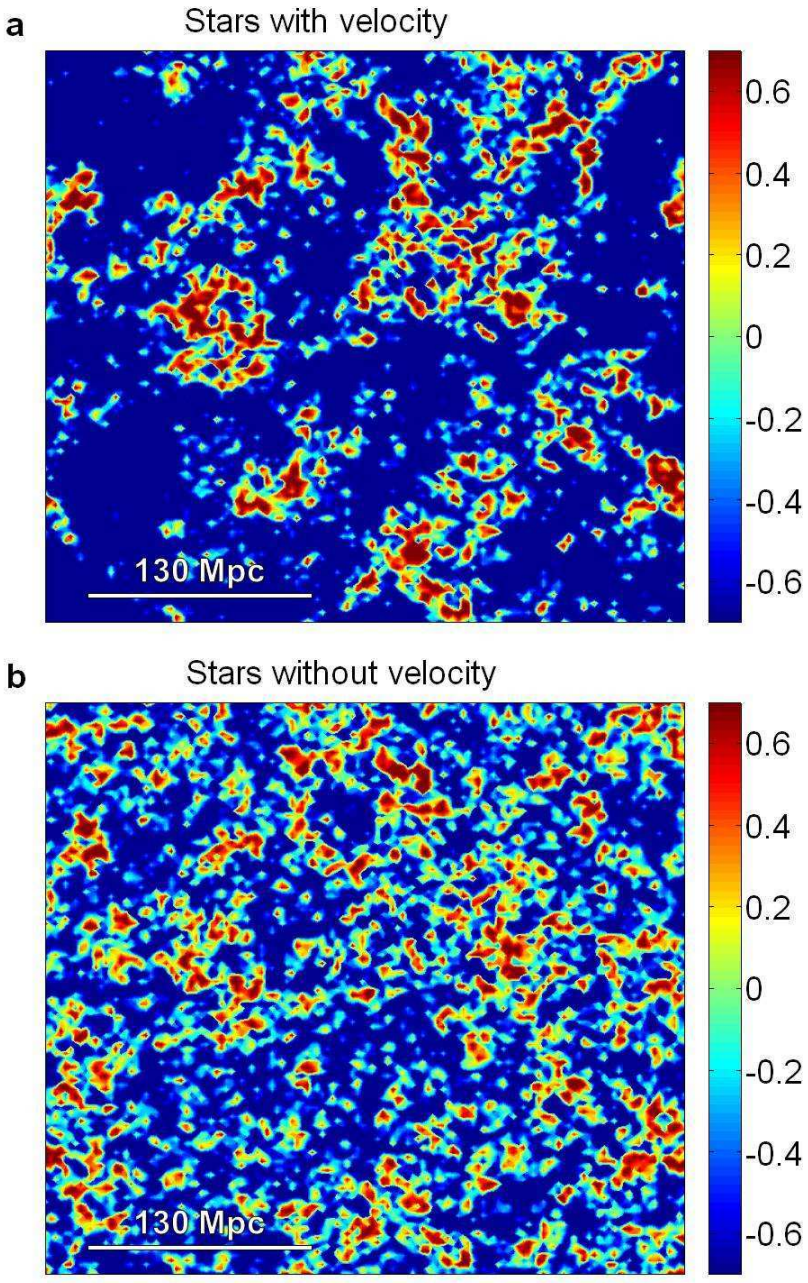

Figure 6.2.—: (Continued).

These radiation backgrounds have effective horizons on the order of 100 Mpc, due to redshift, optical depth, and time delay effects. Thus, the relative velocity effect on the stellar distribution leads to large-scale fluctuations in the radiation fields. This substantially alters the feedback environment of the first stars, making it far more inhomogeneous than previously thought. Observationally, these degree-scale fluctuations will affect various cosmic radiation backgrounds, and in particular the history of 21-cm emission and absorption (Figure 6.3), which depends on the timing of the three radiative transitions. Although it is still significantly uncertain, the 21-cm coupling due to Lyman-α radiation is expected to occur rather early, with the X-ray heating fluctuations occurring later and likely overlapping with significant small-halo suppression due to LW radiation (see Supplementary Information section 6.1.3 and Figure 6.5). Thus, we focus on the fluctuations due to X-ray heating at redshift 20, assuming that Lyman-α coupling has already saturated while bracketing the effect of the LW flux by considering the two limiting cases where the LW transition has either not yet begun or has already saturated.

Figure 6.3.—: The effect of relative velocity on the 21-cm brightness temperature at $z = 20$. The 21-cm brightness temperature (in units of mK) in the same two-dimensional slice as in Figure 6.1 at $z = 20$ with (**a**) and without (**b**) the relative velocity effect. For ease of comparison, both plots use a common scale that ranges from -79 to +58 mK; the no-velocity case is smoother and does not reach below -42 mK.

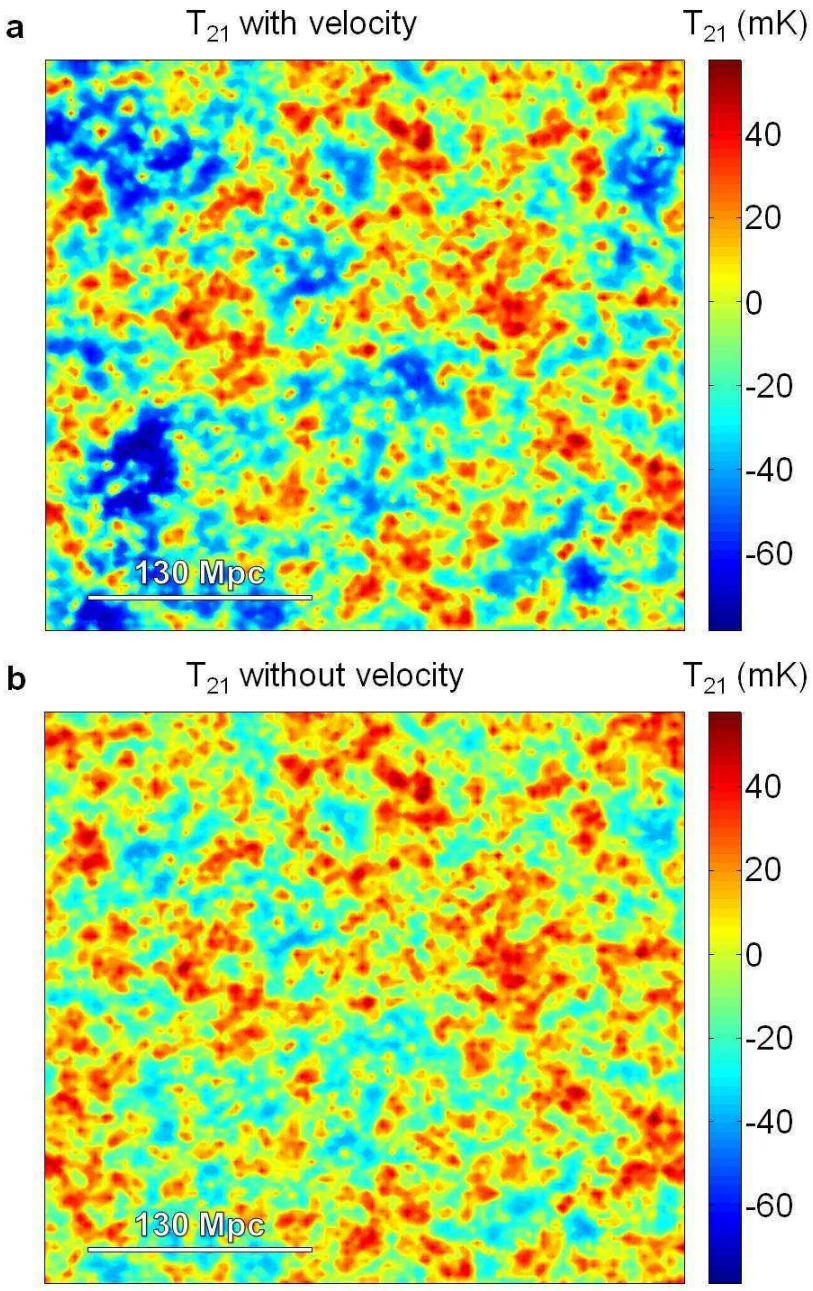

Figure 6.3.—: (Continued).

Fluctuations on large scales are easier to observe, since 21-cm arrays rapidly lose sensitivity with increasing resolution (Furlanetto et al. 2006b). For fixed comoving pixels, going from $z = 10$ to $z = 20$ increases the thermal noise per pixel by a factor of 30 (in the power spectrum), but this is more than compensated for if the required comoving resolution is 4 times lower than at $z = 10$. In the case of negligible LW flux, the relative velocity effect boosts the power spectrum on a scale of $2\pi/k = 130$ Mpc (0.°66 at $z = 20$) by a factor of 3.8, leading to 11 mK fluctuations on this scale and an overall flat power spectrum with a prominent signature of BAOs (Figure 6.4). If, on the other hand, the LW transition has already saturated, the power spectrum is even higher (e.g., 13 mK on the above scale) due to the dominance of larger halos (characterized by efficient atomic cooling) that are more highly biased; in this case, the effect of the streaming velocities is suppressed, reducing the oscillatory signature and steepening the power spectrum. We thus predict a strong, observable signal from heating fluctuations, regardless of the precise timing of the LW transition, with the signal's shape indicating the relative abundance of small versus large galaxies.

Figure 6.4.—: The signature of relative velocity in the 21-cm power spectrum at $z = 20$. Power spectrum of the 21-cm brightness temperature fluctuations versus wavenumber, at the peak of the X-ray heating transition at $z = 20$. We show the prediction for the case of a late LW transition for which the LW feedback is still negligible at $z = 20$ (blue solid curve); this no-feedback case shows a strong effect of the velocities. This is well above the projected 1-σ telescope sensitivity (McQuinn et al. 2006b) (green dashed curve) based on 1000-hour observations with an instrument like the Murchison Wide-field Array or the Low Frequency Array but designed to operate at 50–100 MHz, where we include an estimated degradation factor due to foreground removal (Liu & Tegmark 2012) (see Supplementary Information section 6.1.4 for details). Future experiments like the Square Kilometer Array should reach a better sensitivity by an order of magnitude (McQuinn et al. 2006b). We also show the prediction for an early LW transition that has already saturated by $z = 20$ (purple solid curve), in which case the power spectrum is essentially unaffected by the velocities. These two feedback cases bracket the possible range. We show for comparison the previous expectation for the no feedback case, without the velocity effect (red dotted curve). The velocity effect makes it significantly easier to detect the signal, and also creates a clear signature by flattening the power spectrum and increasing the prominence of the BAOs (which are more strongly imprinted in the velocity than in the density fluctuations). Each plotted result is the mean of 20 realizations of our full box (s.d. error bars are shown in the main case). In this plot we have fixed the heating transition at $z = 20$ for easy comparison among the various cases. In cases with effective feedback, the heating transition as well as the main portion of the feedback itself will be delayed to somewhat lower redshift, making the signal more easily observable.

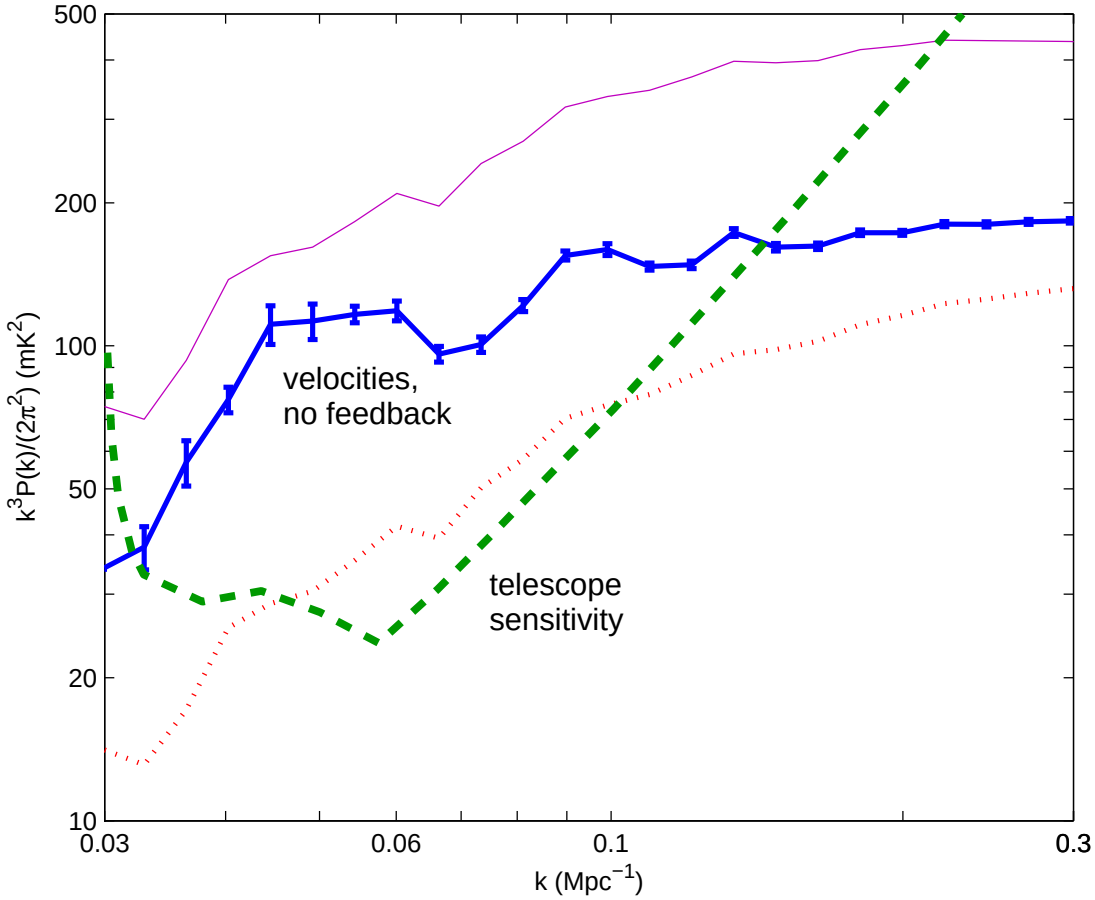

Figure 6.4.—: (Continued).

In general, the 21-cm fluctuation amplitude at a given redshift can be reduced by making galactic halos less massive (and thus less strongly clustered) or by increasing the X-ray efficiency (thus heating the cosmic gas past the temperature range that affects the 21-cm emission). Thus, the characteristic shape that we predict is essential for resolving this degeneracy and allowing a determination of the properties of the early galaxies. Moreover, similar observations over the full $\Delta z \sim 6$ redshift range of significant heating fluctuations could actually detect the slow advance of the LW feedback process, during which the power spectrum continuously changes shape, gradually steepening as the BAO signature weakens towards low redshift.

The exciting possibility of observing the 21-cm power spectrum from galaxies at $z \sim 20$ should stimulate observational efforts focused on this early epoch. Such observations would push well past the current frontier of cosmic reionization ($z \sim 10$, $t \sim 480$ Myr) for galaxy searches (Bouwens et al. 2011a) and 21-cm arrays (Furlanetto et al. 2006b). Detecting the remarkable velocity-caused BAO signature (which is much more prominent than its density-caused low-redshift counterpart (Anderson et al. 2012)) would confirm the major influence on galaxy formation of the initial velocity difference set at cosmic recombination. Measuring the abundance of $10^6 M_\odot$ halos would also probe primordial density fluctuations on ~ 20 kpc scales, an order of magnitude below current constraints. This could lead to new limits on models with suppressed small-scale power such as warm dark matter (Barkana et al. 2001).

6.1 Large Supplementary Information

6.1.1 Description of the Simulation Code

We developed our own code that implements a hybrid method to produce instances of the expected three-dimensional distribution of the first stars. We first used the known statistical properties of the initial density and velocity perturbations to generate a realistic sample universe on large, linear scales. Specifically, we assumed Gaussian initial conditions and adopted the initial power spectrum corresponding to the currently best-measured cosmological parameters (Komatsu et al. 2011). In a cubic volume consisting of 128^3 cells (each 3 comoving Mpc on a side), we generated as in our previous work (Tseliakhovich & Hirata 2010) a random realization, including the appropriate correlations, of the initial overdensity and relative baryon-dark matter velocity in each cell (with periodic boundary conditions). These values are easily computed at any redshift as long as the scales are sufficiently large to use linear perturbation theory. We then computed analytically the gas fraction in star-forming halos in each cell as a function of these two variables and the redshift, as in our previous papers. Specifically, this gas has density (Tseliakhovich et al. 2011)

$$\rho_{\rm gas} = \int_{M_{\rm cool}}^{\infty} \frac{dn}{dM} M_{\rm gas}(M)\, dM \ , \tag{6.1}$$

where dn/dM is the comoving abundance of halos of mass M (i.e., n is the comoving number density), $M_{\rm gas}(M)$ is the gas mass inside a halo of total mass M, and $M_{\rm cool}$ is the minimum halo mass in which the gas can cool efficiently and form stars. In this calculation (whose results are illustrated in Figures 6.1 and 6.2) we included three separate effects of the relative velocity on star formation (Fialkov et al. 2012a), namely

the effect on $M_{\rm cool}$, on dn/dM, and on $M_{\rm gas}(M)$ (see also section 6.1.2). The stellar density equals $\rho_{\rm gas}$ multiplied by the star-formation efficiency.

We then used this information to determine the X-ray heating rate in each cell as follows. At each redshift, we smoothed the stellar density field in shells around each cell, by filtering it (using fast Fourier transforms) with two position-space top-hat filters of different radii and taking the difference. We assumed the flux of X-ray photons emitted from each shell to be proportional to the star formation rate, which is in turn proportional to the time derivative of $\rho_{\rm gas}$. We assumed an X-ray efficiency of 1.75×10^{57} photons per solar mass in stars (1.15×10^{57} for the case with no streaming velocity) produced above the minimum energy (assumed to be 200 eV) that allows the photons to escape from the galaxy. The efficiency in each case was chosen so as to get the peak of the cosmic heating transition at $z = 20$, i.e., so that the mean kinetic gas temperature equals the cosmic microwave background (CMB) temperature at that redshift. The actual X-ray efficiency of high-redshift galaxies is highly uncertain, but 10^{57} photons per solar mass along with our adopted power-law spectrum corresponds to observed starbursts at low redshifts (Pritchard & Furlanetto 2007). We then computed the heating by integrating over all the shells seen by each cell, as in the 21CMFAST code (Mesinger et al. 2011b). In this integral, the radiative contribution of each cell to a given central cell was computed analytically at the time-delayed redshift seen by the central cell, using a pre-computed interpolation grid of star formation versus overdensity, streaming velocity, and redshift. We varied the number and thickness of shells to check for convergence. To estimate the optical depth, we assumed a uniform density and a neutral inter-galactic medium, but did not make a crude step-function approximation as in 21CMFAST. We used photoionization cross sections and energy deposition fractions from atomic physics

calculations (Verner et al. 1996; Furlanetto & Stoever 2010).

Given the X-ray heating rate versus redshift at each cell, we integrated as in 21CMFAST to get the gas temperature as a function of time. We interpolated the heating rate between the redshifts where it was explicitly computed, and varied the number of redshifts to ensure convergence. We then assumed that the spin temperature and the gas temperature are coupled to compute the 21cm signal, i.e., that the Lyman-α coupling has already saturated by $z = 20$, as expected (see section 6.1.3). Except for the differences noted, in the heating portion of the code we followed 21CMFAST and adopted their fiducial parameters, such as a 10% star-formation efficiency. However, our source distribution was substantially different since they did not include the effect of the streaming velocity. Since we focused on the era well before the peak of cosmic reionization, we did not calculate ionization due to ultra-violet or X-ray radiation. The kinetic temperature T_k and overdensity δ of the gas in each cell gave us the 21-cm brightness temperature (relative to the CMB temperature $T_{\rm CMB}$) (Madau et al. 1997)

$$\delta T_b = 40(1+\delta)\left(1-\frac{T_{\rm CMB}}{T_{\rm k}}\right)\sqrt{\frac{1+z}{21}}\ {\rm mK}\ , \tag{6.2}$$

and thus Figures 6.3 and 6.4. Finally, for Figure 6.5 (in section 6.1.3) we added a calculation of the inhomogeneous Lyman-Werner flux (Holzbauer & Furlanetto 2012) within the box using the halo distribution in the box similarly to our calculation of the inhomogeneous X-ray heating rate.

6.1.2 Comparison with Previous Work

In this section we briefly summarize previous work on the streaming velocity and note the differences with our work.

It is now known that the relative motion between the baryons and dark matter has three effects on halos: (1) suppressed halo numbers, i.e., the abundance of halos as a function of total mass M and redshift z; (2) suppressed gas content of each halo, i.e., the gas mass within a halo of a given M and z; and (3) boosted minimum halo mass needed for cooling, i.e., the minimum total mass M of halos at each redshift z in which catastrophic collapse due to cooling, and thus star formation, can occur. Note that this separation into three distinct effects is natural within our model (see Eq. 6.1 in section 6.1.1), but this does not preclude the possibility that they are physically correlated or mutually dependent.

The original paper in which the importance of the relative motion was discovered (Tseliakhovich & Hirata 2010) included only the impact on the halo abundance (effect #1). This was sufficient for them to deduce the important implication of enhanced large-scale fluctuations, but quantitatively the effect was underestimated. Also, their calculations had a number of simplifying assumptions: they calculated the baryon perturbations under the approximation of a uniform sound speed (which has a big impact on the no-streaming-velocity case which is still relevant in regions where the streaming velocity is low), and used the old (and relatively inaccurate) Press-Schechter halo mass function.

The effect of the relative velocity on suppressing the gas content of halos (effect #2) was the next to be demonstrated (Dalal et al. 2010b). These authors predicted significant fluctuations on large scales, with prominent baryon acoustic oscillations. However, they made a number of simplifying approximations (detailed previously (Fialkov et al. 2012a)). Most important were two limitations: they included only effect #2 (i.e., they left out the already-known #1), and they scaled star formation according to the total gas content

in halos, without including a cooling criterion for star formation. The vast majority of the gas is in minihalos that cannot cool, and because of their low circular velocities their ability to collect baryons is much more affected by the streaming velocity than the star-forming halos. Even more importantly, they only considered fluctuations in the Lyman-α radiation, which yielded a prediction at $z = 20$ of a large-scale power spectrum peak of amplitude 5 mK^2 (see their Figure 6.4). In comparison, in our Figure 6.4 the large-scale peak (due to X-ray heating fluctuations) is more than 20 times higher, at around 110 mK^2. We also note that they assumed a particularly low Lyman-α efficiency in order to get significant Lyman-α fluctuations at a redshift as low as 20, while such fluctuations are actually expected to be significant only at a much higher redshift (see section 6.1.3 below), where the observational noise is much higher.

In a subsequent paper (Tseliakhovich et al. 2011) we calculated the consequences of the combination of effects #1 and #2 on the distribution of star-forming halos as well as on star-less gas minihalos. At this point there were indications from numerical simulations (Maio et al. 2011; Stacy et al. 2011; Greif et al. 2011) that the minimum halo mass needed for cooling also changed as a result of the streaming velocity (effect #3). Recently, numerical simulations have also been used for a more robust and detailed look at effect #1 (Naoz et al. 2012). We have studied the three effects on halos and shown (Fialkov et al. 2012a) that the effect on star-forming halos, and thus also on the various radiation fields, is mainly due to effects #1 and #3, while the smaller gas minihalos are mainly affected by effects #1 and #2.

In summary, the existence and correct determination of the various effects of the streaming velocity on star formation have been worked out gradually. The present paper fully incorporates that understanding in order to study the implications for X-ray heating

fluctuations, resulting in a solid prediction of strong large-scale 21-cm fluctuations around redshift 20.

6.1.3 Timing of Feedback Transitions

In the main text, we noted that three radiative transitions are expected to occur at high redshift: Lyman-α coupling, X-ray heating, and Lyman-Werner suppression. In our results in Figure 6.4, we assumed that Lyman-α coupling occurs early, while the other two transitions occur later and may overlap. In this section we explain why this relative timing of the feedback transitions is expected.

It has been previously shown (Pritchard & Furlanetto 2007) that the heating transition is expected to occur significantly later than Lyman-α coupling. Specifically, the scenarios considered by these authors showed a clear period of observable 21-cm absorption before heating (see their Figure 1). They, however, considered scenarios in which only large (atomic cooling) halos are included. In our calculations, we included also the highly abundant molecular-cooling halos, and these help produce the various transitions at higher redshifts, and with a larger gap between the Lyman-α coupling and the heating transition. Specifically, we find that in our model the coupling transition (which is also when Lyman-α fluctuations are maximal) is expected to occur at redshift 27.8 (compared to 30.1 without the streaming velocity effect). Note that the result without velocities is in good agreement with a similar previous calculation (Holzbauer & Furlanetto 2012). For the heating transition, we adopted redshift 20 in the paper, but allowing for a range of uncertainty of an order of magnitude in the X-ray efficiency (centered around the efficiency of observed starbursts) gives a transition redshift within

$z = 17 - 21$, well after the peak of the Lyman-α coupling transition (the range is $z = 17 - 23$ without the velocity effect).

The third (LW) transition should occur significantly later than previously estimated in the literature. Both simulations of individual halos (Haiman et al. 2000b) and full cosmological simulations (Machacek et al. 2001; Wise & Abel 2007; O'Shea & Norman 2008) that investigated halo formation under the influence of an external LW background used an artificially input *fixed* LW flux during the entire halo formation process. In reality the LW flux rises exponentially with time (along with the cosmic star formation rate) at high redshifts. Taking the final, highest value reached by the LW flux when the halo forms, and assuming that this value had been there from the beginning, greatly overestimates the effect of the LW feedback. In fact, a change in LW flux takes some time to affect the halo. The flux changes the formation rate of molecular hydrogen, but it then takes some time for this to affect the collapse. For instance, if the halo core has already cooled and is collapsing to a star, changing the LW flux will not suddenly stop or reverse the collapse. Another indication for the gradual process involved is that the simulation results can be approximately matched (Machacek et al. 2001) by comparing the cooling time in halo cores to the Hubble time (which is a relatively long timescale). Thus, estimates (Haiman et al. 2000b; Holzbauer & Furlanetto 2012) of the LW feedback based on the LW flux at halo virialization overestimate the transition redshift.

In order to better estimate the effect of LW feedback, we have calculated the mean LW intensity in our simulated volume, and compared it to a critical threshold for significant suppression of halos. We adopt a threshold intensity of $J = 10^{-22}$ erg s^{-1} cm^{-2} Hz^{-1} sr^{-1} as defining the center of the LW transition. The above-mentioned cosmological simulations indicate that at this intensity, the minimum halo mass for

cooling (in the absence of streaming velocities) is raised to $\sim 2 \times 10^6 M_\odot$ due to the LW feedback. This is a useful fiducial mass scale, roughly intermediate (logarithmically) between the cooling masses obtained with no LW flux or with saturated LW flux, and characteristic of the scale at which the streaming velocity effect is significantly but not overwhelmingly suppressed (e.g., the velocity effect on the halo abundance is maximized at this mass scale (Tseliakhovich & Hirata 2010)). Thus, at this level of LW suppression we would expect the 21-cm power spectrum (in the case of an X-ray heating transition at $z = 20$) to be approximately the average of the two top curves in Figure 6.4. Note that even in the case of a fully saturated LW feedback, a minor $(5 - 10\%)$ effect remains for the velocities on the 21-cm power spectrum.

A key point is that the critical feedback threshold must be compared not to the LW intensity when the halo virializes, but to its typical or average value during the entire process of halo formation. Another important feature is that the LW transition is very gradual. Adopting a reasonable range of uncertainty, we find (Figure 6.5) that the LW transition, for our adopted parameters, should be centered somewhere in the range $z = 21 - 28$, with its main portion extending over a $\Delta z \sim 6 - 8$ (note that the center is expected in the range $z = 24 - 31$ without the velocity effect). In fact, the feedback itself will delay the heating transition to lower redshift, so that in general we expect redshift 20 to show a significant velocity signature.

Figure 6.5.—: The expected timing of the Lyman-Werner feedback. We show the mean Lyman-Werner intensity J in our simulation box as a function of redshift, with (solid) and without (dashed) the relative velocity effect. In each case, we show the actual intensity (top, thin curve), and a range of effective intensities for halo feedback (bottom, thick curves). Specifically, for the effective intensity we adopt the intensity that was in place at the midpoint of halo formation. This is a reasonable estimate of the characteristic value during halo formation since, during the formation process, half the time J was below this value, and half the time above it. We estimate the midpoint of halo formation (in terms of cosmic age) based on the standard spherical collapse model (Gunn & Gott 1972a). To obtain a plausible range of uncertainty, we consider the start of halo formation to be either the beginning of the universe, or the start of the actual collapse (i.e., the moment of turnaround); the former yields an earlier characteristic time and corresponds to the bottom curve in each case. Also shown (horizontal lines) are critical values of LW intensity (to be compared with the effective intensities) that correspond to the central portion of the LW transition, during which the minimum halo mass for cooling (in the absence of streaming velocities) is raised by LW feedback to (Wise & Abel 2007) $8 \times 10^5 M_\odot$, $2 \times 10^6 M_\odot$, and $5 \times 10^6 M_\odot$, respectively.

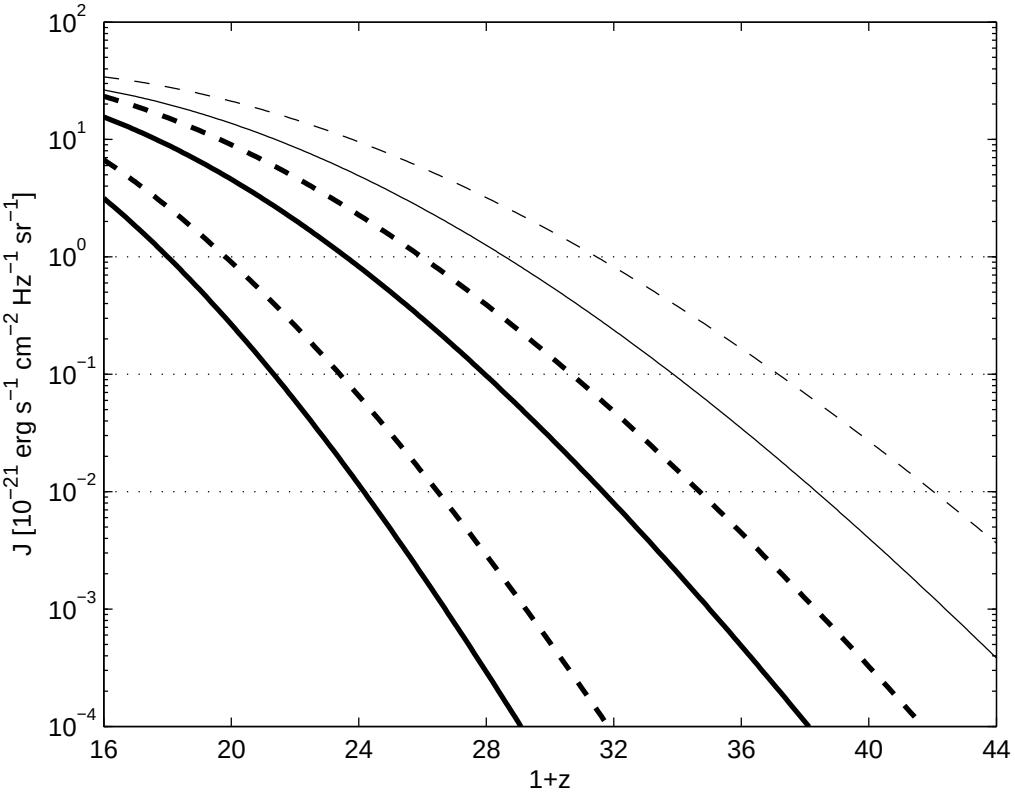

Figure 6.5.—: (Continued).

We conclude that the Lyman-α transition occurs well before the X-ray heating transition, while the latter likely overlaps in redshift with the LW transition. Note that the prediction for the Lyman-α transition is more secure (for a given star formation efficiency) than the others, since the Lyman-α radiation comes directly from stars (unlike the more uncertain X-ray emission associated with stellar remnants), and it directly affects the low-density intergalactic gas (unlike the more uncertain LW feedback which occurs within the non-linear cores of collapsing halos). In particular, the LW feedback may be further delayed by complex local feedback effects that can oppose the suppression effect (Ahn & Shapiro 2007; Johnson et al. 2007).

6.1.4 Observational Considerations

In the main text we argued that there are good prospects for observing the 21-cm power spectrum that we predict at redshift 20. In this section we briefly elaborate on the experimental sensitivity that we adopted and on the observational challenges.

In Figure 6.4 we showed the projected 1-σ sensitivity of one-year observations with an instrument like the first-generation MWA and LOFAR experiments. Specifically, we adopted the projected sensitivity of the MWA from a detailed analysis of the sensitivity to the power spectrum (McQuinn et al. 2006b). The parameters of the actual instruments have changed somewhat, but in any case no current instrument is designed for observations at $z = 20$; we considered instruments in the same class of capabilities but designed to operate at 50–100 MHz. Specifically, we assumed an instrument with 500 antennas, a field of view of 800 deg^2, and an effective collecting area at $z = 20$ of 23,000 m^2, and scaled the noise power spectrum from redshift 12 to redshift 20 up by a

factor of 12 [proportional to $(1+z)^{5.2}$] due to the brighter foreground (McQuinn et al. 2006b). The sensitivity in Figure 6.4 is calculated for an 8 MHz band and bin sizes of $\Delta k = 0.5k$. It assumes a 1000 hr integration in a single field of view, i.e., it allows for a selection (out of an 8800 hr year) of night-time observations with favorable conditions.

An instrument like LOFAR – with 64 antennas, a field of view of 50 deg^2, and a collecting area at $z = 20$ of 190,000 m^2 – should have a slightly better power spectrum sensitivity, i.e., lower noise by about a factor of two (McQuinn et al. 2006b). A second-generation instrument should reach a substantially better sensitivity, e.g., by an order of magnitude for the SKA or a 5000-antenna MWA (McQuinn et al. 2006b).

A possible concern, especially with large-scale modes in the 21-cm signal, is the degeneracy with the foregrounds. At each point on the sky, or at each point in the Fourier (u, v)-plane, the intensity spectrum of synchrotron and free-free foregrounds is smooth. The fitting and removal of these foregrounds also removes some of the signal at small radial wavenumbers $k_\parallel$, which means that the power spectrum of the cosmological 21-cm signal at sufficiently small k is not measurable.

The range of wavenumbers k that are affected by foregrounds follows from geometrical considerations as well as the complexity of the foreground model that must be removed. The first issue is that template projection removes a range of $k_\parallel = k\cos\theta$ rather than a range of k, where θ is the angle between the wave vector and the line of sight. Therefore if we must cut at some $k_{\parallel,\rm min}$ then all values of $k < k_{\parallel,\rm min}$ are rejected, and at larger values of k a fraction $1 - k_{\parallel,\rm min}/k$ survive. The foreground model consists of a smooth function such as a low-order polynomial (as well as Galactic radio recombination lines confined to specific frequencies (Oh & Mack 2003)).

The relation between the foreground model complexity and the range of suppressed $k_\parallel$ is more complex (Liu & Tegmark 2012). The simplest argument to derive $k_\parallel$ is via mode counting: at each pixel in the (u, v)-plane of size $\Delta u\,\Delta v = \Omega^{-1}$ (where Ω is the solid angle of the survey), if one removes a polynomial of order $N-1$ (i.e., with N independent coefficients) then one has removed the lowest N radial modes. Since the number of modes per unit radial wavenumber (including both positive and negative $k_\parallel$) is $\Delta r/(2\pi)$, where Δr is the radial width of the survey, mode-counting would suggest that radial wavenumbers from $-k_{\parallel,\min} < k < k_{\parallel,\min}$ are lost in the projection, giving $k_{\parallel,\min} = \pi N/\Delta r$. Despite its simplicity, the mode-counting argument holds up well against much more detailed studies. A good example (Bowman et al. 2009) is a simulated foreground subtraction in the frequency range 142–174 MHz, using the subtraction of a cubic polynomial ($N = 4$). This corresponds to a radial shell of width $\Delta r = 551\,\mathrm{Mpc}$. Mode-counting suggests that subtraction of real signal should become an issue at $k_{\parallel,\min} = 0.023\,\mathrm{Mpc}^{-1}$, and in fact Figure 13 of these authors (Bowman et al. 2009) shows that the 21-cm signal remains intact over the entire range of scales investigated (0.03–1.0 Mpc^{-1}). Larger values of $k_{\parallel,\min}$ occur in calculations with narrower bandwidths (Petrovic & Oh 2011b).

For our $z = 20$ case, assuming a bandwidth of 60–80 MHz, the same mode-counting argument leads to $k_{\parallel,\min} = 0.03\,\mathrm{Mpc}^{-1}$ for $N = 5$. Thus we would expect that if the foregrounds can be described by the lowest 5 modes over a factor of 1.33 in frequency, that they are distinguishable from our signal. In Figure 6.4 we have included the estimated degradation of the observational sensitivity for these parameters, with a $1/\sqrt{1 - k_{\parallel,\min}/k}$ factor.

This of course leaves open the issue of how many foreground modes actually need

to be removed. A previous study (Liu & Tegmark 2012) suggests 3–4 modes might be sufficient, but they considered higher frequencies (where the foreground:signal ratio is smaller) and used principal components of their foreground spectra (which given their assumptions must work better than polynomials, although after rescaling by an overall power law their eigenfunctions are – unsurprisingly – very similar to polynomials). Fortunately, if the foreground spectrum is analytic (as expected for synchrotron and free-free emission), polynomial fits are expected to converge exponentially fast to the true foreground spectrum as N is increased. The true value of N that will be required for future 21 cm experiments (and hence the required $k_{\parallel,\mathrm{min}}$) will likely be determined by how well such smooth functions can really describe the foreground.

The most difficult part of the foreground removal has been the calibration problem: even if the foreground frequency spectrum is smooth, frequency-dependent calibration errors will beat against the bright foreground and produce spurious frequency-dependent fluctuations. The problem is made more difficult by the nature of interferometry: a baseline measuring a particular Fourier mode in the (u, v)-plane at one frequency ν actually measures a different Fourier mode, $(\nu'/\nu)(u, v)$, at a neighboring ν'. Thus each pixel in (u, v)-space is actually made up from different pairs of antennas as the frequency varies, which means that the relative calibration of the gains and beams of all antennas must be known very accurately (Bowman et al. 2009; Datta et al. 2010; Morales et al. 2012). Note that the relevant gain and beam are those projected onto the sky, including phase and (of particular importance at lower frequencies) amplitude shifts induced by the ionosphere. The polarization calibration is also important: Faraday rotation is expected to produce rapidly varying structure in the polarized Stokes parameters Q and U of the Galactic synchrotron radiation, which has been observed at high Galactic

latitudes at frequencies as low as 150 MHz (Bernardi et al. 2010) (albeit with some nondetections (Pen et al. 2009a), which may be the result of lower sensitivity). The proper extrapolation of this signal to the $z \sim 20$ band is not clear, as it depends in detail on the small-scale structure of the emitting and rotating regions, but it seems likely that leakage into the Stokes I map will need to be carefully controlled. The current ($z \sim 10$) 21-cm experiments are working to achieve the required accuracy in calibration and it is hoped that they will succeed in laying the groundwork for similar efforts at higher redshift.

Chapter 7

A Simple Model for the Density Profiles of Isolated Dark Matter Halos

E. Visbal, A. Loeb, & L. Hernquist arXiv:1206.5852

Abstract

We explore the possibility that the density profiles of elliptical galaxies and cold dark matter (CDM) halos found in cosmological simulations can be understood in terms of the same physical process, collisionless gravitational collapse. To investigate this, we study a simplified model, the collapse of a perfectly cold Plummer sphere. First, we examine an N-body simulation of this model with particles constrained to purely radial orbits. This results in a final state characterized by a profile slightly steeper than $\rho \propto r^{-2}$ at small

radii and behaving as $\rho \propto r^{-4}$ at large radii, which can be understood in terms of simple analytic arguments. Next, we repeat our simulation without the restriction of radial orbits. This results in a shallower inner density profile, like those found in elliptical galaxies and CDM halos. We attribute this change to the radial orbit instability (ROI) and propose a form of the distribution function (DF) motivated by a physical picture of collapse. As evidence of the link between our model and CDM halos, we find that our collapse simulation has a final state with pseudo-phase-space density which scales roughly as $\rho/\sigma^3 \propto r^{-1.875}$, like that observed in CDM halos from cosmological simulations (Navarro et al. 2010). The velocity anisotropy profile is also qualitatively similar to that found near the centers of these halos. We argue that the discrepancy at large radii (where CDM halos scale as $\rho \propto r^{-3}$) is due to the presence of the cosmological background or continued infall. This leads us to predict that the outer CDM halo density profile is not "universal," but instead depends on cosmological environment (be it an underdense void or overdense region).

7.1 Introduction

Over roughly the past 15 years, considerable attention has been directed at the possibility that halos in cold dark matter (CDM) universes may have so-called "universal" density profiles. This idea was motivated by studies of cosmological N-body simulations which found that the spherically averaged density profiles of CDM halos could be accurately fit by the same simple function for a very large range in mass (Navarro et al. 1996). This

discovery led to the popular NFW profile parameterization,

$$\rho_{\rm NFW}(r) \propto \frac{1}{(r/r_s)\,(1+r/r_s)^2}, \tag{7.1}$$

where r_s is a characteristic length scale. There have been numerous attempts to understand the physical nature of the NFW profile and other similar parameterizations. The work has mostly focused on an origin within the cosmological context, investigating the role of large-scale structure and cosmological infall and accretion (e.g. Lithwick & Dalal 2011; Dalal et al. 2010a; Subramanian et al. 2000; Zukin & Bertschinger 2010a,b). These efforts have generally failed to produce a complete physical description of the processes which lead to the halo density profiles found in simulations.

It is well known that elliptical galaxies have surface density distributions described by the de Vaucouleurs $R^{1/4}$ law (or its generalization the Sersic law) (e.g. Trujillo et al. 2004; Graham & Guzmán 2003). A convenient analytical approximation to the deprojected $R^{1/4}$ law is given by the Hernquist model (Hernquist 1990)

$$\rho_{\rm H}(r) \propto \frac{1}{(r/r_s)\,(1+r/r_s)^3}. \tag{7.2}$$

The NFW and Hernquist profiles are strikingly similar, only differing asymptotically at large radii. This suggests a link between the density profiles of elliptical galaxies and CDM halos. In fact, they can be accurately fit in projection by the Sersic law or in three dimensions by a related profile, the Einasto model, which has been shown to fit CDM halos more accurately than the NFW parameterization (Merritt et al. 2005; Navarro et al. 2010). This similarity motivates the hypothesis that the same physical processes are responsible for the form of the density profiles in both CDM halos and elliptical galaxies.

This leads us to propose that the formation of CDM halos can be understood, at least in part, in terms of the physics of dissipationless gravitational collapse common to elliptical galaxies and CDM halos. We can apply this physics to better understand the density profiles observed in cosmological simulations. For example, the analytic arguments made 25 years ago by Jaffe (1987) and White (1987) imply that in the outer regions of isolated elliptical galaxies the density scales as $\rho \propto r^{-4}$. We suggest, that for dark matter halos, any deviation from this is due to continued accretion or because at large radii the cosmological background density dominates. Thus, to the extent that the structure of halos depends on their instantaneous accretion state or the local background density, the notion that CDM halos have "universal" density profiles is not accurate. In a ΛCDM universe, an isolated halo in a very low density environment will stop accreting relatively early, and hence will achieve the limiting form $\rho \propto r^{-4}$. This is consistent with the results of the cosmological simulations of Dubinski & Carlberg (1991), where vacuum boundary conditions led to an outer profile with $\rho \propto r^{-4}$. We also note that the recent work of Lithwick & Dalal (2011) and Vogelsberger et al. (2011) demonstrates that for scale-free models, the inner halo profile is sensitive to the shape of the collapsing perturbation. This suggests that the inner profile of halos could be sensitive to environment as well.

In this paper, the first in a series of two, we explore the physics of dissipationless gravitational collapse and how it applies to the formation of CDM halos. We accomplish this with numerical experiments and analytic arguments based on a simple toy-model, the collapse of a perfectly cold (zero initial kinetic energy) Plummer sphere. In Paper 2 (in preparation) we will study the impact of cosmological effects, such as continued accretion. This will include analyzing cosmological N-body simulations to study the

expected systematic dependence of the detailed profile on cosmological environment, be it an underdense void or an overdense region.

We begin the study of our collapsing Plummer sphere by performing a simulation of purely radial collapse in which non-radial motions are suppressed. This results in a final equilibrium state with a density profile slightly steeper than $\rho \propto r^{-2}$ near the center and $\rho \propto r^{-4}$ at large radii. However, a system composed entirely of particles on purely radial orbits will be dynamically unstable once non-radial motions are allowed, owing to the radial orbit instability (ROI), an effect first noted by Barnes et al. (1986) and Merritt & Aguilar (1985). When we remove the restriction of purely radial orbits we find a final state with a shallower inner profile more similar to that found in elliptical galaxies and CDM halos. The possibility that the ROI could play a role in structuring CDM halos has been emphasized already by Bellovary et al. (2008). Below, we examine this idea in greater depth by postulating a physically motivated form for the distribution function (DF) of systems which have relaxed through the ROI. As evidence of the link between our simple collapse model and CDM halos, we find that the final state has a pseudo-phase-space density $\rho(r)/\sigma(r)^3 \propto r^{-1.875}$, as observed in halos in N-body cosmological simulations (Navarro et al. 2010) and derived in self-similar secondary infall models (Bertschinger 1985).

This paper is structured as follows. In Section 7.2 we present the simulation of our toy-model of gravitational collapse with particles restricted to purely radial orbits. In the following section, we discuss the outer density profile of this numerical experiment and how it relates to CDM halos and elliptical galaxies. We consider the inner density profile in Section 7.4. Here we re-simulate the collapse from Section 7.2 without the restriction of purely radial orbits, and discuss the impact of the ROI. In Section 7.5 we

propose a physically motivated DF for the final state of systems formed through initially radial gravitational collapse. We discuss our results in the context of previous work in Section 7.6 and give our main conclusions in Section 7.7.

Throughout the paper, the data from our numerical experiments are presented in the internal units we use in the GADGET N-body code (Springel 2005). Distances are given in units of 1kpc, velocities in units of 1km s^{-1}, and mass in units of $10^{10} M_{\odot}$. Other units (e.g. time, energy, density) are given by the relevant combination of these three quantities.

7.2 A Simple Example

We begin the exploration of our simplified model with an N-body simulation of gravitational collapse where particle orbits are constrained to be completely radial. The simulation was initialized as a perfectly cold (all particles with zero velocity) Plummer sphere with scale length of 100 and total mass of 100 in the code units described above. These choices are unimportant, as neither the total mass nor the scale length affect the shape of the density profile for the final state. The system was evolved in time with particles only subjected to the component of the gravitational force in the radial direction. This was accomplished by modifying the publicly available N-body code GADGET (Springel 2005). The simulation was run until it reached an equilibrium state, with the density profile plotted in Figure 7.1. We have achieved convergence in the sense that the final state is not sensitive to the number of particles included in the simulation. For the results shown, we used 10^5 particles which were initially distributed by randomly drawing from a probability density function (PDF) proportional to the Plummer profile.

A gravitational softening length of $\epsilon_g = 0.3$ was adopted; reducing this value did not affect the results on the scales of interest. Note that the specific choice of a Plummer sphere does not have a strong impact on the final state. We find similar outcomes with other initial density profiles (e.g. Gaussian or Hernquist).

Our simulation results in an equilibrium state slightly steeper than $\rho \propto r^{-2}$ at small radii and $\rho \propto r^{-4}$ at large radii. We can show that in general, a density profile formed through purely radial collapse cannot be shallower than $\rho \propto r^{-2}$ using fairly simple analytical arguments (Dalal et al. 2010a). In the central regions, the time averaged contribution to the total density profile from each particle is

$$\rho_p(r) \propto \frac{dt(r)}{4\pi r^2 dr} \propto \frac{1}{r^2}\frac{dt}{dr}, \tag{7.3}$$

where $dt(r)$ is the time the particle spends between radii r and $r + dr$. For a density profile shallower than $\rho \propto r^{-2}$, dt/dr is a constant for sufficiently small r. It follows from equation (7.3) that central density profiles must always be at least as steep as $\rho \propto r^{-2}$ in the purely radial case.

The large radius limit can be explained with the following argument (White 1987; Jaffe 1987). In the final state of a system formed through gravitational collapse, the outer envelope will be populated by particles which have been scattered into weakly bound orbits. The size of these orbits will be inversely proportional to the energy, E. The number of particles between E and $E + dE$, $N(E)dE$, is expected to be non-zero and continuous near $E = 0$. For the density, this implies

$$\rho(r) = \frac{N(E)}{4\pi r^2}\frac{dE}{dr} \propto \frac{N(GM/r)}{r^2}\frac{d(GM/r)}{dr} \propto r^{-4}. \tag{7.4}$$

Note that this result was derived in the context of elliptical galaxies and has been completely ignored in the literature on cosmological CDM halo formation.

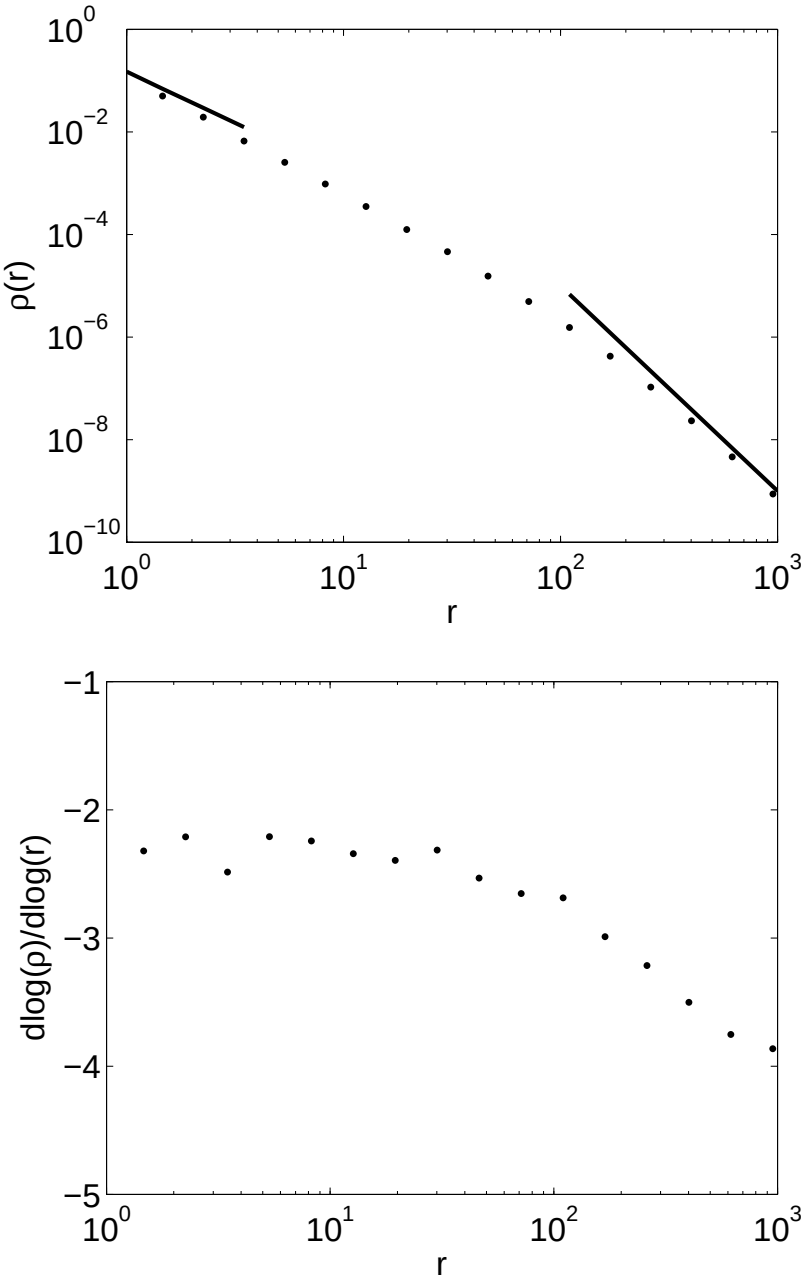

Figure 7.1.—: The density profile (top panel) and logarithmic slope (bottom panel) of the final state from our simulation of purely radial collapse starting from a perfectly cold Plummer sphere (see Section 7.2 for more details). The solid lines indicate $\rho \propto r^{-2}$ at small radii and $\rho \propto r^{-4}$ at large radii.

Although the above discussion is (intentionally) highly idealized, it demonstrates some important consequences. First, there is nothing mysterious or pathological about density profiles which diverge as $r \to 0$. Second, the large-r behavior is consistent with the analytical arguments of White (1987) and Jaffe (1987). Note that while "violent-relaxation" (Lynden-Bell 1967) plays a role in the evolution by redistributing energy among the particles, and hence promoting a small fraction to unbound orbits, it does not in detail determine the limiting behavior at small and large radii, and hence does not justify efforts to understand the nature of the generic density profiles based on thermodynamic arguments (e.g. Spergel & Hernquist 1992). Finally, the lack of sensitivity to the number of particles indicates that the outcome has been determined by the physics of collisionless dynamics. We argue that the physical processes acting in this example are, at least in part, responsible for the origin of the density profiles of dark matter halos. While the density profile obtained from this example does not match the NFW form, we can nevertheless use it as a starting point for the more detailed study described in the following sections.

Before moving on, we note that the final state in this example can be approximated by the density profile of the Jaffe model,

$$\rho_{\rm J}(r) \propto \frac{1}{(r/r_s)^2\,(1+r/r_s)^2}. \tag{7.5}$$

However unlike the isotropic Jaffe model, the velocities are purely radial and therefore are dynamically unstable when particles are permitted to have non-radial velocities (as we explore below). Note that the DF for a Jaffe model density profile constrained to purely radial orbits can be expressed analytically. We derive this expression in the Appendix.

7.3 The Outer Density Profile

According to the arguments put forward by White (1987) and Jaffe (1987), an isolated collisionless system evolving into equilibrium through collapse should eventually achieve the limiting form $\rho \propto r^{-4}$ at large radii. This expected outcome is in agreement with the simple numerical experiment presented in Section 7.2. Note that the analytic argument is insensitive to orbital anisotropy, and therefore is unaffected by the imposed constraint of purely radial orbits. We point out that this large radius behavior should also occur in dark matter halos once cosmological infall terminates. Dubinski & Carlberg (1991) originally demonstrated this using cosmological simulations in which they employed vacuum boundary conditions around individual objects which naturally led to a cessation of late time accretion.

We suggest that the NFW profile at large radii, $\rho \propto r^{-3}$, does not directly reflect the physical processes that form CDM halos. We find in our collapse simulations (both the purely radial case discussed above and the generalized case discussed below) that the density profile reaches $\rho \propto r^{-4}$ roughly two orders of magnitude beyond the radius where $d\ln(\rho)/d\ln(r) \approx -2$. For most CDM halos in the cosmological context, the background density will dominate at such large radii. Thus, CDM halos may not extend far enough before falling below the background density to achieve $\rho \propto r^{-4}$. Additionally, continued infall in high density regions could alter the outer profile. This finding has important implications for understanding the formation of halos in a cosmological context. Low-density regions will behave as open universes, implying that accretion there will halt earlier than in higher density environments. Some regions may be underdense enough to permit halos to reach the asymptotic form $\rho \propto r^{-4}$. Therefore, it is expected that the

outer profiles of halos may exhibit a variety of behaviors, depending on environment and redshift, so in detail the outer profiles of dark matter halos will not be characterizing by a universal form. This will be explored in detail in paper 2 (in preparation).

7.4 The Inner Density Profile and the Radial Orbit Instability

To investigate the small-radii properties of equilibrium systems formed through gravitational collapse, we generalize the numerical experiment described in Section 7.2. We perform the same N-body simulation of radial collapse, but relax the restriction that the particles move on purely radial orbits. Here we use 2×10^6 particles and a softening length of $\epsilon_g = 0.1$. We find that we have achieved convergence in the sense that increasing particle number or decreasing softening length do not impact our results on the scales of interest. Since our results are not sensitive to particle number, we conclude that 2-body relaxation does not impact our results and the system is effectively collisionless. As in the purely radial simulation, different initial density profiles result in similar final equilibrium states. The results of this simulation are presented in Figure 7.2. Note that the simulation was run roughly five times the dynamical time at the maximum radius shown. While we may not have reached perfect equilibrium at this radii, we do not expect substantial changes at longer times.

Figure 7.2.—: The final state of the N-body simulation of collapse from a cold (zero velocities) Plummer sphere described in Section 7.4. We plot radial profiles of the density, cumulative mass interior to a radius r, anisotropy parameter, and logarithmic slope. The solid line indicates $\rho \propto r^{-4}$ and the dashed line marks the half-mass radius.

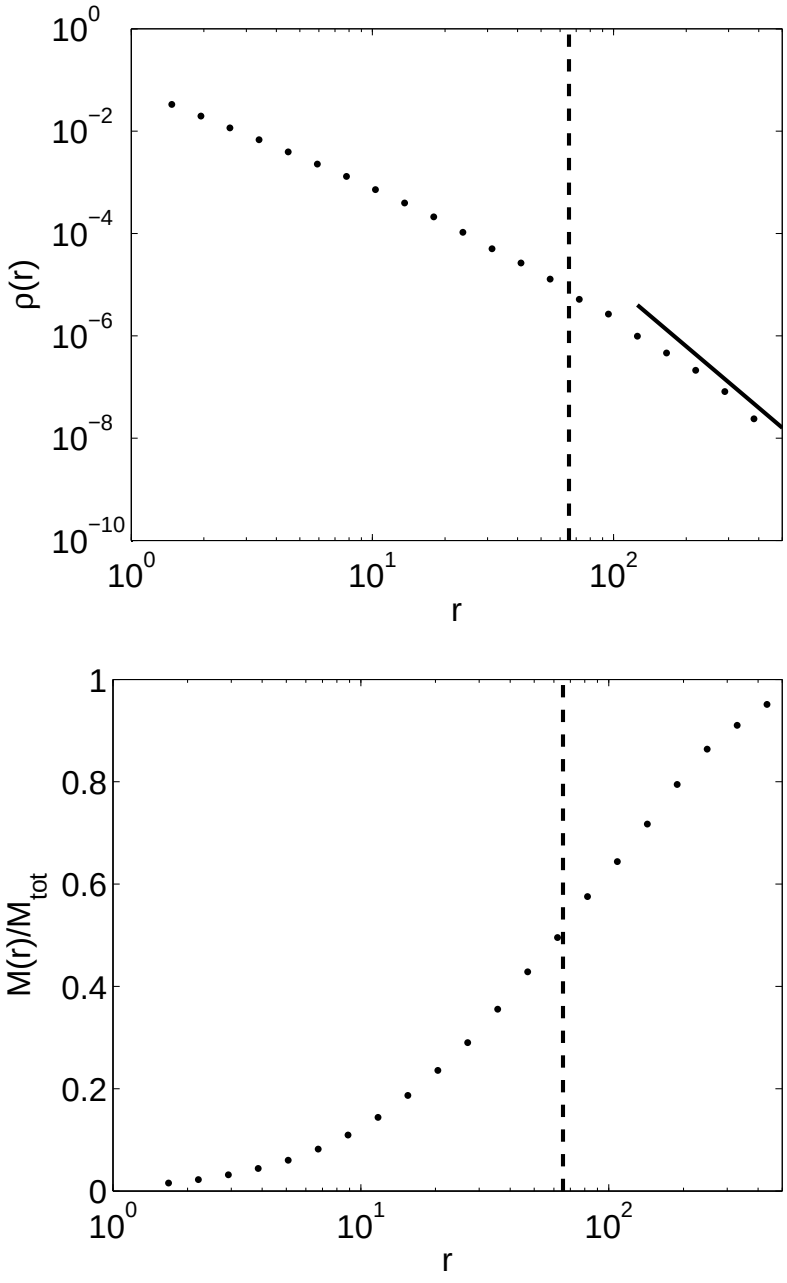

Figure 7.2.—: (Continued).

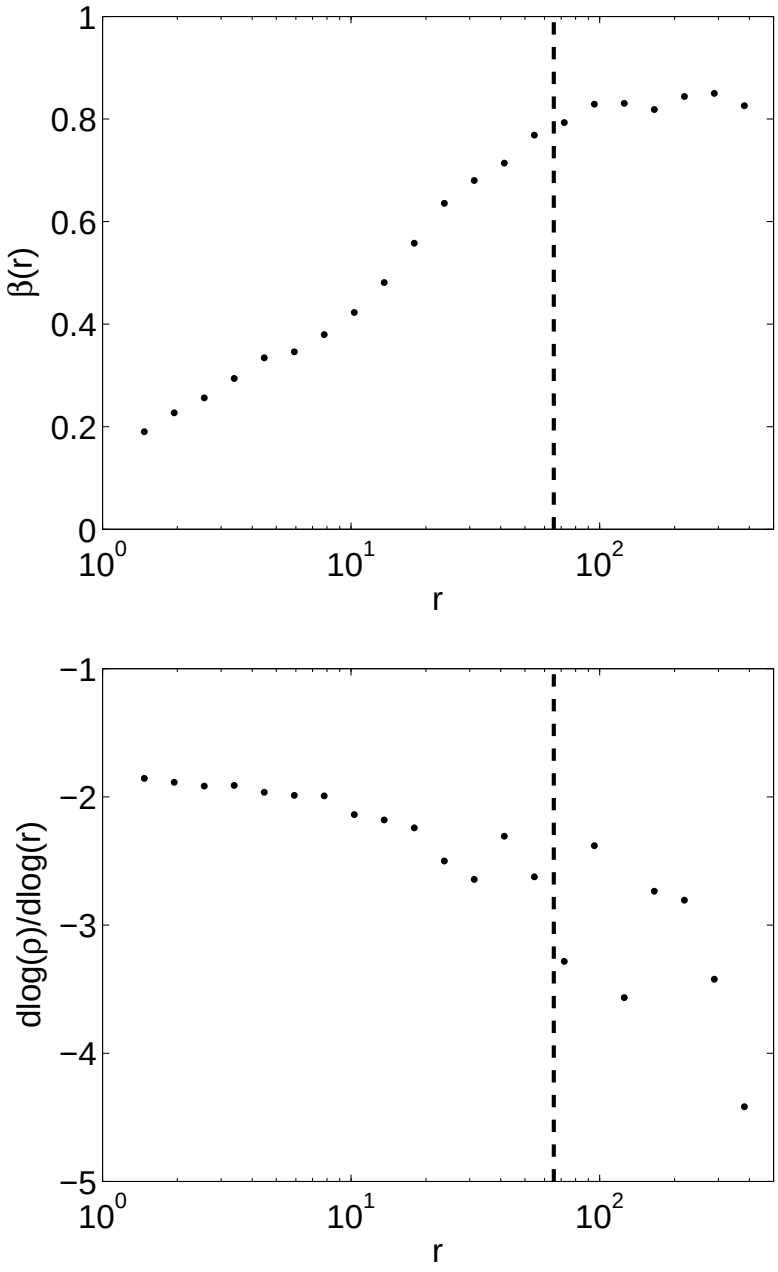

Figure 7.2.—: (Continued).

Initially the system has mainly radial orbits (as in the first numerical experiment). However, in response to small non-radial perturbations, purely radial orbits are dynamically unstable. The system achieves a different equilibrium in which the orbits in the inner regions are isotropic, but those in the outer regions, where the system is not strongly self-gravitating, are still mainly radial. Roughly, the transition occurs at the half-mass radius of the new configuration. This is shown in Figure 7.2, where we plot the radial profile of the anisotropy parameter,

$$\beta(r) = 1 - \frac{\sigma_t(r)^2}{2\sigma_r(r)^2}, \tag{7.6}$$

where $\sigma_r(r)^2$ and $\sigma_t(r)^2$ are, respectively, the radial and the tangential variance in the velocity as a function of radius ($\beta = 0$ corresponds to isotropic and $\beta = 1$ to radial). In the final state, the system has an inner density profile shallower than r^{-2}, but the outer regions are unchanged compared to the purely radial case, still having $\rho \propto r^{-4}$. The particles in this outer region (well outside the half-mass radius) respond to the gravitational potential dictated by the inner region, and their orbits are therefore stable. The inner core (inside the half mass radius), on the other hand, is self-gravitating and subject to the ROI. The resulting central density cusp is now more similar to those which characterize CDM halos and the deprojected $R^{1/4}$ law, supporting the notion that CDM halos and elliptical galaxies are shaped by similar processes.

As further evidence of the relationship between the physics of gravitational collapse in this example and CDM halos we observe that the pseudo-phase-space density of the final state scales roughly as $\rho/\sigma^3 \propto r^{-1.875}$, matching that in halos from cosmological simulations (Navarro et al. 2010). This is plotted in Figure 7.3. We also find that the velocity anisotropy profile scales roughly as $\beta(r) \propto \ln(r)$ near the center, qualitatively

similar to that seen in halos from cosmological N-body simulations.

7.5 A Distribution Function for the Relaxed System

The numerical experiments and analytic arguments presented in the preceding sections have led us to propose a simple scenario for how collisionless systems are formed through gravitational collapse. The outer profile is determined by the redistribution of energy among particles through violent-relaxation, which promotes a small fraction of the mass onto unbound orbits. If no further infall occurs, the density profile will asymptote to $\rho \propto r^{-4}$ as predicted by White (1987) and Jaffe (1987). If infall has not halted, the system will not be in equilibrium and a different density profile may be measured at large radii. For a nearly radial infall, the ROI will operate causing the system to evolve such that the inner region is characterized by orbit isotropy and a density profile shallower than $\rho \propto r^{-2}$ (not permitted in the purely radial case). If the collapsing particles initially have significant non-radial motions, the final profile will be even shallower.

To understand the physical nature of systems formed through this scenario, we have performed an analysis of the phase-space distribution of the final state in the numerical example of Section 7.4. Note that because the system is anisotropic, the DF cannot be expressed as a function of energy alone. We propose the following form of the DF (guided by Gerhard (1991)),

$$f(E, L) = f(E, x) = g(E)h(x, E), \tag{7.7}$$

where $x = L/L_c(E)$ is the angular momentum divided by the angular momentum of a particle on a circular orbit with energy E. The values of x range between 0 and 1. The

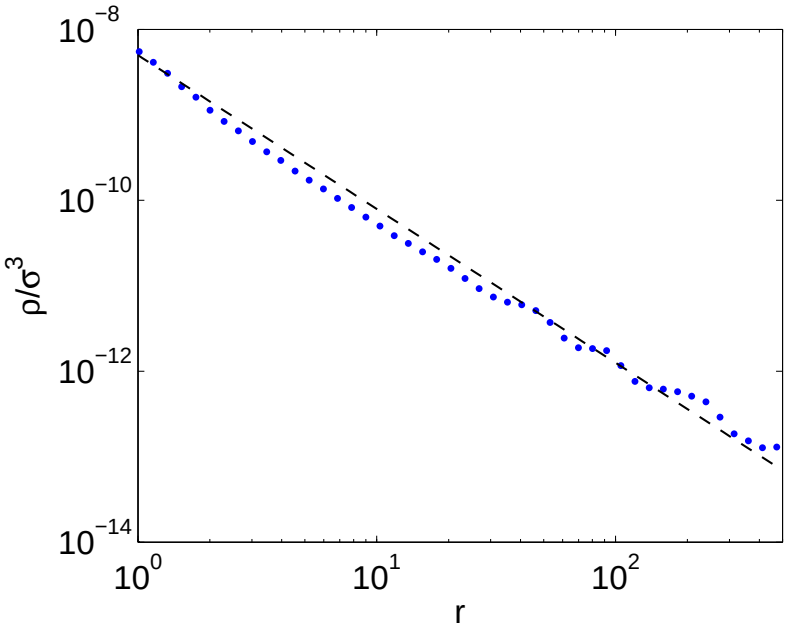

Figure 7.3.—: The pseudo-phase-space density, ρ/σ^3, of the final state of the collapse simulation described in Section 7.4 (points). For reference we plot $\rho/\sigma^3 \propto r^{-1.875}$, which is found in CDM halos from cosmological N-body simulations.

functions g and h are given by

$$g(E) = A \exp(-\beta_E E)(-E)^c, \tag{7.8}$$

and

$$h(x, E) = \exp(-x^2/q(E)^2), \tag{7.9}$$

where A, β_E, and c are free parameters. We expect $q(E)$ to be a function which increases with $|E|$ and parameterize it with a broken power law as explained below.

This model's main features can be explained in terms of the collapse scenario described above. The function $h(x, E)$ determines how anisotropic orbits of a given energy are, with a delta function in x corresponding to purely radial and a constant function corresponding to isotropic. We expect that $q(E)$ gets larger for increasing $|E|$ such that $h(x, E)$ transitions from a delta function for the least tightly bound particles to a constant for the most tightly bound particles. The most tightly bound particles are those which make up the inner profile and have been isotropized through the ROI, while the more weakly bound particles are unaffected by this instability and are found mostly in the outskirts of the system on radial orbits. The energy dependence of the DF in equation (7.8) is a Maxwellian distribution for large $|E|$, but modified by the factor $(-E)^c$ for the least tightly bound particles. We can interpret this as a Gaussian distribution (representing a favorable statistical state), modified at high energies due to particles being scattered into unbound orbits. The values of the parameters in our model can also be related to the bulk properties of the system. Our expectation is that the parameter $1/\beta_e$ is of the order of the kinetic energy per particle. The transition in $q(E)$ which changes $h(x, E)$ from a delta function to a constant should happen roughly at the mean energy of particles found at the half-mass radius of the system. This corresponds

to the notion that the ROI isotropizes roughly the inner half of the system and leaves the outer envelope, which is not strongly self-gravitating, mostly radial.

We compare the DF measured directly from the simulation with a parameterization of this model. Values of $c = 0.9275$ and $\beta_E = 4 \times 10^{-5}$ are found to match the simulation well (see Figure 7.4). As expected, the value of β_E also corresponds roughly to the reciprocal of the mean kinetic energy, $\bar{v}^2/2 = 10^4$. For $q(E)$ we use a broken power law of the form $q(E) = a(-E)^b$. For $\ln(-E) < 9.55$, $a = 0.00012$ and $b = 0.87$, while for $9.55 < \ln(-E) < 11.9$, $a = 0.07$ and $b = 0.21$. When $\ln(-E) > 11.9$, we assume $a = 4 \times 10^{-11}$ and $b = 2$. This was determined by fitting for $q(E)$ separately in each energy bin and then using the power law as a simple way to parameterize the values. This procedure provides a reasonably good match to the simulation data and has the limiting behavior we expect for high and low E. We compare contours of the DF, $f(E, L)$, from the simulation and this parameterization of the model in Figure 7.4. Clearly, there is very good agreement.

Figure 7.4.—: A comparison of the DF from the N-body simulation of gravitational collapse described in Section 7.4 and the model DF described in Section 7.5. We plot contours of the DF, $\log(f(E, L))$, from the simulation (first page top panel) and the parameterized model (first page bottom panel). We plot $g(E)$, given by equation (7.8), for the simulation data (blue points) and the model (dashed line). We also plot $h(x, E = -3.8 \times 10^4)$, given by equation (7.9). The values for the model parameters are listed in the main text.

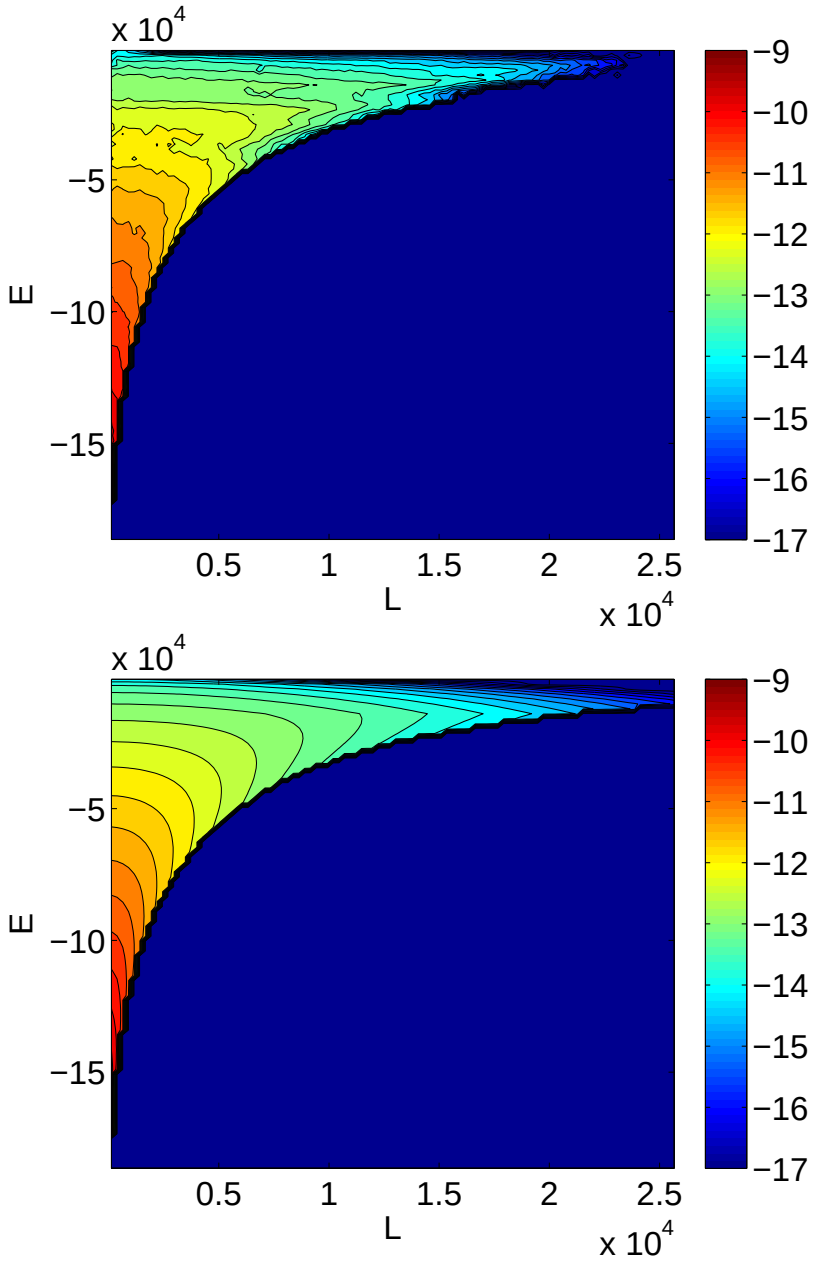

Figure 7.4.—: (Continued).

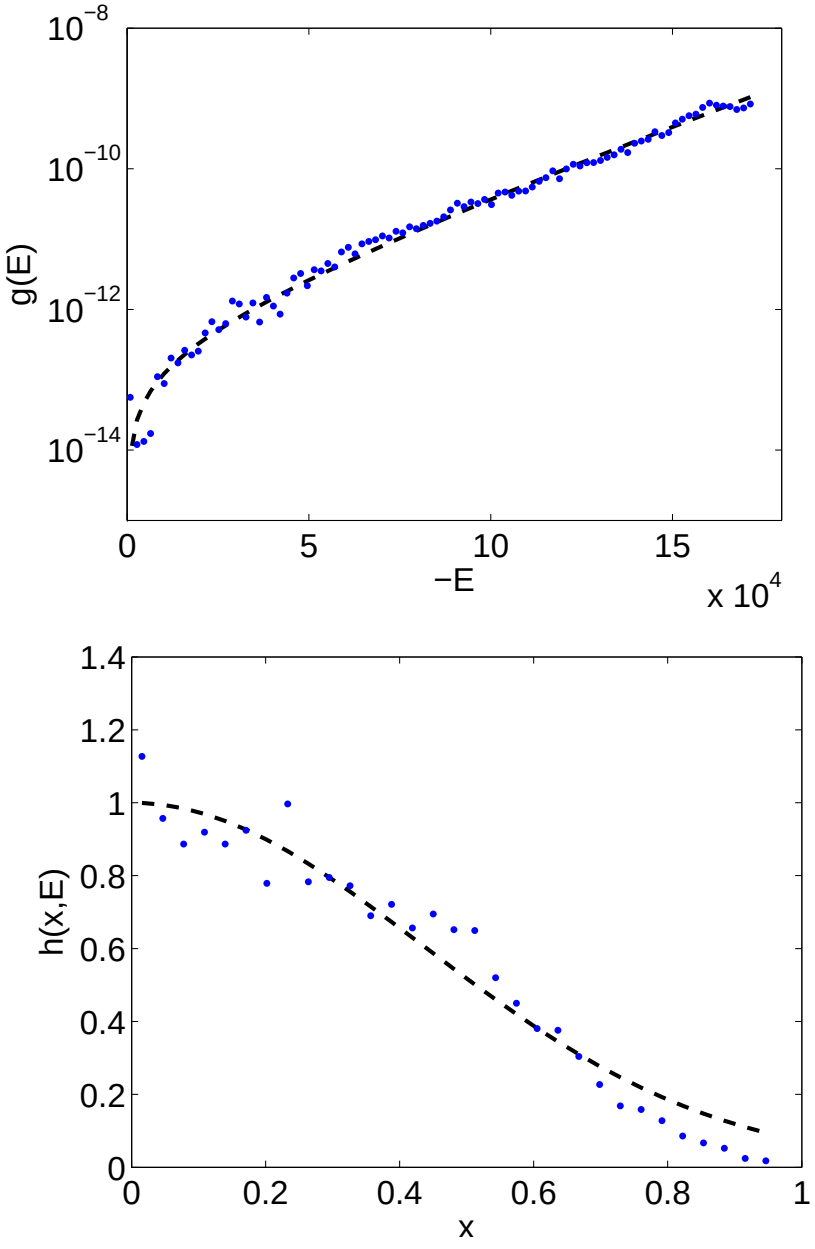

Figure 7.4.—: (Continued).

In addition to fitting the phase-space data from the numerical experiment we also take this DF parameterization and self-consistently compute the density and anisotropy profiles of the system. This was accomplished iteratively with the following expression:

$$\rho_{n+1}(r) = \int d^3\vec{v} f(E = v^2/2 + \Phi(r), L = v_t r), \tag{7.10}$$

where the gravitational potential $\Phi(r)$ is computed using the density from the previous step, ρ_n. At each step the normalization of the DF is set to fix the innermost value of $\rho(r)$ to a constant value. We use the density profile from the simulation as $\rho(r)_1$ and iterate until the profile has converged to values where $\rho(r)_n = \rho(r)_{n+1}$. In Figure 7.5, we show the results of this procedure and find good agreement with the density and anisotropy profiles measured from the simulation. Note that we have not searched the parameter space for the best match between profiles. We simply used the same parameters described above. A better match would be obtained if we searched explicitly for the values of c, β_E, and the $q(E)$ power law parameters which minimize the density profile discrepancy. More flexible functions of $q(E)$ could also improve the fit.

That a relatively simple form of the DF matches the results of our numerical experiments so well justifies the notion that there is favored outcome through gravitational collapse. A similar outcome should apply to all systems formed through radial dissipationless gravitational collapse, including CDM halos and elliptical galaxies.

7.6 Comparison with previous work

There has been much work attempting to understand the physical nature of the nearly universal density profiles of CDM halos found in cosmological N-body simulations. Next

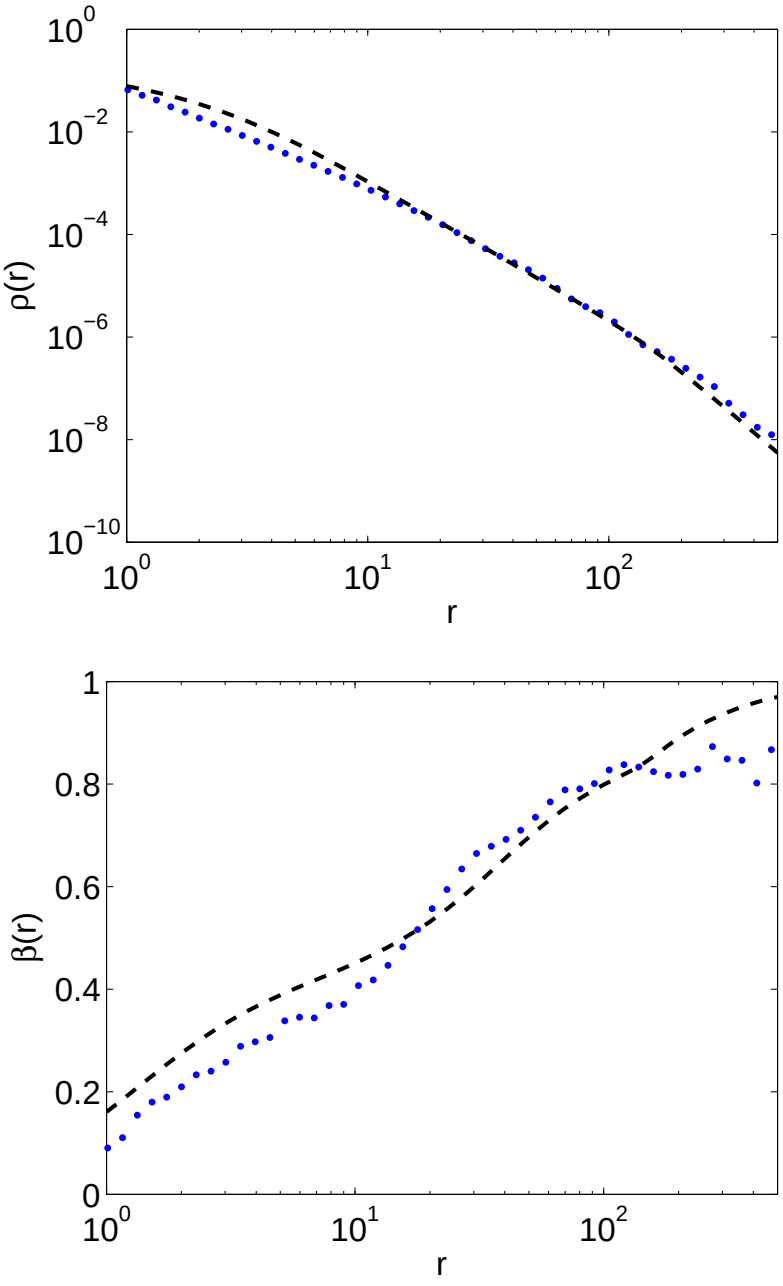

Figure 7.5.—: A comparison between the numerical simulation described in Section 7.4 and the model DF described in Section 7.5. We plot the density profile (top panel) and the velocity anisotropy (bottom panel) from the simulation (blue points) and the values implied by the model DF (dashed lines). The values for the model parameters used are listed in the main text.

we summarize much of this work and explain how it relates to the present paper.

One popular way of analytically modeling CDM halo formation is through so-called secondary infall (SI) models. This work began with Gunn & Gott (1972b), who studied how mass shells accrete onto a collapsed object. Later, by imposing self-similar and radial orbits Bertschinger (1985) and Fillmore & Goldreich (1984) were able to derive the inner profile of a halo as a function of the density profile of the initial perturbation. More recently, there have been a number of improvements to these models which include angular momentum (Zukin & Bertschinger 2010a,b) and generalize to fully 3D solutions (Lithwick & Dalal 2011), including numerical simulations (Vogelsberger et al. 2011). Note that much like our example in Section 7.2, the purely radial SI models produce halos which have steeper central profiles than those observed in cosmological simulations. Models which include non-radial velocities are able to produce NFW or Einasto-like profiles. However, they contain a number of non-physical assumptions to make the problem tractable, such as spherical symmetry or assuming that all particles in a given mass shell have the same velocity. In this paper, we argue that much of the physics which determines the density profiles of CDM halos is unrelated to cosmology. The details related to cosmological expansion and accretion included in SI modeling may obscure the important physics. Thus, our work compliments the SI approach by identifying what aspects of the equilibrium state do not depend on cosmology.

Other work focusing on the cosmological context has investigated how the hierarchical assembly of halos affects the density profile. Huss et al. (1999) found that a variety of different initial conditions, including simple monolithic collapse produce similar density profiles. Wang & White (2009) find that cosmological hot dark matter (HDM) simulations produce similar profiles to CDM halos, implying that the mergers

due to increased substructure in a CDM cosmology are not important to structuring density profiles. This is also supported by the simulations of Kazantzidis et al. (2006), who find that the shape of density profiles are preserved during major mergers of halos in N-body simulations, and earlier work by Hernquist (1992, 1993); Barnes & Hernquist (1996) who showed that density profiles similar to those described here arise naturally in mergers of individual galaxies. All of this work supports the idea presented in this paper, that the shape of CDM halos is due to physical principles common to collapsing systems rather than depending on the details of initial conditions or cosmology.

It has also been observed in cosmological simulations that the outer portions of CDM halo density profiles depend on the cosmological model. For example the outskirts of halos simulated with vacuum boundary conditions have profiles steeper than the NFW profile (Dubinski & Carlberg 1991). In the future of a ΛCDM universe, halos are steeper than the NFW parameterization at large radius and are truncated due to the acceleration caused by dark energy (Busha et al. 2005). We note that the analytic prediction of $\rho \propto r^{-4}$ breaks down at large radii in this case since the binding energy of particles is affected by dark energy. That the outer profile is affected by cosmology supports our claim that the $\rho \propto r^{-3}$ asymptotic limit in the NFW profile is a consequence of the cosmological background density and continued accretion and not due to the primary physics which determines the profile.

We argue that the ROI is a key physical process which determines the shape of CDM halo density profiles. This has been proposed by a number of other authors and the ROI has been explored both within N-body simulations (Bellovary et al. 2008; MacMillan et al. 2006) and semi-analytic models (Barnes et al. 2005). We extend these studies by proposing a form of the DF motivated by a physical scenario of gravitational collapse

including the ROI. A different form of the DF to describe objects formed through gravitational collapse was put forward by Trenti & Bertin (2005) and Trenti et al. (2005). This DF was determined by maximizing entropy subject to a constraint involving an integral of the angular momentum and the energy. This model generates density and velocity anisotropy profiles similar to those found in N-body simulations, but has a feature which does not match in the detailed form of $f(E, L)$. Another relevant paper is Merritt et al. (2005), where they point out, as we have, that elliptical galaxy and CDM halo profiles can both be fit by similar parameterizations (namely the Einasto profile or Sersic model). In this paper we have attempted to better explain this connection by studying a new form of the DF which better matches simulations.

7.7 Conclusions

The similarity between the density profiles of CDM halos and elliptical galaxies suggests that their formation can be understood in terms of the same physical processes. This leads us to propose that the features of CDM halo density profiles result, to a large extent, from the physics of gravitational collapse of collisionless systems. In this paper, the first in a series, we studied these dynamics by exploring a toy-model, the collapse of a perfectly cold Plummer sphere.

Using analytic arguments and two numerical experiments, we demonstrated that the final equilibrium state of our Plummer model collapse can be understood in fairly simple terms. In the first experiment, we ran an N-body simulation of collapse with the particles constrained to radial orbits. In the final state, we have found an inner density profile which is slightly steeper than $\rho \propto r^{-2}$ and an outer profile which scales as $\rho \propto r^{-4}$.

Simple analytic arguments explain these asymptotic profiles. In the second experiment, we relaxed the radial orbit constraint. Here we have found the same outer equilibrium profile, but a shallower inner profile, which we attribute to isotropization introduced by the ROI in the self-gravitating core of the halo.

We are led to a relatively simple scenario for the formation of objects through radial gravitational collapse. Initially violent-relaxation scatters some particles to unbound orbits and the remaining weakly bound particles form the outer density profile, which scales as r^{-4} due to the argument of Jaffe (1987) and White (1987). These particles are not strongly self-gravitating and thus remain on mostly radial orbits. The inner profile is strongly self-gravitating and becomes isotropic through the onset of ROI resulting in a profile shallower than $\rho \propto r^{-2}$, like those observed in elliptical galaxies and CDM halos.

We present a form of the DF which matches the final state of our collapse simulation. The main features of this model can be related to our physical picture of collapse; weakly bound (large radii) particles are on radial orbits and tightly bound (small radii) particles have isotropic velocities. This is captured with a term that describes how circular orbits are as a function of energy, $h(x, E)$. These simple considerations are combined with a roughly Maxwellian energy dependence term, which is a natural expectation based on statistical arguments. Our model self-consistently reproduces the density and anisotropy profiles obtained from our simulations. The parameters in the model can also be related to the bulk properties of the system.

The simple parameterization of the DF motivates a universal form for density profiles created through this process. However, non-radial velocities in the initial conditions of collapse may alter the inner profile, making it shallower than we find in our

numerical experiments. Continued cosmological infall and accretion could also have some effect. These factors may make the inner profiles of CDM halos sensitive to cosmological parameters in detail. Since the outer profile of an object created through gravitational collapse is predicted to scale as $\rho \propto r^{-4}$, the shallower profile in CDM halos must be due to ongoing cosmological accretion and the presence of the cosmological background.

As evidence for the connection between our toy-model and CDM halos we find that they both have the same power law for the pseudo-phase-space density, $\rho/\sigma^3 \propto r^{-1.875}$. We also note that at small radii, CDM halos have an anisotropy profile, $\beta(r)$, which is similar to our collapse model (Navarro et al. 2010).

The physical picture presented in this paper provides predictions for CDM halos which can readily be tested. First, there is no "universal" form of the CDM halos in the Universe. Instead, the outer halo is altered by accretion and therefore will depend on background density. In principle, a halo in a sufficiently under-dense region will behave as if it is in an open-universe, causing accretion to halt at earlier epochs allowing the halo to equilibrate to the $\rho \propto r^{-4}$ form. Another prediction is that the final state of halos may have DFs which resemble those from our collapse simulation. We will test these predictions in paper 2 (in preparation) and further investigate how the physics of dissipationless collapse and effects from the cosmological environment combine to produce the CDM halo density profiles seen in N-body simulations.

Acknowledgments

We thank Mark Vogelsberger for useful conversations. This work was supported in part by NSF grant AST-0907890 and NASA grants NNX08AL43G and NNA09DB30A.

7.8 Appendix: Distribution Function of the Radial Jaffe Profile

The distribution function (DF) for a system of purely radial orbits can be written as

$$f(\vec{x},\vec{v}) = g(\mathcal{E})\delta^D(L^2), \tag{7.11}$$

where $\mathcal{E} \equiv -E$ and δ^D is a Dirac delta function. We derive $g(\mathcal{E})$ for a Jaffe density profile with scale length a and density parameter ρ_0,

$$\rho(r) = \frac{\rho_0}{(r/a)^2(1+r/a)^2}. \tag{7.12}$$

We begin with

$$\rho(r) = \int d^3\vec{v} f(\vec{x},\vec{v}) = \int dv_r \frac{g(\mathcal{E})}{r^2}, \tag{7.13}$$

where v_r is the radial velocity. We then perform a change of variables to obtain

$$\tilde{\rho}(r) = \int_0^\Psi \frac{d\mathcal{E}\, g(\mathcal{E})}{\sqrt{\Psi - \mathcal{E}}}, \tag{7.14}$$

where we have defined $\tilde{\rho}(r) \equiv \sqrt{2}\rho(r)r^2$ and $\Psi \equiv -\Phi$. Using the Abel integral equation (see Appendix B in Binney & Tremaine (2008)), we can solve for $g(\mathcal{E})$,

$$g(\mathcal{E}) = \frac{1}{\pi}\left[\int_0^\mathcal{E} \frac{d\Psi}{\sqrt{\mathcal{E}-\Psi}}\frac{d\tilde{\rho}}{d\Psi} + \frac{\tilde{\rho}(\Psi=0)}{\sqrt{\mathcal{E}}}\right]. \tag{7.15}$$

Since Ψ is a monotonic function of r we are able to use $\tilde{\rho}$ as a function of Ψ,

$$\tilde{\rho}(\Psi) = \sqrt{2}\rho_0 a^2 e^{-2\tilde{\Psi}} \left(e^{\tilde{\Psi}} - 1\right)^2, \tag{7.16}$$

where $\tilde{\Psi} = \Psi/(4\pi\rho_0 a^2 G)$. Evaluating the integral in equation (7.15) we obtain,

$$g(\mathcal{E}) = \frac{2a}{\pi^{3/2}}\sqrt{\frac{\rho_0}{G}}\left[\sqrt{2}D\left(\sqrt{\frac{\mathcal{E}}{4\pi a^2\rho_0 G}}\right) - D\left(\sqrt{\frac{\mathcal{E}}{2\pi a^2\rho_0 G}}\right)\right], \tag{7.17}$$

where $D(x)$ is the Dawson function.

Chapter 8

Conclusions and Future Directions

There are a number of exciting unresolved topics in cosmology and the high-redshift universe, including the formation and evolution of the first galaxies and the time and details of reionization. The research presented above addresses these topics by improving theoretical models and identifying promising directions for future observations.

In Chapters 2 and 3, we propose intensity mapping of spectral lines besides the 21cm line of neutral hydrogen. This new observational technique can be used measure the global properties of high-redshift galaxy populations that are too faint to be directly observed. Since the publication of this work, interest in this approach has grown substantially. Additional theoretical research has focused on the CO, CII, and Lyman-α lines from galaxies during the epoch of reionization (e.g. Lidz et al. 2011; Carilli 2011; Gong et al. 2011, 2012; Silva et al. 2013). There is also interest among observers in building dedicated instruments (personal communication Judd Bowman 2012). As a first step in computing the expected intensity mapping signal, we calibrated the line luminosity of high-redshift galaxies empirically with observations of nearby galaxies.

Additional theoretical work is necessary to predict the signal from first principles, which will be very important for interpreting future measurements.

Chapter 4 contains a forecast of how well futuristic 21cm intensity mapping instruments could constrain cosmological parameters. We find that these observations could greatly improve constraints from Planck alone. Currently several groups are working to perform the first 21cm intensity mapping measurements (e.g. Chang et al. 2010). This technique promises to be an extremely sensitive probe of cosmology.

In Chapter 5, we describe a semi-numerical technique to compute the reionization history when X-rays, from sources such as active galactic nuclei, provide a significant ionization contribution. We find that the kSZ component of the CMB power spectrum is reduced, due to the smoother topology of reionization introduced by X-rays. Unfortunately, the sensitivity of SPT and ACT are not sufficient to distinguish the different models of reionization we explore. However, a non-detection of the patchy reionization signal with these instruments could suggest that X-rays played an important role. Upcoming radio observations of redshifted 21cm emission from reionization could also reveal the impact X-rays (Warszawski et al. 2009). Future work will check (and potentially improve) our semi-analytic prescription by comparing with full cosmological simulations which include radiative transfer.

In Chapter 6, we demonstrate the impact of the newly discovered relative velocity between baryons and dark matter on the 3-dimensional distribution of the first stars. We find that the relative velocity may increase the amplitude of fluctuations in the 21cm signal at a redshift of $z = 20$, making the signal easier to observe than previously expected. Because individual sources are very distant, this may be the most promising

way of studying the first generation of stars. While our simulations are an important step in modeling the pre-reionization 21cm signal, much work remains. The signal depends on a number of different physical parameters including the star formation efficiency and the spectral properties of X-ray sources. We have only tested one set of values for these parameters. Moving forward, it will be important to explore the entire parameter space of realistic possibilities. We have assumed that star formation in small dark matter halos is possible via molecular hydrogen cooling. Once Lyman-Werner radiation dissociates molecular hydrogen, star formation can only proceed in larger dark matter halos where the relative velocity effect has a much smaller impact. We have started to investigate the possible impact Lyman-Werner radiation in detail (Fialkov et al. 2012b), but improved numerical simulations are needed for more robust predictions.

In Chapter 7, we present (non-cosmological) N-body simulations of dissipationless gravitational collapse in an effort to understand the physics that sets the density profiles of dark matter halos. We find some interesting similarities with the final equilibrium states of our simulations and dark matter halos found in the cosmological context. In particular, we find a very similar form of the pseudo-phase-space density, $\rho/\sigma^3 \propto r^{-1.875}$. We also propose a new form of the distribution function, based on a simple physical picture of gravitational collapse, which fits the final states of our simulations. The similarities between our simulations and dark matter halos is intriguing, but future work that compares these results directly with cosmological simulations is necessary to better understand the connection.

References

Abel, T., Bryan, G. L., & Norman, M. L. 2002, Science, 295, 93

Ahn, K., & Shapiro, P. R. 2007, MNRAS, 375, 881

Aihara, H., et al. 2011, ApJS, 193, 29

Anderson, L., et al. 2012, MNRAS, 427, 3435

Arnouts, S., et al. 2005, ApJ, 619, L43

Babich, D., & Loeb, A. 2006, ApJ, 640, 1

Barkana, R., Haiman, Z., & Ostriker, J. P. 2001, ApJ, 558, 482

Barkana, R., & Loeb, A. 2001, Phys. Rep., 349, 125

—. 2004, ApJ, 609, 474

—. 2005a, ApJ, 624, L65

—. 2005b, ApJ, 626, 1

—. 2007, Reports on Progress in Physics, 70, 627

Barnes, E. I., Williams, L. L. R., Babul, A., & Dalcanton, J. J. 2005, ApJ, 634, 775

Barnes, J., Hut, P., & Goodman, J. 1986, ApJ, 300, 112

Barnes, J. E., & Hernquist, L. 1996, ApJ, 471, 115

Barnes, L. A., & Haehnelt, M. G. 2009, MNRAS, 397, 511

Bellovary, J. M., Dalcanton, J. J., Babul, A., Quinn, T. R., Maas, R. W., Austin, C. G., Williams, L. L. R., & Barnes, E. I. 2008, ApJ, 685, 739

Bernardi, G., et al. 2010, A&A, 522, A67

Bertschinger, E. 1985, ApJS, 58, 39

Bharadwaj, S., & Ali, S. S. 2004, MNRAS, 352, 142

Binney, J., & Merrifield, M. 1998, Galactic Astronomy

Binney, J., & Tremaine, S. 2008, Galactic Dynamics

Bond, J. R., Cole, S., Efstathiou, G., & Kaiser, N. 1991, ApJ, 379, 440

Bouwens, R. J., Illingworth, G. D., Franx, M., & Ford, H. 2007, ApJ, 670, 928

Bouwens, R. J., et al. 2011a, Nature, 469, 504

—. 2011b, ApJ, 737, 90

—. 2012, ApJ, 752, L5

Bowman, J. D., Morales, M. F., & Hewitt, J. N. 2006, ApJ, 638, 20

—. 2009, ApJ, 695, 183

Bradford, C. M., et al. 2009, in Astronomical Society of the Pacific Conference Series, Vol. 417, Submillimeter Astrophysics and Technology: a Symposium Honoring Thomas G. Phillips, ed. D. C. Lis, J. E. Vaillancourt, P. F. Goldsmith, T. A. Bell, N. Z. Scoville, & J. Zmuidzinas, 341

Bromm, V., Coppi, P. S., & Larson, R. B. 1999, ApJ, 527, L5

Bullock, J. S., Wechsler, R. H., & Somerville, R. S. 2002, MNRAS, 329, 246

Busha, M. T., Evrard, A. E., Adams, F. C., & Wechsler, R. H. 2005, MNRAS, 363, L11

Carilli, C. L. 2011, ApJ, 730, L30

Chang, T.-C., Pen, U.-L., Bandura, K., & Peterson, J. B. 2010, Nature, 466, 463

Chang, T.-C., Pen, U.-L., Peterson, J. B., & McDonald, P. 2008, Physical Review Letters, 100, 091303

Colless, M., et al. 2001, MNRAS, 328, 1039

Cooray, A., & Sheth, R. 2002, Phys. Rep., 372, 1

Curran, S. J., Tzanavaris, P., Murphy, M. T., Webb, J. K., & Pihlström, Y. M. 2007, MNRAS, 381, L6

Dalal, N., Lithwick, Y., & Kuhlen, M. 2010a, ArXiv e-prints: 1010.2539

Dalal, N., Pen, U.-L., & Seljak, U. 2010b, JCAP, 11, 7

Datta, A., Bowman, J. D., & Carilli, C. L. 2010, ApJ, 724, 526

Davies, J. I., de Blok, W. J. G., Smith, R. M., Kambas, A., Sabatini, S., Linder, S. M., & Salehi-Reyhani, S. A. 2001, MNRAS, 328, 1151

Dubinski, J., & Carlberg, R. G. 1991, ApJ, 378, 496

Efstathiou, G. 1992, MNRAS, 256, 43P

Faucher-Giguère, C.-A., Lidz, A., Hernquist, L., & Zaldarriaga, M. 2008, ApJ, 688, 85

Fialkov, A., Barkana, R., Tseliakhovich, D., & Hirata, C. M. 2012a, MNRAS, 424, 1335

Fialkov, A., Barkana, R., Visbal, E., Tseliakhovich, D., & Hirata, C. M. 2012b, ArXiv e-prints: 1212.0513

Fillmore, J. A., & Goldreich, P. 1984, ApJ, 281, 1

Fixsen, D. J., Dwek, E., Mather, J. C., Bennett, C. L., & Shafer, R. A. 1998a, ApJ, 508, 123

—. 1998b, ApJ, 508, 123

Furlanetto, S. R., & Loeb, A. 2002, ApJ, 579, 1

Furlanetto, S. R., Oh, S. P., & Briggs, F. H. 2006a, Phys. Rep., 433, 181

—. 2006b, Phys. Rep., 433, 181

Furlanetto, S. R., & Stoever, S. J. 2010, MNRAS, 404, 1869

Gardner, J. P., et al. 2006, Space Sci. Rev., 123, 485

Gerhard, O. E. 1991, MNRAS, 250, 812

Gong, Y., Cooray, A., Silva, M., Santos, M. G., Bock, J., Bradford, C. M., & Zemcov, M. 2012, ApJ, 745, 49

Gong, Y., Cooray, A., Silva, M. B., Santos, M. G., & Lubin, P. 2011, ApJ, 728, L46

Goobar, A., Hannestad, S., Mörtsell, E., & Tu, H. 2006, JCAP, 6, 19

Graham, A. W., & Guzmán, R. 2003, The Astronomical Journal, 125, 2936

Greif, T. H., White, S. D. M., Klessen, R. S., & Springel, V. 2011, ApJ, 736, 147

Gruzinov, A., & Hu, W. 1998, ApJ, 508, 435

Gunn, J. E., & Gott, III, J. R. 1972a, ApJ, 176, 1

—. 1972b, ApJ, 176, 1

Haiman, Z., Abel, T., & Rees, M. J. 2000a, ApJ, 534, 11

—. 2000b, ApJ, 534, 11

Haiman, Z., Rees, M. J., & Loeb, A. 1997a, ApJ, 476, 458

—. 1997b, ApJ, 476, 458

Harker, G., et al. 2010, MNRAS, 405, 2492

Heitmann, K., Higdon, D., White, M., Habib, S., Williams, B. J., Lawrence, E., & Wagner, C. 2009, ApJ, 705, 156

Heitmann, K., White, M., Wagner, C., Habib, S., & Higdon, D. 2010, ApJ, 715, 104

Hernquist, L. 1990, ApJ, 356, 359

—. 1992, ApJ, 400, 460

—. 1993, ApJ, 409, 548

Holzbauer, L. N., & Furlanetto, S. R. 2012, MNRAS, 419, 718

Hui, L., & Gnedin, N. Y. 1997, MNRAS, 292, 27

Huss, A., Jain, B., & Steinmetz, M. 1999, ApJ, 517, 64

Iliev, I. T., Pen, U.-L., Bond, J. R., Mellema, G., & Shapiro, P. R. 2007, ApJ, 660, 933

Jaffe, W. 1987, in IAU Symposium, Vol. 127, Structure and Dynamics of Elliptical Galaxies, 511

Jelić, V., et al. 2008, MNRAS, 389, 1319

Johnson, J. L., Greif, T. H., & Bromm, V. 2007, ApJ, 665, 85

Jungman, G., Kamionkowski, M., Kosowsky, A., & Spergel, D. N. 1996, Phys. Rev. D, 54, 1332

Kaiser, N. 1987, MNRAS, 227, 1

Kanekar, N., & Chengalur, J. N. 2003, A&A, 399, 857

Kazantzidis, S., Zentner, A. R., & Kravtsov, A. V. 2006, ApJ, 641, 647

Kennicutt, Jr., R. C. 1998, ARA&A, 36, 189

Knox, L., Scoccimarro, R., & Dodelson, S. 1998, Physical Review Letters, 81, 2004

Komatsu, E., et al. 2011, ApJS, 192, 18

Kosowsky, A. 2003, New Astronomy Reviews, 47, 939

Kravtsov, A. V., Berlind, A. A., Wechsler, R. H., Klypin, A. A., Gottlöber, S., Allgood, B., & Primack, J. R. 2004, ApJ, 609, 35

Lidz, A., Furlanetto, S. R., Oh, S. P., Aguirre, J., Chang, T.-C., Doré, O., & Pritchard, J. R. 2011, ApJ, 741, 70

Lithwick, Y., & Dalal, N. 2011, ApJ, 734, 100

Liu, A., & Tegmark, M. 2011, Phys. Rev. D, 83, 103006

—. 2012, MNRAS, 419, 3491

Liu, A., Tegmark, M., Bowman, J., Hewitt, J., & Zaldarriaga, M. 2009, MNRAS, 398, 401

Loeb, A. 2008, JCAP, 4, 21

Loeb, A. 2010, How Did the First Stars and Galaxies Form?

Loeb, A., Barkana, R., & Hernquist, L. 2005, ApJ, 620, 553

Loeb, A., & Wyithe, J. S. B. 2008, Physical Review Letters, 100, 161301

Lynden-Bell, D. 1967, MNRAS, 136, 101

Machacek, M. E., Bryan, G. L., & Abel, T. 2001, ApJ, 548, 509

MacMillan, J. D., Widrow, L. M., & Henriksen, R. N. 2006, ApJ, 653, 43

Madau, P., Meiksin, A., & Rees, M. J. 1997, ApJ, 475, 429

Madau, P., Rees, M. J., Volonteri, M., Haardt, F., & Oh, S. P. 2004, ApJ, 604, 484

Maio, U., Koopmans, L. V. E., & Ciardi, B. 2011, MNRAS, 412, L40

Malhotra, S., et al. 2001, ApJ, 561, 766

Mao, Y., Tegmark, M., McQuinn, M., Zaldarriaga, M., & Zahn, O. 2008, Phys. Rev. D, 78, 023529

McQuinn, M., Furlanetto, S. R., Hernquist, L., Zahn, O., & Zaldarriaga, M. 2005, ApJ, 630, 643

McQuinn, M., Zahn, O., Zaldarriaga, M., Hernquist, L., & Furlanetto, S. R. 2006a, ApJ, 653, 815

—. 2006b, ApJ, 653, 815

Merritt, D., & Aguilar, L. A. 1985, MNRAS, 217, 787

Merritt, D., Navarro, J. F., Ludlow, A., & Jenkins, A. 2005, ApJ, 624, L85

Mesinger, A., & Dijkstra, M. 2008, MNRAS, 390, 1071

Mesinger, A., Furlanetto, S., & Cen, R. 2011a, MNRAS, 411, 955

—. 2011b, MNRAS, 411, 955

Mesinger, A., McQuinn, M., & Spergel, D. 2011c, ArXiv e-prints: 1112.1820

Morales, M. F. 2005, ApJ, 619, 678

Morales, M. F., Hazelton, B., Sullivan, I., & Beardsley, A. 2012, ApJ, 752, 137

Naoz, S., & Barkana, R. 2008, MNRAS, 385, L63

Naoz, S., Noter, S., & Barkana, R. 2006, MNRAS, 373, L98

Naoz, S., Yoshida, N., & Gnedin, N. Y. 2012, ApJ, 747, 128

Navarro, J. F., Frenk, C. S., & White, S. D. M. 1996, ApJ, 462, 563

Navarro, J. F., et al. 2010, MNRAS, 402, 21

Oesch, P. A., et al. 2010, ApJ, 725, L150

Oh, S. P., & Mack, K. J. 2003, MNRAS, 346, 871

O'Shea, B. W., & Norman, M. L. 2008, ApJ, 673, 14

Osterbrock, D. E., & Ferland, G. J. 2006, Astrophysics of gaseous nebulae and active galactic nuclei

Panuzzo, P., et al. 2010a, A&A, 518, L37

—. 2010b, A&A, 518, L37

Pen, U.-L., Chang, T.-C., Hirata, C. M., Peterson, J. B., Roy, J., Gupta, Y., Odegova, J., & Sigurdson, K. 2009a, MNRAS, 399, 181

Pen, U.-L., Staveley-Smith, L., Peterson, J. B., & Chang, T.-C. 2009b, MNRAS, 394, L6

Petrovic, N., & Oh, S. P. 2011a, MNRAS, 413, 2103

—. 2011b, MNRAS, 413, 2103

Pritchard, J. R., & Furlanetto, S. R. 2007, MNRAS, 376, 1680

Pritchard, J. R., & Loeb, A. 2008, Phys. Rev. D, 78, 103511

—. 2012, Reports on Progress in Physics, 75, 086901

Pritchard, J. R., & Pierpaoli, E. 2008, Phys. Rev. D, 78, 065009

Prochaska, J. X., Herbert-Fort, S., & Wolfe, A. M. 2005, ApJ, 635, 123

Reddy, N. A., & Steidel, C. C. 2009, ApJ, 692, 778

Reichardt, C. L., et al. 2011, ArXiv e-prints: 1111.0932

Ricotti, M., & Ostriker, J. P. 2004, MNRAS, 352, 547

Righi, M., Hernández-Monteagudo, C., & Sunyaev, R. A. 2008, A&A, 489, 489

Rogers, A. E. E., & Bowman, J. D. 2008, AJ, 136, 641

Ruhl, J., et al. 2004, in Society of Photo-Optical Instrumentation Engineers (SPIE) Conference Series, Vol. 5498, Society of Photo-Optical Instrumentation Engineers (SPIE) Conference Series, 11–29

Seljak, U., Slosar, A., & McDonald, P. 2006, JCAP, 10, 14

Seo, H.-J., & Eisenstein, D. J. 2003, ApJ, 598, 720

—. 2007, ApJ, 665, 14

Shapiro, P. R., Giroux, M. L., & Babul, A. 1994, ApJ, 427, 25

Sheth, R. K., Mo, H. J., & Tormen, G. 2001, MNRAS, 323, 1

Shull, J. M., & van Steenberg, M. E. 1985, ApJ, 298, 268

Sigurdson, K., & Furlanetto, S. R. 2006, Physical Review Letters, 97, 091301

Silva, L., Granato, G. L., Bressan, A., & Danese, L. 1998, ApJ, 509, 103

Silva, M. B., Santos, M. G., Gong, Y., Cooray, A., & Bock, J. 2013, ApJ, 763, 132

Spergel, D. N., & Hernquist, L. 1992, The Astrophysical Journal Letters, 397, L75

Springel, V. 2005, MNRAS, 364, 1105

Springel, V., Frenk, C. S., & White, S. D. M. 2006, Nature, 440, 1137

Stacy, A., Bromm, V., & Loeb, A. 2011, ApJ, 730, L1

Stark, D. P., Loeb, A., & Ellis, R. S. 2007, ApJ, 668, 627

Subramanian, K., Cen, R., & Ostriker, J. P. 2000, ApJ, 538, 528

Swinyard, B., et al. 2009, Experimental Astronomy, 23, 193

Tegmark, M., Taylor, A. N., & Heavens, A. F. 1997, ApJ, 480, 22

Tegmark, M., & Zaldarriaga, M. 2009, Phys. Rev. D, 79, 083530

The Planck Collaboration. 2006, ArXiv Astrophysics e-prints: 0604069

Thomas, R. M., & Zaroubi, S. 2008, MNRAS, 384, 1080

Thoul, A. A., & Weinberg, D. H. 1996, ApJ, 465, 608

Trac, H., & Pen, U.-L. 2006, New Astronomy, 11, 273

Trenti, M., & Bertin, G. 2005, A&A, 429, 161

Trenti, M., Bertin, G., & van Albada, T. S. 2005, A&A, 433, 57

Trujillo, I., Erwin, P., Asensio Ramos, A., & Graham, A. W. 2004, The Astronomical Journal, 127, 1917

Tseliakhovich, D., Barkana, R., & Hirata, C. M. 2011, MNRAS, 418, 906

Tseliakhovich, D., & Hirata, C. 2010, Phys. Rev. D, 82, 083520

Venkatesan, A., & Benson, A. 2011, MNRAS, 417, 2264

Venkatesan, A., Giroux, M. L., & Shull, J. M. 2001, ApJ, 563, 1

Verner, D. A., Ferland, G. J., Korista, K. T., & Yakovlev, D. G. 1996, ApJ, 465, 487

Visbal, E., & Loeb, A. 2010, JCAP, 11, 16

Vogelsberger, M., Mohayaee, R., & White, S. D. M. 2011, MNRAS, 414, 3044

Volonteri, M., & Gnedin, N. Y. 2009, ApJ, 703, 2113

Wang, J., & White, S. D. M. 2009, MNRAS, 396, 709

Wang, X., Tegmark, M., Santos, M. G., & Knox, L. 2006, ApJ, 650, 529

Warszawski, L., Geil, P. M., & Wyithe, J. S. B. 2009, MNRAS, 396, 1106

Weiß, A., Walter, F., & Scoville, N. Z. 2005, A&A, 438, 533

Wetzel, A. R., Cohn, J. D., & White, M. 2009, MNRAS, 395, 1376

Wetzel, A. R., & White, M. 2010, MNRAS, 403, 1072

White, S. D. M. 1987, in IAU Symposium, Vol. 127, Structure and Dynamics of Elliptical Galaxies, 339–349

Wilson, T. L., Rohlfs, K., & Hüttemeister, S. 2009, Tools of Radio Astronomy

Wise, J. H., & Abel, T. 2007, ApJ, 671, 1559

Wolfe, A. M., Gawiser, E., & Prochaska, J. X. 2005, ARA&A, 43, 861

Wyithe, J. S. B. 2008, MNRAS, 388, 1889

Wyithe, J. S. B., & Loeb, A. 2006, Nature, 441, 322

—. 2007a, MNRAS, 375, 1034

—. 2007b, MNRAS, 382, 921

—. 2008, MNRAS, 383, 606

—. 2009, MNRAS, 397, 1926

Wyithe, J. S. B., Loeb, A., & Geil, P. M. 2008, MNRAS, 383, 1195

Wyithe, J. S. B., & Morales, M. F. 2007, MNRAS, 379, 1647

Zahn, O., Mesinger, A., McQuinn, M., Trac, H., Cen, R., & Hernquist, L. E. 2011, MNRAS, 414, 727

Zahn, O., Zaldarriaga, M., Hernquist, L., & McQuinn, M. 2005, ApJ, 630, 657

Zaldarriaga, M., & Seljak, U. 1997, Phys. Rev. D, 55, 1830

Zmuidzinas, J. 2003, Appl. Opt., 42, 4989

Zukin, P., & Bertschinger, E. 2010a, Phys. Rev. D, 82, 104044

—. 2010b, Phys. Rev. D, 82, 104045